Aerodynamic Modelling and Optimization of Axial Fans

Sørensen, Dan Nørtoft; Sørensen, Jens Nørkær

Publication date:
1998

Document Version
Publisher's PDF, also known as Version of record

Link back to DTU Orbit

Citation (APA):
Sørensen, D. N., & Sørensen, J. N. (1998). Aerodynamic Modelling and Optimization of Axial Fans. Kgs. Lyngby, Denmark: Technical University of Denmark (DTU). (ET-PHD; No. 98-01).

ET-PHD 9801 JANUAR 1998

INSTITUT FOR ENERGITEKNIK
Fluid Mekanik
ISBN-87-7475-196-4

AERODYNAMIC MODELLING AND OPTIMIZATION OF AXIAL FANS

DAN NØRTOFT SØRENSEN

DANMARKS TEKNISKE UNIVERSITET

Printed 1998
Department of Energy Engineering,
Fluid Mechanics Section, Building 404,
Technical University of Denmark
DK-2800 Lyngby, Denmark

Aerodynamic Modelling and Optimization of Axial Fans

Dan Nørtoft Sørensen

Department of Energy Engineering,
Fluid Mechanics Section
Technical University of Denmark, DK-2800 Lyngby, Denmark

This thesis has been produced with the LaTeX document preparation system. The illustrations have been drawn in XFIG and the graphs were created using XMGR. GtPoints was used to extract airfoil data and fan characteristics from referenced material.

LaTeX is developed by Leslie Lamport.
XMGR is developed by Paul J. Turner.
GtPoints is developed by Dan Nørtoft Sørensen.

Department of Energy Engineering,
Fluid Mechanics Section,
Building 404,
Technical University of Denmark,
DK-2800 Lyngby, Denmark.

Preface

This dissertation is submitted in partial fulfilment of the requirements for the degree of Doctor of Philosophy.

The dissertation is based on theoretical and numerical work carried out from the 1st. of February 1994 to 31st. of January 1998 at the Department of Energy Engineering, Technical University of Denmark. The work has been carried out under guidance of Associate Professor, Ph.D. Jens N. Sørensen. His ability to provide qualified and sufficient supervision, regardless of a tremendous workload, continues to amaze me.

The discussions with Dr. Mark C. Thompson on fan aerodynamics as well as optimization strategies for fan optimization are highly appreciated. The discussions took place during my four month stay in Melbourne at the Department of mechanical Engineering, Monash University.

Thanks to Assistant Professors Martin Hansen and Knud Erik Meyer for the informal discussions on fluid mechanics in general and axial fans in particular. Thanks also to M. Sc. (Mech. Eng.) Robert Mikkelsen for providing airfoil data calculated in cascade configurations.

The experimental measurements of the designed fans were carried out at the Danish Institute of Technology under supervision of M. Sc. (Mech. Eng.) Christian Drivsholm.

Finally, thanks to my wife Tina for hours of proof-reading and to my children Sarah and Michael for forcing me to play.

Technical University of Denmark,
Copenhagen, January 31th

Dan Nørtoft Sørensen

Abstract

A numerically efficient mathematical model for the aerodynamics of low speed axial fans of the arbitrary vortex flow type has been developed. The model is based on a blade-element principle, whereby the rotor is divided into a number of annular streamtubes. For each of these streamtubes relations for velocity, pressure and radial position are derived from the conservation laws for mass, tangential momentum and energy. The resulting system of equations is non-linear and, due to mass conservation and pressure equilibrium far downstream of the rotor, strongly coupled. The equations are solved using the Newton-Raphson method, and solutions converged to machine accuracy are found at small computing costs.

The model has been validated against published measurements on various fan configurations, comprising two rotor-only fan stages, a counter-rotating fan unit and a stator-rotor-stator stage. Comparisons of local and integrated properties show that the computed results agree well with the measurements.

Integrating a rotor-only version of the aerodynamic model with an algorithm for numerical design optimization, enables the finding of an optimum fan rotor. The angular velocity of the rotor, the hub radius and the spanwise distributions of pitch angle and chord length have been chosen as independent variables in the optimizations. Besides restricting the geometry of the rotor, constraints have been added to ensure a required pressure rise as well as non-stalled flow conditions.

Optimizations have been performed to maximize the mean value of fan efficiency in a design interval of flow rates, thus designing a fan which operates well over a range of different flow conditions. The optimization scheme was used to investigate the dependence of maximum efficiency on 1: the number of blades, 2: the width of the design interval and 3: the hub radius. The degree of freedom in the choice of design variables and constraints, combined with the design interval concept, provides a valuable design-tool for axial fans.

To further investigate the use of design optimization, a model for the vortex shedding noise from the trailing edge of the blades has been incorporated into the optimization scheme. The noise emission from the blades was minimized in a flow rate design point. Optimizations were performed to investigate the dependence of the noise on 1: the number of blades, 2: a constraint imposed on efficiency and 3: the hub radius. The investigations showed, that a significant reduction of noise could be achieved, at the expense of a small reduction in fan efficiency.

Abstract (in Danish)

En numerisk effektiv matematisk model til bestemmelse af de aerodynamiske forhold for lavhastigheds aksialblæsere af 'arbitrary vortex flow' typen er blever udviklet. Modellen er baseret på blad-element metoden, hvor rotoren opdeles i et antal annulære strømrør. For hvert af disse opstilles relationer for hastigheder, tryk og radiel position ud fra bevarelsesligninger for masse, tangentiel momentum og energi. Det resulterende ligningssystem er ikke-lineært og stærkt koblet pga. massebevarelse samt trykligevægt langt nedstrøms for rotoren. Ligningerne løses med Newton-Raphsons metode og løsninger, konvergeret til maskin-nøjagtighed, findes med begrænsede beregningstider.

Modellen er blevet valideret mod publicerede målinger på forskellige typer af blæserkonstruktioner. Herunder to konstruktioner med én rotor, en konstruktion med to modroterende rotorer samt en konstruktion med ledeskovle før og efter rotoren. Sammenligninger af lokale og globale størrelser viser, at beregningerne stemmer godt overens med målingerne.

Ved sammenkædning af en computermodel til bestemmelse af de aerodynamiske forhold for én rotor med en algoritme til optimering kan en optimal blæserrotor findes. Som uafhængige variable i optimeringen er valgt rotationshastigheden af rotoren, navradius og de radiære fordelinger af bladvinkel og kordelængde. Udover at begrænse geometrien af rotoren er der inkluderet bibetingelser for at sikre en krævet trykstigning samt at sikre at strømningen ikke separerer.

Optimeringer har været udført for at maksimere middelværdien af blæsereffektiviteten i et designinterval af volumenstrømme. Dermed kan blæseren designes til at arbejde godt under forskellige strømningsforhold. Optimeringerne er udført for at undersøge afhængigheden af den maksimale effektivitet for 1: antallet af blade, 2: bredden af designintervallet og 3: nav radius. Muligheden for frit at kunne vælge de uafhængige variable og bibetingelser kombineret med designinterval-konceptet, resulterer i et værdifuldt optimeringsværktøj for aksialblæsere.

For yderligere at undersøge brugen af optimering er en model for støjen pga. hvirvelafkastninger fra bagkanten af bladene, blevet inkluderet i optimeringsværktøjet. Støjen fra bladene er minimeret i et designpunkt af volumenstrøm. Optimeringerne er udført for at undersøge afhængigheden af støjen for 1: antallet af blade, 2: en bibetingelse på effektiviteten og 3: nav radius. Undersøgelserne viste at en væsentlig reduktion af støjen kunne opnåes på bekostning af en lille reduktion i effektivitet.

Contents

List of Symbols

Roman Letters

a	coefficient used in expression for secondary drag. (page 26)
a_0	velocity of sound. (page 121)
b	coefficient used in expression for secondary drag. (page 26)
B	number of blades. (page 10)
$\boldsymbol{B}$	approximation to Hessian of Lagrangian function. (page 60)
c	chord. (page 10)
C_D	drag coefficient. (page 10)
C_{D_s}	secondary drag coefficient. (page 10)
C_L	lift coefficient. (page 10)
$\bar{C}_L$	average lift coefficient. (page 10)
d	distance from rotor to noise measuring probe. (page 122)
D	drag force. (page 10)
D_i	discretized inlet-rotor disc continuity equation. (page 12)
D_T	airfoil trailing edge width. (page 122)
D_w	wake width behind airfoil. (page 121)
e	sound power from one blade. (page 121)
E	total sound power from rotor. (page 122)
E_i	discretized rotor-outlet continuity equation. (page 12)
f	vortex shedding frequency. (page 121)
f_x	axial volume force. (page 11)
f_θ	tangential volume force. (page 11)
F	objective function (figure of merit). (page 56)
F_i	discretized axial relation equation. (page 13)
$\boldsymbol{F}$	vector with RHS in the Newton-Raphson iteration. (page 14)
g_j	constraint no. j. (page 56)
$\boldsymbol{g}$	constraint vector. (page 59)
G_i	discretized pressure equilibrium equation. (page 13)
$\boldsymbol{G}$	matrix with gradients of the constraints as columns. (page 59)
$\boldsymbol{h}$	search direction in optimization algorithm. (page 57)
H_i	discretized tangential momentum equation. (page 13)
i	index of control volume. (page 6)
I_1	discretized global continuity at the rotor disc. (page 13)
I_2	discretized global continuity far downstream. (page 14)
I_3	discretized $\bar{C}_L$ equation. (page 14)
$\boldsymbol{J}_{\boldsymbol{F}}$	Jacobian matrix. (page 14)
k	iteration counter. (page 14)

ℓ	linearized penalty function. (page 63)
L	lift force. (page 10)
L_F	Lagrangian function. (page 57)
$\dot{m}$	mass flow rate. (page 8)
N	number of annular control volumes. (page 9)
N_B	number of Bézier vertices. (page 70)
N_d	number of design interval divisions. (page 67)
p	static pressure. (page 8)
p_0	static pressure level. (page 8)
p_T	integrated fan pressure rise. (page 31)
P	mechanical shaft power. (page 31)
Q	flow rate. (page 9)
Q_c	flow rate center of design interval. (page 67)
ΔQ	design interval width. (page 67)
Q_F	quadratic function. (page 60)
r	radial axis in cylindrical coordinates. (page 6)
Δr	width of control volume. (page 6)
r_0	rotor hub radius. (page 10)
r_N	rotor tip radius. (page 10)
s	interblade spacing, $s = 2\pi r/B$. (page 26)
S_c	correlation area of pressure fluctuations. (page 121)
t	time. (page 121)
V_r	radial velocity. (page 8)
V_{rel}	velocity relative to the blade element. (page 10)
V_x	axial velocity. (page 7)
V_θ	tangential velocity. (page 7)
w	axially induced velocity. (page 7)
w_0	constant level of the axially induced velocity. (page 7)
x	axial axis in cylindrical coordinates. (page 6)
$\boldsymbol{y}$	solution vector in the Newton-Raphson iteration. (page 14)
$\Delta\boldsymbol{y}$	update of solution vector in the Newton-Raphson iteration. (page 14)

Greek Letters:

α	angle of attack relative to the blade element. (page 10)
α_l	step length in optimization algorithm. (page 57)
β	angle between rotational axis and V_{rel}. (page 10)
$\boldsymbol{\delta}$	step taken in the optimization algorithm. (page 61)
Δ	slope of limit to penalty function for the linesearch. (page 62)
η	fan efficiency. (page 31)
$\bar{\eta}$	mean value of fan efficiency in design interval. (page 67)
$\bar{\eta}_{max}$	optimum fan efficiency. (page 67)
$\boldsymbol{\eta}$	approximation to γ ensures positive definite update of B. (page 61)

γ	difference in gradient of the Lagrangian function. (page 61)
γ_0	circulation from vortex. (page 121)
$\boldsymbol{\lambda}$	Lagrangian multiplier vector. (page 57)
λ_j	Lagrangian multiplier for the j'th constraint. (page 57)
μ_j	penalty parameter for the linesearch. (page 62)
Ω	angular velocity of rotor. (page 10)
ϕ	blade element pitch angle. (page 10)
Φ_n	design variable no. n. (page 56)
Ψ	penalty function for the linesearch. (page 62)
ρ	density of fluid. (page 8)
σ	solidity $= c/s$. (page 26)
Θ	scalar ensuring the update of $\boldsymbol{B}$ remains positive definite. (page 61)
θ	tangential axis in cylindrical coordinates. (page 6)
ξ	blade element stagger angle. (page 10)

Subscript/Superscript:

$(\cdot)_1$	plane far upstream of the rotor disc. (page 7)
$(\cdot)_{d1}$	plane immediately upstream of the rotor disc. (page 7)
$(\cdot)_d$	plane at the rotor disc. (page 7)
$(\cdot)_{d2}$	plane immediately downstream of the rotor disc. (page 7)
$(\cdot)_2$	plane far downstream of the rotor disc. (page 7)
$(\cdot)_i$	denotes control volume no. i. (page 6)
$(\cdot)^k$	variable at iteration no. k. (page 14)
$\bar{(\cdot)}$	value at the center of control volume. (page 6)

Acronyms:

BFGS	Broyden-Fletcher-Goldfarb-Shanno. BFGS is an update to the Hessian of a function, using only first order information.
NCON	number of constraints.
NDV	number of design variables.
NEQ	number of equality constraints.
SPL	sound pressure level.
SQP	sequential quadratic programming.

Introduction

For the design of axial flow fans, the usual approach is to employ the free vortex design method. Although this method is simple to use and often results in a high-efficiency fan at the design point, the usefulness of the method is limited for a number of reasons. First of all, requirements of the spanwise distributions of axial and tangential velocity impose limits on the obtainable pressure rise of a free vortex fan. Secondly, analysing the fan away from the design point has only limited validity since the imposed velocity requirements do not apply at off-design conditions. Finally, it is a design method and as such cannot be used to analyse an existing fan which may not be designed for free vortex operation.

To overcome the limitations of the free vortex design method, the present study is concerned with the development of a more general model for arbitrary vortex flow fans with or without stationary guide vanes. This results in an analysis model which can predict pressure rise and efficiency of any axial fan at various flow rates. However, as an analysis method it does not provide means for designing high-efficiency fans. Furthermore, the degree of freedom in the design of the fan blades is increased, compared to the free vortex method, since no limitations of the distributions of velocity are necessary.

For the design of a high-efficiency axial fan of the arbitrary vortex flow type, the analysis model is combined with a numerical design optimization tool. Basically, this provides the user with a design tool for axial fans, but without the limitations of the free vortex design method, thus enabling a higher pressure rise across the fan. Furthermore, since the analysis model enables calculations for various flow rates, the fan may be designed to perform well in a design interval rather than at a design point as in the free vortex design method.

Often, high efficiency is the sole requirement of an axial fan. However, for fans in domestic use, noise emission from the fan may be equally important. Considerable reductions in fan noise may be achieved if precautions are taken during construction of the fan unit. However, some noise originates from the unsteady flow around the fan blades and can only be reduced by altered blade design. Combining the design tool with a noise prediction model enables a minimization of the noise emission while preserving the flow rate and pressure rise capabilities of the fan.

This dissertation describes the developed aerodynamic model for arbitrary vortex flow fans. Strategies for numerical design optimization of axial fans are discussed and examples of maximum efficiency and minimum noise optimizations are given. The thesis is organized as described below. To introduce the work further, the first section of each chapter contains a thorough background discussion.

Chapter 1 deals with the aerodynamic model for rotors or stators, capable of calculating flows of the arbitrary vortex type. The conservation laws governing the physics are derived and the imposed assumptions are listed. The discretization of the equations is stated and a description of the Newton-Raphson method is given. The special case of a rotor-only fan is considered and an alteration is proposed for this more simple problem, which enables calculations for highly loaded rotors. A discussion of the airfoil data used in the present study is given and the concept of secondary drag is introduced.

Chapter 2 contains validations of the aerodynamic model against measurements on various fan configurations, both of the free vortex type and of the arbitrary vortex type. A discussion of the secondary drag contribution is provided.

Chapter 3 describes the numerical method used to find the minimum of a constrained function of several variables. The terms objective function, design variables and constraints are introduced and a detailed description of the optimization algorithm is given. Finally, implementation details are provided for completeness.

Chapter 4 deals with the design optimization of a rotor-only axial fan to maximize efficiency in an interval of flow rates. Following a description of the chosen objective function, design variables and constraints, initial investigations are carried out. Optimizations are performed to investigate the designs dependence on 1: the number of blades, 2: the width of the design interval and 3: the hub radius.

Chapter 5 deals with design optimization of a rotor-only axial fan to minimize the vortex shedding noise in a design point. After defining the minimization problem, optimizations are carried out to investigate the basic differences when optimizing for 1: minimum noise, 2: minimum angular velocity of the rotor and 3: maximum efficiency. Furthermore, the vortex shedding noise is minimized while imposing constraints on the efficiency. Finally, the noise is minimized without including the hub radius as a design variable.

Chapter 6 concludes the work.

Appendix A contains the derivation of the differentiation of the discretized governing equations.

Appendix B contains detailed geometrical descriptions of the blades used in the validations of chapter 2.

Appendix C describes the model used for prediction of the vortex shedding noise.

CHAPTER 1
Aerodynamic Model

This chapter presents the developed engineering model for the aerodynamics of ducted axial flow fans with prerotation. The governing equations apply for stationary guide vanes (stators) as well as rotors and thus, the model describes the aerodynamics of both rotors and stators. Following a review of the background for the proposed model, the governing equations of the model is presented in section 1.2. In section 1.3, the numerical solution procedure is described. Section 1.4 briefly describes governing equations and solution procedure for the special case of a rotor-only configuration with no prerotation. Furthermore, a velocity correction method is proposed, enabling calculations of heavily loaded rotor-only fans. Finally, in section 1.5, a description of the airfoil data and empirical correlations used in the present study is given.

1.1 Background

Ducted axial fans have for many years been employed to drive the flow in ventilation systems. They range from simple propeller-type fans to constructions with two or more stages comprising impellers and stationary vane rows. Single-stage fans are generally considered low-technology components. Their design has to a large extent been based on simple momentum analysis, combined with the experience gained by the individual manufacturer. In many systems, fans operate away from their peak efficiency duties and, as axial fans work continuously over many years, considerable energy savings would be achieved if they were constructed optimally for each installation (Bolton 1990). Thus, there is a need for simple and computationally efficient aerodynamic analysis models for analysis and design of low pressure axial fans. Only a few aerodynamic models have been reported, whereas many researchers focus on the development of sophisticated computational methods for high-pressure compressors and multi-stage gas turbines.

For the construction of new axial fans, the concept of *specific speed* and *specific diameter*, discussed by e.g. Wright (1996), may aid the designer in determining approximate values for fan angular velocity and diameter based on desired flow rate and pressure rise. After this, the detailed geometry of the rotor is determined. This may be done by either an *isolated airfoil method* or by a *cascade method* (Turner 1966). Although differences in the application of the methods exist, the basic aerodynamics are the same for the two methods. However, the isolated airfoil approach is mainly suitable for high-stagger, low solidity fans whereas the cascade method, originating from compressor design, mainly applies for low-stagger, high-solidity units. The difference lies mainly in the use of the airfoil data: where the cascade method is based on inlet and outlet flow angles, the isolated airfoil method uses lift and drag coefficients.

Choosing either of the two above methods, the *free vortex* flow method may be applied for a detailed geometrical design of the rotor as well as stators, if any. The free vortex flow method is a *design method* where the input is the required flow rate and pressure rise across the fan unit. The output, based on further specifications of the fan engineer, is a detailed description of chord, pitch etc. of the blades of the rotor and stators. Thus, the free vortex flow method is characterized by a very limited amount of work to achieve a fan which operates well at the *design point* of flow rate and pressure rise. Employing the isolated airfoil approach, the free vortex design method is described in e.g. Wallis (1961).

The requirement for free vortex flow is a constant spanwise total pressure rise across the fan unit. Furthermore, the axial velocity is required to be constant across the rotor. The combination of these two requirements imply that the tangential velocity is proportional to the inverse radial position. As previously stated, the free vortex flow method is a design method and, as such, cannot be expected to successfully analyse an unknown fan which may not be designed according to the free vortex flow conditions. Furthermore, the free vortex flow method has only limited validity for off-design analysis of a fan designed after the free vortex method, since the requirement of a constant spanwise total pressure rise is not fulfilled away from the design point.

In an axial fan rotor, the local blade speed increases linearly with radius and thus the largest total pressure rise capability exists at the outer part of the blades. For a free vortex flow fan, where the local total pressure rise is required to be constant with radius, the inner part of the rotor defines the pressure rise limit for the rest of the blade which then operates with a pressure rise below the maximum possible. Turning towards an arbitrary vortex flow method, the fan may be designed such that the total pressure rise increases towards the blade tip and thus the design *mean total pressure rise* across the rotor can be higher than for a corresponding free vortex flow fan with equal total pressure rise at the hub of the rotor.

For the modelling of arbitrary vortex flow fans, Kahane (1948) assumed, for design purposes, that the radial velocity component could be neglected. This results in a *design-tool*, where the tangential velocity distribution can be specified and the axial velocity distribution afterwards determined. Using the cascade method and choosing the solidity of the blades, the airfoil sections which resulted in the appropriate turning angles were chosen from NACA cascade data. Two rotors were designed. One exhibiting constant spanwise downstream tangential velocity and the other to achieve a linear increase in the spanwise downstream tangential velocity (solid body rotation). The resulting designs were validated against measurements, further described in section 2.3.2.

Recently, Downie *et al.* (1993) described a mathematical model for *analysing* the arbitrary vortex flow of a *rotor-only* fan without restrictions on the velocity distributions. The model was afterwards successfully validated against both free and arbitrary vortex flow fan configurations. To the authors knowledge, until now, only Downie *et al.* (1993) have addressed the engineering modelling of true arbitrary vortex flows.

In the present work, a simple and computationally efficient, yet reliable, analysis model for low-pressure axial fan units of the arbitrary vortex flow type has been developed. As opposed to the work by e.g. Downie *et al.* (1993), where the flow around a rotor-only fan is considered, the governing equations are formulated so that they apply to both rotors and stators and thus the aerodynamics of a *full-stage* fan unit can be analysed, using the proposed model. The method proposed ensures global continuity to be satisfied at inlet, rotor disc as well as outlet planes. Furthermore, circulation is preserved upstream and downstream of the rotor disc. As the model is to be used in combination with a numerical procedure for optimal design, *computational efficiency* was considered of primary importance and the governing equations are solved using the Newton-Raphson method, ensuring quadratic convergence at low computing costs.

The proposed model should be considered as an *engineering model* with emphasis on computational efficiency. Several flow phenomena, influencing the local flow around the rotor or stator, cannot be governed by this relatively simple model, some of which are described below.

- The governing equations are based on *inviscid theory*. The main implication of this simplification is that the *wall boundary layers* at the hub and tip cannot be modelled accurately. Although the forces from the rotor are altered locally at the hub and tip, comparisons with measurements indicate that the overall flowpatterns are predicted in close agreement with measurements (chapter 2).

- Many authors have investigated the influence of *tip clearance* on fan performance. Although not conclusive on quantitative measures, all agree that increased tip clearance results in decreased efficiency and pressure rise capabilities of the fan unit. Most researchers depict the influence as a function of flow rate, e.g. Fukano *et al.* (1986) and Cudina (1992). This approach is impractical when a fan is designed for a predefined duct system since a lowered pressure rise capability of the fan unit is also reflected in a lowered flow rate, when the system resistance follows the usually assumed relation $\Delta p = kQ^2$, where Δp is the system resistance and Q the flow rate. Venter and Kröger (1992), assuming the above dependency, investigated the influence of the tip clearance and correlated the tip clearance against fan static pressure ratio and a flow rate ratio related to the lowest tip clearance case. Wallis (1993) provides simple expressions for decreasing efficiency and pressure rise with increasing tip clearance.

- Wright (1984) investigated the influence of changing the *hub clearance* on the performance of a rotor-stator fan unit. It was found that a significant decrease of efficiency, achievable flow rate and pressure rise may occur at large hub clearances. A loss of as much as five percent in efficiency at the same flow rate and pressure rise for a large hub clearance is measured, compared to a well-designed rotor. During design of a mine ventilation system, Wallis (1967) decreased the predicted efficiencies with two to three percent since a square cut hub was used for the rotor.

As can be seen from the above, large uncertainties exist in the prediction of these flow phenomena. Although they cannot be included directly in the model, they may be considered as included in the secondary drag contribution (section 1.5.2) which basically governs all losses besides the airfoil losses due to drag. However, for an excessive tip clearance, further empirical losses may be included, as described in section 4.8.

1.2 Model

Considering *axisymmetric flow*, the annulus between the hub and the tip of the rotor disc is divided into a number of *stream tubes* in which flow can enter and leave through the end surfaces only. Each stream tube is defined as a *control volume* in which the continuity equation, the tangential momentum equation and a relation for axial forces, based on energy conservation along a stream line, is derived. Far upstream and far downstream of the rotor disc, fully developed parallel flow exists and the spanwise pressure gradient is in balance with tangential velocity across the stream tubes. Upstream and downstream of the rotor disc, no tangential forces exist and the circulation is preserved. For each stream tube, the forces acting on the rotor are determined iteratively from measured airfoil data. Besides the equations for each stream tube, integral conditions ensure global continuity at the rotor disc and outlet planes.

The model is expressed in cylindrical coordinates, (x, θ, r), with the velocity field denoted as (V_x, V_θ, V_r). In Fig. 1.1 the coordinate system and the indices, used in the following analysis, are defined. The local axial and tangential velocity components are located at the center of the control volume, whereas the pressure is situated at the radial positions. In the following, $\bar{r}$ and $\bar{p}$ denote radius and pressure in the center of the control volume, respectively, and Δr is the width of the control volume. $\Delta r_i = r_i - r_{i-1}$.

In the following all variables are to be taken at the i'th control volume unless otherwise explicitly stated. The i-index is omitted for clarity.

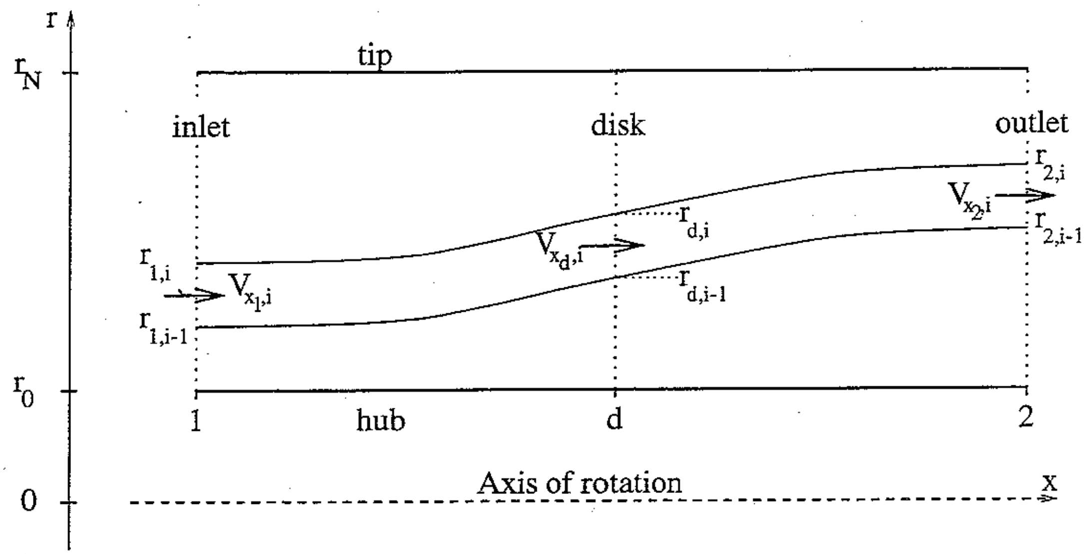

Figure 1.1: The computational domain with indices for the i'th control volume.

1.2.1 Kinematic Relations

Inspired by the *actuator disc method*, discussed by e.g. Horlock (1978), the following kinematic relations may be assumed:

Axial Velocity

From far upstream to far downstream, of the rotor disc, the axial velocity varies continuously in each control volume. In the actuator disc theory, it is assumed that the axial velocity at the rotor disc is the mean of the values far downstream and far upstream. Thus, introducing the axially induced velocity, $w = w(r)$, at the rotor disc, it follows that the velocity is $V_{x_d} = V_{x_1} + w$ at the rotor disc and $V_{x_2} = V_{x_1} + 2w$ far downstream, respectively. This approach is normally taken for *non-ducted* propellers, but for ducted propellers it does not automatically satisfy global continuity. In the present case, the fan analysis model may be combined with similar modules for e.g. stators or pipe bends, and it is of utmost importance that the flow rate leaving the fan unit corresponds to the incoming flow rate. We ensure this by adding a constant level, w_0, to the outflow velocity. Thus, $V_{x_2} = V_{x_1} + 2w + w_0$, where the magnitude of w_0 depends strongly on the skewness of the axial velocity profile experienced at the rotor disc. If the induced velocity, w, is zero for all radial positions, which will be the case for fans of the free vortex flow type, w_0 will be zero.

For *heavily loaded rotors*, the flow in some of the streamtubes becomes *choked*, indicating that $V_{x_2} < 0$. Since this means that flow enters the control volume at both ends, an inconsistency appears and the model is invalid. For the special case of a rotor-only fan without prerotation in the flow, a lower limit on V_{x_2} is imposed, enabling calculations at small flow rates at the expense of accuracy. This is further described in section 1.4.3.

Tangential Velocity

Upstream and downstream of the rotor disc no tangential forces act on the fluid and thus the change in circulation of the fluid occurs in the rotor disc only. The actuator disc theory states that the tangential velocity in the rotor disc is the mean of the ones immediately upstream and downstream of the rotor disc, $2V_{\theta_d} = V_{\theta_{d1}} + V_{\theta_{d2}}$

Upstream and downstream of the rotor disc the *circulation* is preserved, resulting in the following identities for the tangential velocity component from the far upstream to immediately upstream the rotor disc and from immediately downstream the rotor disc to far downstream, respectively:

$$V_{\theta_1} \cdot \bar{r}_1 = V_{\theta_{d1}} \cdot \bar{r}_d. \tag{1.1}$$

$$V_{\theta_{d2}} \cdot \bar{r}_d = V_{\theta_2} \cdot \bar{r}_2. \tag{1.2}$$

Radial Velocity

At a given radial distance from the center line, the radial velocity, V_r, varies continuously as a function of axial distance from the rotor disc. Far upstream and far downstream the flow is assumed to be fully developed with no radial flow.

Pressure

Far upstream of the rotor disc, the spanwise distribution of static pressure is denoted $p_1 = p_1(r)$. Far downstream of the rotor disc, the pressure is divided in a constant level, p_0, and a distribution, p_2, which depends on the radial position. Thus $p(r) = p_0 + p_2(r)$, where p_2 equals zero at the hub radius.

1.2.2 Governing Equations

Here, the conservation laws governing the flow through the rotor (or stator) are defined.

Conservation of Mass

The flow is assumed *incompressible* and conservation of mass results in the following equation:

$$\dot{m} = \rho \int_{CS} \vec{V} \cdot d\vec{A} = 0, \tag{1.3}$$

where ρ is the density of the fluid.

Considering a control volume consisting of an annular stream tube, mass only enters through the control surface at the inlet and leaves at the outlet, far upstream and far downstream of the rotor disc, respectively. For each control volume, the radial positions at both the rotor disc and at the far downstream are unknowns and must ensure that the flow rates at the rotor disc and at the outlet equals the flow rate in the inlet of the control-volume.

From the inlet to the rotor disc, and from the rotor disc to the outlet, this results in the following equations for conservation of mass in a streamtube, respectively

$$2\pi\bar{r}_1 \Delta r_1 V_{x_1} = 2\pi\bar{r}_d \Delta r_d V_{x_d}. \tag{1.4}$$

$$2\pi\bar{r}_d \Delta r_d V_{x_d} = 2\pi\bar{r}_2 \Delta r_2 V_{x_2}. \tag{1.5}$$

Relation for Axial Force

Upstream and downstream of the rotor disc, the *Bernoulli equation* is valid along a stream line contained in the annular control volume. Denoting the static pressure immediately upstream and downstream of the rotor disc as $\bar{p}_{d1}$ and $\bar{p}_{d2}$, respectively, yields

$$\bar{p}_1 + \frac{1}{2}\rho\left(V_{x_1}^2 + V_{\theta_1}^2\right) = \bar{p}_{d1} + \frac{1}{2}\rho\left(V_{x_d}^2 + V_{\theta_{d1}}^2 + V_{r_d}^2\right), \tag{1.6}$$

$$\bar{p}_{d2} + \frac{1}{2}\rho\left(V_{x_d}^2 + V_{r_d}^2 + V_{\theta_{d2}}^2\right) = p_0 + \bar{p}_2 + \frac{1}{2}\rho\left(V_{x_2}^2 + V_{\theta_2}^2\right). \tag{1.7}$$

Since the axial velocity is continuous over the rotor disc, no change in *axial momentum* occurs from immediately upstream to immediately downstream of the rotor disc. This means that the static pressure change across the rotor disc equals the axial force per unit area, f_x, acting on the fluid from the fan rotor

$$\bar{p}_{d2} - \bar{p}_{d1} = f_x. \tag{1.8}$$

Combining eqs. (1.6) - (1.8) and rearranging, yields an equation for the relation of axial forces for a stream tube,

$$p_0 + \bar{p}_2 - \bar{p}_1 + \frac{1}{2}\rho\left(V_{x_2}^2 - V_{x_1}^2 + V_{\theta_2}^2 - V_{\theta_1}^2 + V_{\theta_{d1}}^2 - V_{\theta_{d2}}^2\right) = f_x. \tag{1.9}$$

Pressure Equilibrium Far Downstream

Far downstream of the rotor disc, the flow is assumed parallel and no radial flow exists. Therefore, the radial pressure gradient balances the centrifugal force as

$$\left.\frac{dp}{dr}\right|_2 = \rho\frac{V_{\theta_2}^2}{r_2}. \tag{1.10}$$

Conservation of Tangential Momentum

Across the rotor disc the change in tangential velocity from immediately upstream to immediately downstream is due to the tangential force per unit area, f_θ, acting on the fluid from the fan rotor

$$\rho\left(V_{\theta_{d2}} - V_{\theta_{d1}}\right)V_{x_d} = f_\theta. \tag{1.11}$$

Global Continuity at the Rotor Disc

Summation of the flow rate through all control volumes in the rotor disc must add up to the flow rate, Q, determined by the spanwise axial velocity distribution at the inlet. Thus

$$\sum_{i=1,N} \pi\left(r_{d,i}^2 - r_{d,i-1}^2\right)V_{x_d,i} = Q, \tag{1.12}$$

where N is the number of annular control volumes.

Global Continuity Far Downstream

Far downstream of the rotor disc, the flowrate must again correspond to the inlet flowrate. Thus

$$\sum_{i=1,N} \pi\left(r_{2,i}^2 - r_{2,i-1}^2\right) V_{x_2,i} = Q. \tag{1.13}$$

Equation for Average C_L

The expression for secondary drag, eq. (1.40), involves an average value of the lift coefficient. To ensure quadratic convergence in the Newton-Raphson method, discussed in section 1.3.2, a variable, $\bar{C}_L$, is introduced for the area-averaged lift coefficient. Thus

$$\bar{C}_L = \frac{1}{r_N^2 - r_0^2} \sum_{i=1,N} \left(r_{d,i}^2 - r_{d,i-1}^2\right) C_{L,i}. \tag{1.14}$$

1.2.3 Forces from the Rotor

In Fig. 1.2, a single blade element at $\bar{r}_i$ is shown. The relative velocity, V_{rel}, experienced by the rotating blade, and the angle β, between the rotational axis and V_{rel}, are defined by

$$V_{rel}^2 = \left(\Omega\bar{r}_d - \frac{1}{2}\left(V_{\theta_{d1}} + V_{\theta_{d2}}\right)\right)^2 + \left(V_{x_1} + w\right)^2, \tag{1.15}$$

$$\tan\beta = \frac{\Omega\bar{r}_d - \frac{1}{2}\left(V_{\theta_{d1}} + V_{\theta_{d2}}\right)}{V_{x_1} + w}, \tag{1.16}$$

where Ω is the angular velocity of the rotor disc.

The above implies that the forces experienced by the blade element are determined by the relative velocity, V_{rel}, and the local *angle of attack*, $\alpha = \beta - \xi$. Here ξ is the geometrical *stagger angle* from the airfoil chord line to the axis of rotation. The *pitch angle*, ϕ, is the geometrical pitch angle from the chord line to the plane of rotation, i.e. $\phi = 90^o - \xi$.

The lift and drag forces on a single airfoil blade element are defined as

$$\begin{aligned} L &= \frac{1}{2}\rho V_{rel}^2 c \Delta r_d C_L, \\ D &= \frac{1}{2}\rho V_{rel}^2 c \Delta r_d \left(C_D + C_{D_s}\right). \end{aligned} \tag{1.17}$$

C_L and C_D are airfoil-specific data, C_{D_s} is the secondary drag contribution, dependent on $\bar{C}_L$ (see discussion in section 1.5). The chord length is denoted by c. Denoting the number of blades as B and distributing the force from all blades evenly on the area of the control volume annulus, the local forces per unit area in the axial and tangential direction, respectively, are

$$
\begin{aligned}
f_x &= \frac{B\,(L\sin\beta - D\cos\beta)}{2\pi\bar{r}_d\Delta r_d}, \\
f_\theta &= \frac{B\,(L\cos\beta + D\sin\beta)}{2\pi\bar{r}_d\Delta r_d}.
\end{aligned}
\tag{1.18}
$$

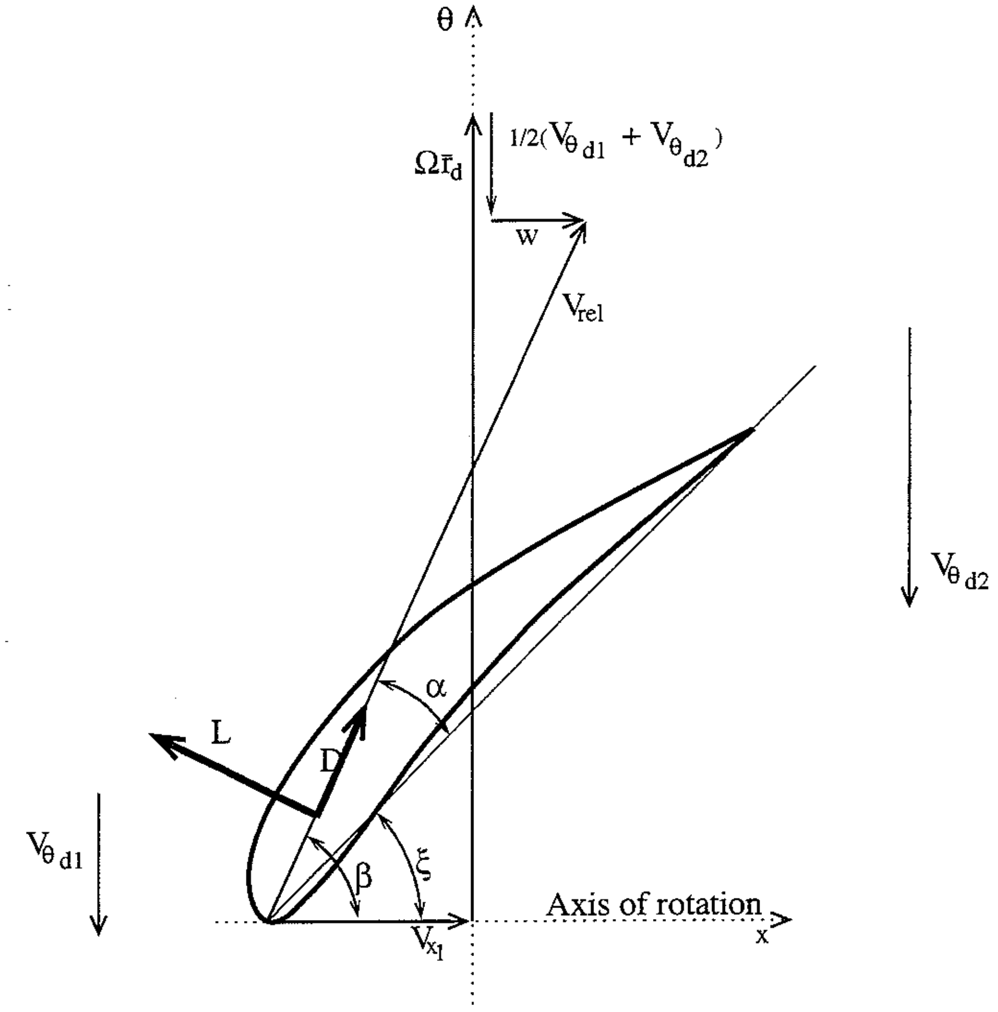

Figure 1.2: Angles and definitions for the rotor with prerotation. Note the direction of the tangential velocity-components. Thus, the tangential velocity felt by the airfoil is $\Omega r_d - 1/2(V_{\theta_1} + V_{\theta_2})$.

1.3 Numerical Solution Procedure

For each control volume, the radial position at the rotor disc, r_d, the radial position far downstream of the rotor disc, r_2, the axially induced velocity, w, the pressure far downstream of the rotor disc, p_2 and the tangential velocity immediately downstream of the rotor disc, $V_{\theta_{d2}}$ are chosen as the variables in the model. Furthermore, three global variables are chosen, namely the pressure level, p_0, the induced velocity level, w_0 and the average lift value $\bar{C}_L$.

Since both hub and tip radii are fixed, only $N-1$ unknown values of r_d and r_2 exist whereas there are N unknowns of w, p_2 and $V_{\theta_{d2}}$.

1.3.1 Discretized Governing Equations

The equations presented in section 1.2.2 are rewritten so that only the above-mentioned variables appear as unknowns. Furthermore, all items are collected on one side of the equality.

Continuity equation, inlet - rotor disc (D_i): Applies to each control volume and thus N equations exist. In the Newton-Raphson method, $r_{d,i}$ is chosen as the independent variable corresponding to D_i, ensuring that the diagonal element in the Jacobian matrix is non-zero. Recalling that only $N-1$ unknown values of r_d exist, the N'th equation determines the boundary condition at the tip of the blade, i.e. $r_{d,N} = r_N$. The discretized form of eq. (1.4) becomes

$$\begin{aligned} D_i \equiv & \left(r_{1,i}^2 - r_{1,i-1}^2\right)\left(V_{x1,i}\right) \\ & - \left(r_{d,i}^2 - r_{d,i-1}^2\right)\left(V_{x1,i} + w_i\right) = 0, \\ D_N \equiv & \, r_{d,N} - r_N = 0. \end{aligned} \tag{1.19}$$

Continuity equation, rotor disc - outlet (E_i): Applies to each control volume and thus N equations exist. r_{2_i} is chosen as the independent variable corresponding to E_i and the N'th equation determines the boundary condition, i.e. $r_{2,N} = r_N$. The discretized form of eq. (1.5) becomes.

$$\begin{aligned} E_i \equiv & \left(r_{d,i}^2 - r_{d,i-1}^2\right)\left(V_{x1,i} + w_i\right) \\ & - \left(r_{2,i}^2 - r_{2,i-1}^2\right)\left(V_{x1,i} + 2w_i + w_0\right) = 0, \\ E_N \equiv & \, r_{2,N} - r_N = 0. \end{aligned} \tag{1.20}$$

Axial relation (F_i): Applies to each of the N control volumes. Choosing the N unknown values of w as independent variables, the number of equations corresponds to the number of unknowns. In discretized form eq. (1.9) reads

$$\begin{aligned}F_i \equiv& \frac{1}{2}\left(p_{2,i}+p_{2,i-1}-p_{1,i}-p_{1,i-1}\right)+p_0\\&+\frac{1}{2}\rho\left[\left(V_{x_1,i}+2w_i+w_0\right)^2-V_{x_1,i}^2\right]\\&+\frac{1}{2}\rho\left[V_{\theta_{d2},i}^2\left(\left(\frac{r_{d,i}+r_{d,i-1}}{r_{2,i}+r_{2,i-1}}\right)^2-1\right)\right]\\&+\frac{1}{2}\rho\left[V_{\theta_1,i}^2\left(\left(\frac{r_{1,i}+r_{1,i-1}}{r_{d,i}+r_{d,i-1}}\right)^2-1\right)\right]-f_x=0.\end{aligned} \tag{1.21}$$

Pressure equilibrium (G_i): Applies across each control volume and thus N equations exist. Recalling that $p_{2,i=0}=0$ and choosing the N unknown values of p_2 as the independent variables for the pressure equilibrium equation, the number of variables corresponds to the number of equations.

Discretizing the pressure equilibrium equation across a control volume, the term dp is evaluated using a finite difference from the $i-1$'th to the i'th value. Thus eq. (1.10) reads

$$\frac{p_{2,i}-p_{2,i-1}}{r_{2,i}-r_{2,i-1}}=\rho\frac{V_{\theta_2,i}^2}{\frac{1}{2}\left(r_{2,i}+r_{2,i-1}\right)},$$

which, by use of eq. (1.2), can be rewritten as

$$\begin{aligned}G_i \equiv& \frac{1}{2}\left(r_{2,i}+r_{2,i-1}\right)^3\left(p_{2,i}-p_{2,i-1}\right)\\&-\rho V_{\theta_{d2},i}^2\left(r_{d,i}+r_{d,i-1}\right)^2\left(r_{2,i}-r_{2,i-1}\right)=0.\end{aligned} \tag{1.22}$$

Tangential momentum equation (H_i): Applies to the N control volumes. Choosing the N unknown values of $V_{\theta_{d2}}$ as the independent variables, the number of equations corresponds to the number of unknowns. Thus, for each control volume, eq. (1.11) reads

$$H_i \equiv \rho\left(V_{x_1,i}+w_i\right)\left(V_{\theta_{d2},i}-V_{\theta_1,i}\frac{r_{1,i}+r_{1,i-1}}{r_{d,i}+r_{d,i-1}}\right)-f_{\theta,i}=0. \tag{1.23}$$

Global continuity at the rotor disc (I_1). Eq. (1.12) yields

$$I_1 \equiv \pi\sum_{i=1,N}\left(r_{d,i}^2-r_{d,i-1}^2\right)\left(V_{x_1,i}+w_i\right)-Q=0. \tag{1.24}$$

Global continuity far downstream (I_2). Eq. (1.13) yields

$$I_2 \equiv \pi\sum_{i=1,N}\left(r_{2,i}^2-r_{2,i-1}^2\right)\left(V_{x_1,i}+2w_i+w_0\right)-Q=0. \tag{1.25}$$

Equation for $\bar{C}_L$ (I_3). Eq. (1.14) yields

$$I_3 \equiv \pi \sum_{i=1,N} \left(r_{d,i}^2 - r_{d,i-1}^2\right) C_{L,i} - \pi \left(r_N^2 - r_0^2\right) \bar{C}_L = 0 \qquad (1.26)$$

1.3.2 Newton-Raphson Method

The discretized governing system of equations (1.19) - (1.26) is strongly coupled and non-linear. Solving the equations by the Newton-Raphson method is *computationally efficient* and exhibits *quadratic convergence.* The Jacobian matrix turns out to be *sparse* and the linear system of equations, occuring in each iteration of the Newton-Raphson method, can be efficiently solved.

The standard formulation of the Newton-Raphson method for solution of a non-linear system of equations is

$$\begin{aligned} \boldsymbol{J_F}\left(\boldsymbol{y}^k\right) \boldsymbol{\Delta y}^k &= -\boldsymbol{F}\left(\boldsymbol{y}^k\right) \\ \boldsymbol{y}^{k+1} &= \boldsymbol{y}^k + \boldsymbol{\Delta y}^k, \quad k = 1, 2, ..., \end{aligned} \qquad (1.27)$$

where $\boldsymbol{y}^k$ contains the solution vector at the k'th iteration and the eqs. (1.19) - (1.26) are contained in $\boldsymbol{F}$. $\boldsymbol{J_F}$ is the Jacobian matrix defined by

$$\boldsymbol{J_F}(y) = \frac{\partial F}{\partial y}.$$

In the present case, the problem is described by $5N + 3$ variables and thus $\boldsymbol{J_F}$ is a $[5N+3] \times [5N+3]$ matrix. The order chosen for the equations in $\boldsymbol{F}$ and their corresponding variables in $\boldsymbol{y}$ is

$$\boldsymbol{F} = \begin{pmatrix} D_1 \\ E_1 \\ F_1 \\ G_1 \\ H_1 \\ \vdots \\ D_N \\ E_N \\ F_N \\ G_N \\ H_N \\ I_1 \\ I_2 \\ I_3 \end{pmatrix} \text{ and } \boldsymbol{y} = \begin{pmatrix} r_{d,1} \\ r_{2,1} \\ w_1 \\ p_{2,1} \\ V_{\theta_{d2},1} \\ \vdots \\ r_{d,N} \\ r_{2,N} \\ w_N \\ p_{2,N} \\ V_{\theta_{d2},N} \\ p_0 \\ w_0 \\ \bar{C}_L \end{pmatrix}. \qquad (1.28)$$

The *explicit differentiation* of the equations in $\boldsymbol{F}$ with respect to the elements in $\boldsymbol{y}$ is presented in appendix A.

Factorization of the Jacobian matrix may be performed by Gaussian elimination of the full $[5N+3] \times [5N+3]$ matrix in each iteration in the Newton-Raphson method. As shown below, the Jacobian matrix is sparse and the computational effort can be reduced significantly by exploiting the sparsity.

Examining eqs. (1.15) and (1.16), it is seen that $V_{rel,i}$ and β_i are functions of $r_{d,i-1}$, $r_{d,i}$, w_i and $V_{\theta_{d2},i}$ only. The forces $f_{x,i}$ and $f_{\theta,i}$ are thus functions of $r_{d,i-1}$, $r_{d,i}$, w_i, $V_{\theta_{d2},i}$ and $\bar{C}_L$ only. For the i'th control volume, according to eqs. (1.19) - (1.23), it is then readily found that

$$\begin{aligned}
D_i &= D_i\left(r_{d,i-1}, r_{d,i}, w_i\right) \\
E_i &= E_i\left(r_{d,i-1}, r_{2,i-1}, r_{d,i}, r_{2,i}, w_i, w_0\right) \\
F_i &= F_i\left(r_{d,i-1}, r_{2,i-1}, p_{2,i-1}, r_{d,i}, r_{2,i}, w_i, p_{2,i}, V_{\theta_{d2},i}, p_0, w_0, \bar{C}_L\right) \\
G_i &= G_i\left(r_{d,i-1}, r_{2,i-1}, p_{2,i-1}, r_{d,i}, r_{2,i}, p_{2,i}, V_{\theta_{d2},i}\right) \\
H_i &= H_i\left(r_{d,i-1}, r_{d,i}, w_i, V_{\theta_{d2},i}, \bar{C}_L\right),
\end{aligned} \tag{1.29}$$

except for $i = N$, where the two continuity equations ensures fixed tip radius. Thus

$$\begin{aligned}
D_N &= D_N\left(r_{d,N}\right) \\
E_N &= E_N\left(r_{2,N}\right)
\end{aligned} \tag{1.30}$$

Besides being functions of p_0, w_0 and $\bar{C}_L$, the equations D_i, E_i, F_i, G_i and H_i are functions of variables at control volumes $i-1$ and i only.

The three global equations (1.24) - (1.26) have the following dependence

$$\begin{aligned}
I_1 &= I_1\left(r_{d,i}, w_i\right) &&, \ i = 1, 2, \ldots, N \\
I_2 &= I_2\left(r_{2,i}, w_i, w_0\right) &&, \ i = 1, 2, \ldots, N \\
I_3 &= I_3\left(r_{d,i}, w_i, V_{\theta_{d2},i}, \bar{C}_L\right) &&, \ i = 1, 2, \ldots, N.
\end{aligned} \tag{1.31}$$

Besides the non zero elements in the last three columns corresponding to the global variables, the equations corresponding to D_i, E_i, F_i, G_i and H_i in the Jacobian matrix have non zero elements close to the diagonal only, due to the ordering in eq. (1.28). As an example, consider the Jacobian matrix for $N = 5$. Denoting a non zero element with a "x" and a zero element with a ".", the outline of the Jacobian becomes

$$
\left[\begin{array}{ccccc|ccccc|ccccc|ccccc|ccccc||ccc}
x & \cdot & x & \cdot & \cdot & \cdot & \cdot & \cdot & \cdot & \cdot & \cdot & \cdot & \cdot & \cdot & \cdot & \cdot & \cdot & \cdot & \cdot & \cdot & \cdot & \cdot & \cdot & \cdot & \cdot & \cdot & \cdot & \cdot \\
x & x & x & \cdot & \cdot & \cdot & \cdot & \cdot & \cdot & \cdot & \cdot & \cdot & \cdot & \cdot & \cdot & \cdot & \cdot & \cdot & \cdot & \cdot & \cdot & \cdot & \cdot & \cdot & \cdot & \cdot & x & \cdot \\
x & x & x & x & x & \cdot & \cdot & \cdot & \cdot & \cdot & \cdot & \cdot & \cdot & \cdot & \cdot & \cdot & \cdot & \cdot & \cdot & \cdot & \cdot & \cdot & \cdot & \cdot & \cdot & x & x & x \\
x & x & \cdot & x & x & \cdot & \cdot & \cdot & \cdot & \cdot & \cdot & \cdot & \cdot & \cdot & \cdot & \cdot & \cdot & \cdot & \cdot & \cdot & \cdot & \cdot & \cdot & \cdot & \cdot & \cdot & \cdot & \cdot \\
x & \cdot & x & \cdot & x & \cdot & \cdot & \cdot & \cdot & \cdot & \cdot & \cdot & \cdot & \cdot & \cdot & \cdot & \cdot & \cdot & \cdot & \cdot & \cdot & \cdot & \cdot & \cdot & \cdot & \cdot & \cdot & x \\
\hline
x & \cdot & \cdot & \cdot & \cdot & x & \cdot & x & \cdot & \cdot & \cdot & \cdot & \cdot & \cdot & \cdot & \cdot & \cdot & \cdot & \cdot & \cdot & \cdot & \cdot & \cdot & \cdot & \cdot & \cdot & \cdot & \cdot \\
x & x & \cdot & \cdot & \cdot & x & x & x & \cdot & \cdot & \cdot & \cdot & \cdot & \cdot & \cdot & \cdot & \cdot & \cdot & \cdot & \cdot & \cdot & \cdot & \cdot & \cdot & \cdot & \cdot & x & \cdot \\
x & x & \cdot & x & \cdot & x & x & x & x & x & \cdot & \cdot & \cdot & \cdot & \cdot & \cdot & \cdot & \cdot & \cdot & \cdot & \cdot & \cdot & \cdot & \cdot & \cdot & x & x & x \\
x & x & \cdot & x & \cdot & x & x & \cdot & x & x & \cdot & \cdot & \cdot & \cdot & \cdot & \cdot & \cdot & \cdot & \cdot & \cdot & \cdot & \cdot & \cdot & \cdot & \cdot & \cdot & \cdot & \cdot \\
x & \cdot & \cdot & \cdot & \cdot & x & \cdot & x & \cdot & x & \cdot & \cdot & \cdot & \cdot & \cdot & \cdot & \cdot & \cdot & \cdot & \cdot & \cdot & \cdot & \cdot & \cdot & \cdot & \cdot & \cdot & x \\
\hline
\cdot & \cdot & \cdot & \cdot & \cdot & x & \cdot & \cdot & \cdot & \cdot & x & \cdot & x & \cdot & \cdot & \cdot & \cdot & \cdot & \cdot & \cdot & \cdot & \cdot & \cdot & \cdot & \cdot & \cdot & \cdot & \cdot \\
\cdot & \cdot & \cdot & \cdot & \cdot & x & x & \cdot & \cdot & \cdot & x & x & x & \cdot & \cdot & \cdot & \cdot & \cdot & \cdot & \cdot & \cdot & \cdot & \cdot & \cdot & \cdot & \cdot & x & \cdot \\
\cdot & \cdot & \cdot & \cdot & \cdot & x & x & \cdot & x & \cdot & x & x & x & x & x & \cdot & \cdot & \cdot & \cdot & \cdot & \cdot & \cdot & \cdot & \cdot & \cdot & x & x & x \\
\cdot & \cdot & \cdot & \cdot & \cdot & x & x & \cdot & x & \cdot & x & x & \cdot & x & x & \cdot & \cdot & \cdot & \cdot & \cdot & \cdot & \cdot & \cdot & \cdot & \cdot & \cdot & \cdot & \cdot \\
\cdot & \cdot & \cdot & \cdot & \cdot & x & \cdot & \cdot & \cdot & \cdot & x & \cdot & x & \cdot & x & \cdot & \cdot & \cdot & \cdot & \cdot & \cdot & \cdot & \cdot & \cdot & \cdot & \cdot & \cdot & x \\
\hline
\cdot & \cdot & \cdot & \cdot & \cdot & \cdot & \cdot & \cdot & \cdot & \cdot & x & \cdot & \cdot & \cdot & \cdot & x & \cdot & x & \cdot & \cdot & \cdot & \cdot & \cdot & \cdot & \cdot & \cdot & \cdot & \cdot \\
\cdot & \cdot & \cdot & \cdot & \cdot & \cdot & \cdot & \cdot & \cdot & \cdot & x & x & \cdot & \cdot & \cdot & x & x & x & \cdot & \cdot & \cdot & \cdot & \cdot & \cdot & \cdot & \cdot & x & \cdot \\
\cdot & \cdot & \cdot & \cdot & \cdot & \cdot & \cdot & \cdot & \cdot & \cdot & x & x & \cdot & x & \cdot & x & x & x & x & x & \cdot & \cdot & \cdot & \cdot & \cdot & x & x & x \\
\cdot & \cdot & \cdot & \cdot & \cdot & \cdot & \cdot & \cdot & \cdot & \cdot & x & x & \cdot & x & \cdot & x & x & \cdot & x & x & \cdot & \cdot & \cdot & \cdot & \cdot & \cdot & \cdot & \cdot \\
\cdot & \cdot & \cdot & \cdot & \cdot & \cdot & \cdot & \cdot & \cdot & \cdot & x & \cdot & \cdot & \cdot & \cdot & x & \cdot & x & \cdot & x & \cdot & \cdot & \cdot & \cdot & \cdot & \cdot & \cdot & x \\
\hline
\cdot & \cdot & \cdot & \cdot & \cdot & \cdot & \cdot & \cdot & \cdot & \cdot & \cdot & \cdot & \cdot & \cdot & \cdot & \cdot & \cdot & \cdot & \cdot & \cdot & x & \cdot & \cdot & \cdot & \cdot & \cdot & \cdot & \cdot \\
\cdot & \cdot & \cdot & \cdot & \cdot & \cdot & \cdot & \cdot & \cdot & \cdot & \cdot & \cdot & \cdot & \cdot & \cdot & \cdot & \cdot & \cdot & \cdot & \cdot & \cdot & x & \cdot & \cdot & \cdot & \cdot & \cdot & \cdot \\
\cdot & \cdot & \cdot & \cdot & \cdot & \cdot & \cdot & \cdot & \cdot & \cdot & \cdot & \cdot & \cdot & \cdot & \cdot & x & x & \cdot & x & \cdot & x & x & x & x & x & x & x & x \\
\cdot & \cdot & \cdot & \cdot & \cdot & \cdot & \cdot & \cdot & \cdot & \cdot & \cdot & \cdot & \cdot & \cdot & \cdot & x & x & \cdot & x & \cdot & x & x & \cdot & x & x & \cdot & \cdot & \cdot \\
\cdot & \cdot & \cdot & \cdot & \cdot & \cdot & \cdot & \cdot & \cdot & \cdot & \cdot & \cdot & \cdot & \cdot & \cdot & x & \cdot & \cdot & \cdot & \cdot & x & \cdot & x & \cdot & x & \cdot & \cdot & x \\
\hline\hline
x & \cdot & x & \cdot & \cdot & x & \cdot & x & \cdot & \cdot & x & \cdot & x & \cdot & \cdot & x & \cdot & x & \cdot & \cdot & x & \cdot & x & \cdot & \cdot & \cdot & \cdot & \cdot \\
\cdot & x & x & \cdot & \cdot & \cdot & x & x & \cdot & \cdot & \cdot & x & x & \cdot & \cdot & \cdot & x & x & \cdot & \cdot & \cdot & x & x & \cdot & \cdot & \cdot & x & \cdot \\
x & \cdot & x & \cdot & x & x & \cdot & x & \cdot & x & x & \cdot & x & \cdot & x & x & \cdot & x & \cdot & x & x & \cdot & x & \cdot & x & \cdot & \cdot & x
\end{array}\right] . \tag{1.32}
$$

The upper left $[5N] \times [5N]$ matrix is seen to be block-tridiagonal with blocksize $[5] \times [5]$ and with the upper block zero. This is advantageous when storing the Jacobian matrix in memory, as only the blocks with non zeros are stored. The factorization of the Jacobian matrix, eq. (1.27), is performed by *Gaussian elimination* of the non zero elements only. The sparsity of the Jacobian matrix results in a computational effort of the factorization being proportional to N (as opposed to the factorization of a full matrix which is proportional to N^3). Since the number of iterations in the Newton method is independent of N, the computational effort for the fan analysis is thus found to be *proportional* to N.

The Newton-Raphson method may diverge if the initial guess is chosen far from the solution. It was found that converging solutions were usually obtained if $p_{2,i} = p_{1,i} - p_{1,0}$, $w_i = 0$, $V_{\theta_{d2},i} = 0$, $r_{2,i} = r_{d,i} = r_{1,i}$, $p_0 = p_{1,0}$, $w_0 = 0$ and $\bar{C}_L = 0$ for the first point calculated on the performance curve. For succeeding points, the previous solution was used as initial guess.

1.4 Rotor-Only Configuration

In this section, the special case of a *rotor-only* configuration without prerotation is examined (Sørensen and Sørensen 1997). This simplified problem may be solved using the "full" model, described in section 1.2 and section 1.3. However, utilizing the simplified flow-conditions, it turns out that only four governing equations and four independent variables are necessary for each control volume to model the flow. This furthermore implies that the Jacobian matrix reduces from size $[5N+3] \times [5N+3]$ to size $[4N+3] \times [4N+3]$. Thus, the computational effort in each Newton-Raphson iteration is reduced significantly. When analysing an existing fan configuration, this is not important. However, when integrating the aerodynamic model with an optimization scheme, many fan configurations are examined and the decreased computational effort is advantageous.

The main difference from the full model is that *no rotation* exists before the rotor. This in turn implies that no radial pressure gradient is present far upstream of the rotor. Furthermore, the flow is assumed to be fully developed with constant axial velocity far upstream of the rotor.

Investigating the discretized governing equations from section 1.3.1 and recalling that $V_{\theta_1,i} = 0$, the radial positions at the inlet, $r_{1,i}$ only appears in the continuity equation from the inlet to the rotor disc (eq. (1.19)). This in turn indicates that r_1 need not be included in the solution of the rotor-only case. Removing the inlet-rotor disc continuity equation and fixing the values of the radial positions at the rotor disc, r_d, rather than the inlet radial positions, results in a set of simplified governing equations as well as a decreased computational effort when solving the equations.

In section 1.4.1, the alterations to the discretized governing equations are presented. The changes to the Jacobian matrix are discussed in section 1.4.2. Finally, in section 1.4.3, an alteration to the axial relation, to be used for heavily loaded rotors, is proposed.

1.4.1 Discretized Governing Equations

The only changes to the discretized governing equations occur in the relation for axial force and in the tangential momentum equation. Furthermore, the continuity equation from the inlet to the rotor disc is removed. Restating the altered discretized governing equations for the relation of axial force and the tangential momentum equation from section 1.3.1 with $V_{\theta_1,i} = 0$, yields

Axial relation (F_i):

$$\begin{aligned} F_i \equiv \frac{1}{2}\left(p_{2,i} + p_{2,i-1} - p_{1,i} - p_{1,i-1}\right) + p_0 \\ + \frac{1}{2}\rho\left[\left(V_{x_1,i} + 2w_i + w_0\right)^2 - V_{x_1,i}^2\right] \\ + \frac{1}{2}\rho\left[V_{\theta_{d2},i}^2\left(\left(\frac{r_{d,i} + r_{d,i-1}}{r_{2,i} + r_{2,i-1}}\right)^2 - 1\right)\right] - f_x = 0. \end{aligned} \tag{1.33}$$

Tangential momentum equation (H_i):

$$H_i \equiv \rho \left(V_{x_1,i} + w_i\right) V_{\theta_{d2},i} - f_{\theta,i} = 0. \tag{1.34}$$

The remaining discretized equations are not changed.

1.4.2 Newton-Raphson Method

Although the simplifications do not seem to radically change the computational effort for the solution, the fact that the radial positions at the rotor disc, r_d is fixed changes the dependence of the governing equations on the independent variables. This in turns means decreased computational effort, both when building the Jacobian matrix and in the following factorization.

When $V_{\theta_{d1},i} = 0$ and $r_{d,i}$ is fixed, β_i and $V_{rel,i}$ are functions of w_i and $V_{\theta_{d2},i}$ only, and not of $r_{d,i-1}$ and $r_{d,i}$ as in the "full" model. According to the simplified discretized equations, utilizing fixed $r_{d,i}$, it is then found that

$$\begin{aligned}
E_i &= E_i\left(r_{2,i-1}, r_{2,i}, w_i, w_0\right) \\
F_i &= F_i\left(r_{2,i-1}, p_{2,i-1}, r_{2,i}, w_i, p_{2,i}, V_{\theta_{d2},i}, p_0, w_0, \bar{C}_L\right) \\
G_i &= G_i\left(r_{2,i-1}, p_{2,i-1}, r_{2,i}, p_{2,i}, V_{\theta_{d2},i}\right) \\
H_i &= H_i\left(w_i, V_{\theta_{d2},i}, \bar{C}_L\right),
\end{aligned} \tag{1.35}$$

except for $i = N$, where the continuity equation from rotor disc to outlet ensures fixed tip radius. Thus

$$E_N = E_N\left(r_{2,N}\right) \tag{1.36}$$

The three global equations have the following dependence

$$\begin{aligned}
I_1 &= I_1\left(w_i\right) &&, \ i = 1, 2, \dots, N \\
I_2 &= I_2\left(r_{2,i}, w_i, w_0\right) &&, \ i = 1, 2, \dots, N \\
I_3 &= I_3\left(w_i, V_{\theta_{d2},i}, \bar{C}_L\right) &&, \ i = 1, 2, \dots, N.
\end{aligned} \tag{1.37}$$

The outline of the Jacobian matrix for $N = 5$ becomes

$$\left[\begin{array}{cccc|cccc|cccc|cccc|cccc||ccc}
x & x & \cdot & \cdot & \cdot & \cdot & \cdot & \cdot & \cdot & \cdot & \cdot & \cdot & \cdot & \cdot & \cdot & \cdot & \cdot & \cdot & \cdot & \cdot & \cdot & x & \cdot \\
x & x & x & x & \cdot & \cdot & \cdot & \cdot & \cdot & \cdot & \cdot & \cdot & \cdot & \cdot & \cdot & \cdot & \cdot & \cdot & \cdot & \cdot & x & x & x \\
x & \cdot & x & x & \cdot & \cdot & \cdot & \cdot & \cdot & \cdot & \cdot & \cdot & \cdot & \cdot & \cdot & \cdot & \cdot & \cdot & \cdot & \cdot & \cdot & \cdot & \cdot \\
\cdot & x & \cdot & x & \cdot & \cdot & \cdot & \cdot & \cdot & \cdot & \cdot & \cdot & \cdot & \cdot & \cdot & \cdot & \cdot & \cdot & \cdot & \cdot & \cdot & \cdot & x \\
\hline
x & \cdot & \cdot & \cdot & x & x & \cdot & \cdot & \cdot & \cdot & \cdot & \cdot & \cdot & \cdot & \cdot & \cdot & \cdot & \cdot & \cdot & \cdot & \cdot & x & \cdot \\
x & \cdot & x & \cdot & x & x & x & x & \cdot & \cdot & \cdot & \cdot & \cdot & \cdot & \cdot & \cdot & \cdot & \cdot & \cdot & \cdot & x & x & x \\
x & \cdot & x & \cdot & x & \cdot & x & x & \cdot & \cdot & \cdot & \cdot & \cdot & \cdot & \cdot & \cdot & \cdot & \cdot & \cdot & \cdot & \cdot & \cdot & \cdot \\
\cdot & \cdot & \cdot & \cdot & \cdot & x & \cdot & x & \cdot & \cdot & \cdot & \cdot & \cdot & \cdot & \cdot & \cdot & \cdot & \cdot & \cdot & \cdot & \cdot & \cdot & x \\
\hline
\cdot & \cdot & \cdot & \cdot & x & \cdot & \cdot & \cdot & x & x & \cdot & \cdot & \cdot & \cdot & \cdot & \cdot & \cdot & \cdot & \cdot & \cdot & \cdot & x & \cdot \\
\cdot & \cdot & \cdot & \cdot & x & \cdot & x & \cdot & x & x & x & x & \cdot & \cdot & \cdot & \cdot & \cdot & \cdot & \cdot & \cdot & x & x & x \\
\cdot & \cdot & \cdot & \cdot & x & \cdot & x & \cdot & x & \cdot & x & x & \cdot & \cdot & \cdot & \cdot & \cdot & \cdot & \cdot & \cdot & \cdot & \cdot & \cdot \\
\cdot & \cdot & \cdot & \cdot & \cdot & \cdot & \cdot & \cdot & \cdot & x & \cdot & x & \cdot & \cdot & \cdot & \cdot & \cdot & \cdot & \cdot & \cdot & \cdot & \cdot & x \\
\hline
\cdot & \cdot & \cdot & \cdot & \cdot & \cdot & \cdot & \cdot & x & \cdot & \cdot & \cdot & x & x & \cdot & \cdot & \cdot & \cdot & \cdot & \cdot & \cdot & x & \cdot \\
\cdot & \cdot & \cdot & \cdot & \cdot & \cdot & \cdot & \cdot & x & \cdot & x & \cdot & x & x & x & x & \cdot & \cdot & \cdot & \cdot & x & x & x \\
\cdot & \cdot & \cdot & \cdot & \cdot & \cdot & \cdot & \cdot & x & \cdot & x & \cdot & x & \cdot & x & x & \cdot & \cdot & \cdot & \cdot & \cdot & \cdot & \cdot \\
\cdot & \cdot & \cdot & \cdot & \cdot & \cdot & \cdot & \cdot & \cdot & \cdot & \cdot & \cdot & \cdot & x & \cdot & x & \cdot & \cdot & \cdot & \cdot & \cdot & \cdot & x \\
\hline
\cdot & \cdot & \cdot & \cdot & \cdot & \cdot & \cdot & \cdot & \cdot & \cdot & \cdot & \cdot & \cdot & \cdot & \cdot & \cdot & x & \cdot & \cdot & \cdot & \cdot & \cdot & \cdot \\
\cdot & \cdot & \cdot & \cdot & \cdot & \cdot & \cdot & \cdot & \cdot & \cdot & \cdot & \cdot & x & \cdot & x & \cdot & x & x & x & x & x & x & x \\
\cdot & \cdot & \cdot & \cdot & \cdot & \cdot & \cdot & \cdot & \cdot & \cdot & \cdot & \cdot & x & \cdot & x & \cdot & x & \cdot & x & x & \cdot & \cdot & \cdot \\
\cdot & \cdot & \cdot & \cdot & \cdot & \cdot & \cdot & \cdot & \cdot & \cdot & \cdot & \cdot & \cdot & \cdot & \cdot & \cdot & \cdot & x & \cdot & x & \cdot & \cdot & x \\
\hline\hline
\cdot & x & \cdot & \cdot & \cdot & x & \cdot & \cdot & \cdot & x & \cdot & \cdot & \cdot & x & \cdot & \cdot & \cdot & x & \cdot & \cdot & \cdot & \cdot & \cdot \\
x & x & \cdot & \cdot & x & x & \cdot & \cdot & x & x & \cdot & \cdot & x & x & \cdot & \cdot & x & x & \cdot & \cdot & \cdot & x & \cdot \\
\cdot & x & \cdot & x & \cdot & x & \cdot & x & \cdot & x & \cdot & x & \cdot & x & \cdot & x & \cdot & x & \cdot & x & \cdot & \cdot & x
\end{array}\right] . \tag{1.38}$$

1.4.3 Heavily Loaded Rotors

At the inner part of the rotor a pronounced *deceleration* of the flow occurs for *heavily loaded rotors.* If, for any streamtube, the axial velocity far downstream of the rotor disc becomes negative, indicating reversed flow, the model is invalid. For wind turbines and propellers, an empirical correction by Glauert (1935) may be introduced where the equations become invalid. Since the correction does not ensure conservation of mass, a different approach was chosen in the present work. Here, the axial velocity far downstream of the rotor disc is *fixed* at a minimum value of $1/4V_{x_1}$, if, during solution of the equations, a lower value is found.

Even though the velocity correction may alter the velocity and pressure distributions significantly at the inboard sections of the blade, the areas of the streamtubes at the inner radii are small and thus the effect on the global properties is expected to be small. It must be emphasized that, rather than being based on physical reasoning, the velocity correction is imposed to enable calculations at small flow rates and thus, the results obtained should be used with caution.

The correction is done by replacing the discretized equation for the axial relation, eq. (1.34), with

$$F_i \equiv V_{x_1,i} + 2w_i + w_0 - 1/4V_{x_1,i} = 0, \tag{1.39}$$

which, when satisfied, defines the outflow velocity to be fixed at a value of $1/4V_{x_1}$. In the implementation of the velocity correction, it is assumed that the lowest axial velocity always occurs at the inner-most part of the rotor blade. Thus, if at some control volume, a lower value of the axial outlet velocity is found, the correction from eq. (1.39) is used for the first control volume. If problems still occur, the correction is used for the second control volume as well, and so on.

1.5 Airfoil Data and Losses

The aerodynamic model, described in the previous sections, is based on simple physical conservation laws. Besides the assumed kinematic relations from section 1.2.1, the only empirical relations used, are for the airfoil *lift* and *drag* coefficients and for the *secondary drag* coefficient.

A large number of accurate measurements, including stalled conditions, exist for isolated two-dimensional airfoils. In contrast, measurements on airfoil in cascade, experiencing multiplane interference, are rarely seen. In the present study, when cascade measurements were not available, two-dimensional airfoil data were corrected for multiplane interference using an empirical correlation for solidity and stagger. The airfoil data used as well as the empirical correlation are described in section 1.5.1.

In the aerodynamic model, losses from e.g. wall boundary layers, tip clearance and annulus-to-full tube expansion are not included. In the free vortex flow design method, described by e.g. Wallis (1993), these losses are included as a secondary drag contribution. Due to the lack of a more sophisticated method, the same approach has been taken in the present study. A description of the secondary drag is given in section 1.5.2.

1.5.1 Airfoil Data

One of the main shortcommings of the proposed aerodynamic model is the dependency on airfoil lift and drag coefficients. For axial fans, blades are often constructed with high *chord-to-spacing* ratios implying that airfoil data obtained from experiments on isolated airfoils are not suitable for the analysis of fans. To the authors knowledge, only the NACA 65 airfoil family has been extensively investigated in a cascade wind tunnel (Herrig *et al.* 1951).

To enable corrections for *multiplane interference* in the data for isolated airfoils, an approach described in e.g. Wallis (1993) is taken. Here, an *interference factor*, stating the ratio between multiplane lift coefficient and isolated airfoil lift coefficient is provided as a function of stagger angle and solidity. According to Wallis, the *isolated airfoil correction* method only applies for circular-arc camber lines. As will become evident in the following, the method seems to result in inaccurate values of the lift coefficient for some of the airfoils considered. No corresponding correction exists for the drag coefficient and thus, the isolated airfoil values are used.

To obtain more accurate airfoil data in cascade configurations, the general purpose incompressible Navier-Stokes solver EllipSys2D (Michelsen 1992; Sørensen 1995) has been used by Mikkelsen (1997) to *calculate* the aerodynamic performance of airfoils in *cascade* configurations. A significant part of the work has been to create a grid generator enabling periodic boundaries for modelling of airfoils in cascades (Mikkelsen 1997). The calculated lift coefficients show a very good agreement with the measurements on the NACA 65 airfoil (Mikkelsen 1997). Based on this validation, calculations for other types of airfoils are believed to yield satisfactory results. Due to the extensive calculation time of the solver, combined with the large number of parameters in cascade configurations, it has only been possible to obtain calculated lift and drag coefficients for a few selected airfoils in certain configurations.

Below, a description of the airfoil data used for the various fan analysis and optimizations in the following chapters is provided. Due to the lack of a more accurate method, the isolated airfoil correction method is used whenever measured or calculated cascade data are not available. The airfoil data are used as they are and no attempts have been made to correct the data for the dependency on e.g. Reynolds number or surface-roughness. Especially the former may be of importance in fan applications since a critical Reynolds number exists, below which the characteristics of the airfoil data change significantly (Roberts 1975).

Cambered Flat Plate

In the work by Downie *et al.* (1993), investigated in section 2.3.1, the case 2 rotor is constructed using cambered flat plates.

Measurements of isolated airfoil data for lift and drag coefficients are obtained from Wallis (1993). The isolated airfoil correction method is used to correct the data for multiplane interference.

F-series Airfoil

In the work by Downie *et al.* (1993), described in section 2.3.1, the case 1 rotor is constructed using F-series airfoils with an additional nose-droop. In section 2.5, the stators before and after the rotor are constructed using the C4 airfoil (Mathews *et al.* 1967). The C4 airfoil is a zero nose-droop F-series airfoil.

Isolated airfoil data for the F-series airfoil and a functional relationship for the influence of nose-droop are proposed in Wallis (1977). The isolated airfoil correction method is used to alter the data for multiplane interference.

In chapter 4, the above data and corrections are used to find an optimum rotor geometry. Measurements on one of the obtained optimum rotor geometries were performed at the Danish Institute of Technology, and a poor agreement was found (section 4.8). To investigate whether the deviations could be attributed to the use of isolated airfoil data corrected for multiplane interference, a set of airfoil data, calculated by Mikkelsen (1997), was used for the analysis of the optimum design and a slight improvement in the fan characteristics was found.

In Fig. 1.3, lift curves, predicted by the multiplane correction method, are shown for three spanwise stations along the blade. Also, lift curves predicted by the CFD-model for the same three spanwise stations are shown. Large discrepancies between the two methods are seen and, especially, it may be noted that the lift values for the correction method decreases from the root towards the tip, whereas the opposite tendency is found from the CFD-data.

As described further in chapter 4, the camber angle of the blades decreases linearly from

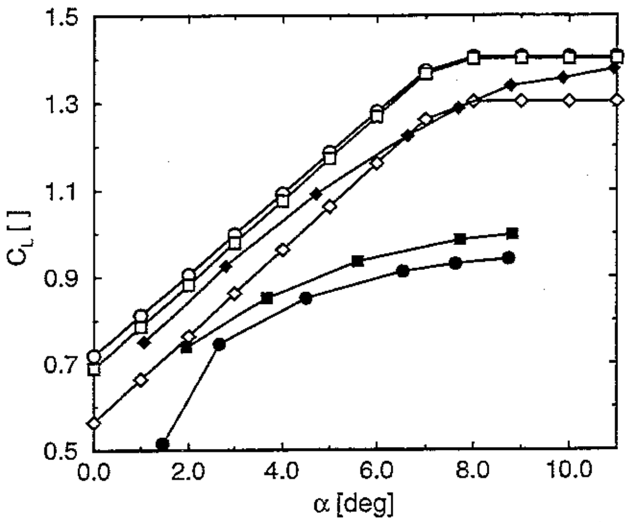

Figure 1.3: Lift coefficients as a function of angle of attack for three spanwise stations along the optimum rotor blade investigated in section 4.8. Data are shown for the isolated airfoil correction method as well as for the CFD-method.
○: hub station, □: station no. 10, ◇: tip station. Filled symbols are data predicted by the CFD-model, open symbols are data predicted by the isolated airfoil correction method.

six percent at the root to four percent at the tip of the blades. Also, the solidity of the optimum blade is always below one and decreasing towards the tip. Furthermore, large stagger angles are found for the optimum design.

For the isolated airfoil correction method, solidities below one, combined with the large stagger angles found for the optimum design, results in very limited corrections to the isolated airfoil lift coefficients. The decrease in camber towards the tip is thus reflected in the decrease in lift coefficients towards the tip of the blade, depicted in Fig. 1.3.

Contrary to this, the CFD-model predicts a large influence from multiplane interference, even for the small values of solidity and large values of stagger occuring for the optimum design. Thus, the increase in lift coefficients towards the tip is mainly due to a decrease in solidities, the influence from which is larger than the influence from the decrease in camber towards the tip of the blade.

To draw any conclusions, based on the above discrepancies, is very difficult. However, at smaller values of stagger angles, the agreement between the two approaches was found to be good, when the solidity was between 0.75 and 1.25. Thus, for large values of stagger angle and small values of solidity, it seems that, either the CFD-model predicts an excessive influence from stagger angle and solidity, or else the correction to isolated airfoil data predicts an influence from stagger angle and solidity below the actual case.

In section 4.8, the optimum fan is analysed with both sets of data and the implications of using either set of data are discussed.

NACA 65-(12)10 Airfoil

In Kahane (1948), measurements of a fan employing NACA 65-(12)10 blades were performed and in section 2.3.2 comparisons with the aerodynamic model are carried out. Airfoil data for a range of solidities and stagger angles, measured in a cascade wind tunnel, are described in Herrig *et al.* (1951). The data are mainly suitable for compressor design purposes and there is a lack of data for high-stagger, low-solidity blades. This means that, for the analysis of the Kahane (1948) fan, an extrapolation is necessary at solidities below 1, especially at large inflow angles (i.e. low flow rates).

In Herrig *et al.* (1951), the data are prepared for the cascade method of fan analysis and a conversion is performed to obtain lift and drag as a function of angle of attack on the airfoil, suitable for the presently used aerodynamic model.

RAF 6E Airfoil

In section 2.4, a counter-rotating axial fan stage from Bell and DeKoster (1942) is investigated. The rotors are constructed using 12 % thick RAF 6E airfoils, exhibiting a flat undersurface. Preliminary calculations using isolated airfoil data from Wallis (1961) with the isolated airfoil correction method showed excessive loads on the rotors. Therefore, calculations of airfoil data for two of the fan configurations were performed using the CFD-method.

Fig. 1.4 compares lift coefficients for one of the rotors exhibiting a constant chord with a hub-solidity of 1.05 and a tip solidity of 0.73. For the CFD-method as well as for the correction method, the lift coefficients increase with radius (i.e. with lowered solidities) as expected. However, although the shape of the curves are similar, the lift values predicted by the isolated airfoil correction method are, generally, higher than the ones predicted by the CFD-method. One explanation for this may be, that the correction method applies for circular-arc camber lines and thus may be inaccurate for the flat undersurface RAF 6E airfoils.

To investigate the airfoil data further, comparisons are made of the 24 blade rotor with a hub pitch angle of 30.5^o. Fig. 1.5 depicts the lift coefficients and again, an influence from solidity is found in the calculations by the CFD-method. For the approach with corrected isolated airfoil data, the mid and tip sections exhibit similar lift curves. This is due to the larger stagger angles for which the correction method results in isolated airfoil data. For this rotor, the calculations of section 2.4 showed that very small angles of attack would occur. Thus, the airfoil data by the CFD-method has been extended to low angles of attack. Investigating Fig. 1.5, it seems that the lift coefficients predicted by the CFD-method tends to bend upwards at low angles of attack. As discussed further in section 2.4 this is found to influence some of the rotor-rotor solutions.

Finally, similar comparisons are made for the rotor exhibiting half the solidities of the front rotor described above. Fig. 1.6 depicts the lift coefficients and it is seen that the CFD-method predicts much smaller changes in lift coefficients, due to changes in solidity, than for the high-solidity blade of Fig. 1.4. The isolated airfoil correction method predicts use of isolated airfoil data, due to the low values of solidity, and thus the curves for the three spanwise stations coincide. The lift coefficients predicted by the CFD-method is in close agreement with the airfoil data from Wallis (1961). This implies that, for the low-solidity rotor, isolated airfoil data would have been adequate.

Clark Y Airfoil

In section 2.5, the rotor of the stator-rotor-stator configuration is created using a 10 % thick Clark Y airfoil, exhibiting a flat undersurface. Isolated airfoil data from Wallis (1961) is used for the lift and drag coefficients, combined with the isolated airfoil correction method.

As indicated by the above investigations of the RAF 6E airfoil, the isolated airfoil correction method does not apply well for flat undersurface airfoils. However, although the solidity of the investigated rotor is 1.2 at the hub, the length of the chord decreases rapidly with radius and the correction method predicts use of isolated airfoil data at the outer 80 % of the blade. The use of the isolated airfoil correction method is thus found to be justifyed for the Clark Y rotor.

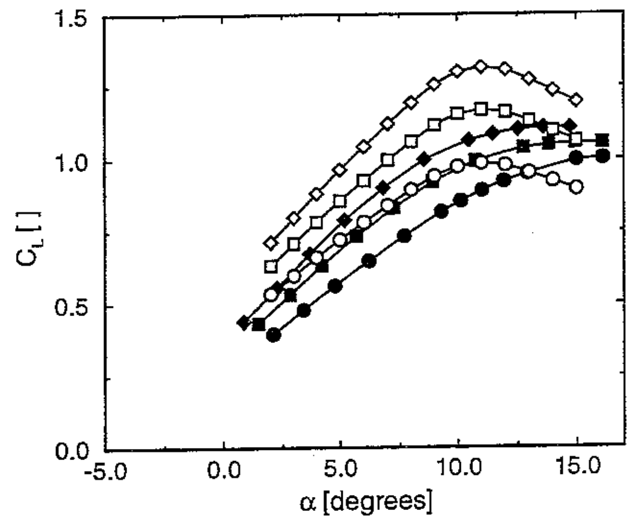

Figure 1.4: Lift coefficients as a function of angle of attack for three spanwise stations along the rotor blade, investigated in section 2.4. The blades exhibit 50.5 degree pitch angle at the hub, and solidities varying from 1.05 at the hub to 0.73 at the tip. Data are shown for the isolated airfoil correction method as well as for the CFD-method.
○: hub station, □: midspan station, ◇: tip station. Filled symbols are data predicted by the CFD-model, open symbols are data predicted by the isolated airfoil correction method.

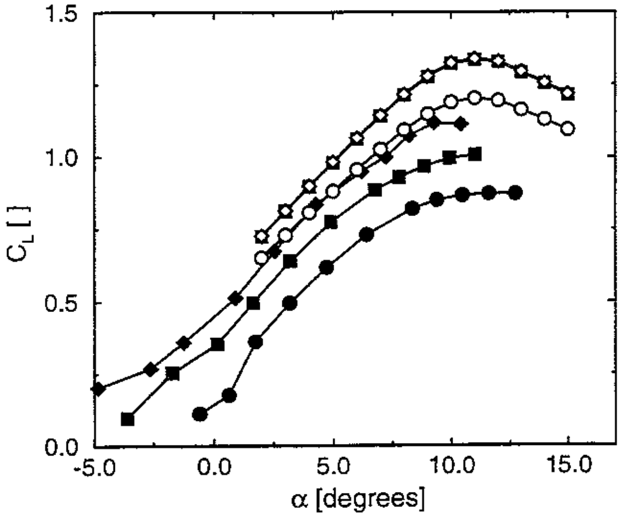

Figure 1.5: Lift coefficients as a function of angle of attack for three spanwise stations along the rotor blade, investigated in section 2.4. The blades exhibit 30.5 degree pitch angle at the hub, and solidities varying from 1.05 at the hub to 0.73 at the tip.
○: hub station, □: midspan station, ◇: tip station. Filled symbols: CFD-method, open symbols: isolated airfoil correction method.

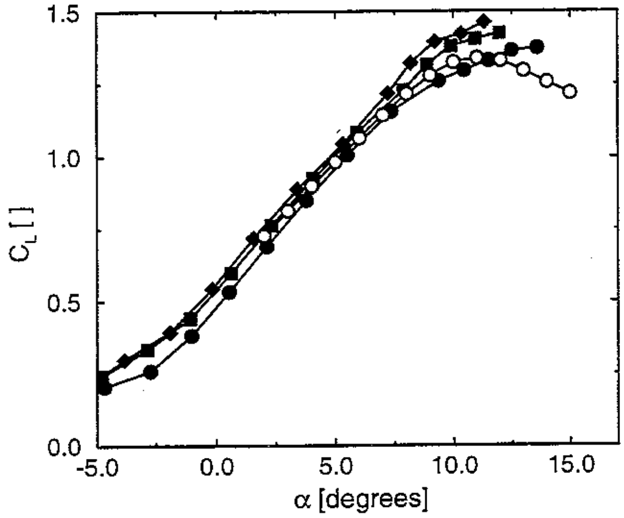

Figure 1.6: Lift coefficients as a function of angle of attack for three spanwise stations along the front rotor blade, investigated in section 2.4. The blades exhibit 30.5 degree pitch angle at the hub, and solidities varying from 0.52 at the hub to 0.36 at the tip.
●: hub station - CFD-method, ■: midspan station - CFD-method, ◆: tip station - CFD-method. ○: all stations - isolated airfoil correction method.

1.5.2 Secondary Drag

Secondary losses from hub, tip, wall shear etc. change the nature of the flow around the blades of the fan rotor and stators. The interrelated nature of the secondary losses implies that determination of reasonable correction terms, based on the physics of the flow, for each type of loss is not possible. To enable a simple, yet reasonable, determination of the secondary losses, the standard procedure in both fan and compressor design is to include all losses in a term denoted the *secondary drag.*

In the present work, an expression from Wallis (1993) is used for the secondary drag as

$$C_{D_s} = a\bar{C}_L^2 + bc/(\sigma[r_N - r_0]), \qquad (1.40)$$

where a and b are empirical constants. σ denotes the solidity. For the fan rotor, the values for a and b have been determined from measurements on a large number of fan configurations. Recommended values for a are $a = 0.018$ for airfoil-type blades and $a = 0.025$ for flat plate airfoils. For b, the recommended value is $b = 0.02$ (Wallis 1993). However, Wallis discusses the possibility that $b = 0$ is a more reasonable value. In the present work, if not stated otherwise, the above proposed values for a are used and the value of b is defined as $b = 0.02$

For the counter-rotating fan unit, described in section 2.4, $a = 0.018$ and $b = 0$ are used for both rotors.

For prerotators (stator upstream of the rotor), $a = 0.015$ and $b = 0$ are suggested and for stators (downstream of the rotor), $a = 0.018$ and $b = 0$, has been found to provide good comparisons with measurements (Wallis 1993).

In section 2.6, implications of the secondary drag term is discussed in detail. A few calculations with altered values of a and b are performed to investigate the influence from the secondary drag term.

CHAPTER 2

Validation of the Aerodynamic Model

In this chapter, the aerodynamic model from chapter 1 is validated against measured data from the literature. Following a brief background, discussing the problems of obtaining reasonable measurements which can be used for comparisons with the model, initial investigations of the aerodynamic models of chapter 1 is carried out in section 2.2. Section 2.3 comprises validation of the rotor-only implementation of the aerodynamic model (from section 1.4). Section 2.4 investigates rotor-rotor configurations and a stator-rotor-stator configuration is investigated in section 2.5. Finally, in section 2.6, the dependence of the solutions on the secondary drag term is discussed and a few fan analysis are presented with altered expressions for the secondary drag.

2.1 Background

Although measurements of the performance of fan units are frequently described in the literature, a thorough description of the spanwise distribution of chord, pitch etc. are rarely given. Furthermore, definitions of pressure rise and efficiency may be badly explained and vary from article to article. Finally, the uncertainties of the measurement setup is rarely discussed. All of these factors influence the choice of suitable fan units to use for the validation of the model.

Rather than being the "best" possible measurement-setups, the following validations are chosen because thorough descriptions of the fan units are given and, furthermore, local spanwise measurements are described in the majority of the chosen test cases. Finally, measurements were desired on different types of fan units to enable a thorough validation of the capabilities of the arbitrary vortex flow model. The measured results are taken "as is" without discussions of the accuracy of the experimental setup. However, for all the test cases, considerations have been given to provide a uniform inflow, avoid excessive tip clearance, etc. Thus, the measurements conform well with the requirements for the aerodynamic model.

To further emphasize on the difficulties arising when measuring the characteristics of a fan, the work by Randall *et al.* (1996) is described. Here, a comparison of two series of measurements performed on the same exhaust fan is described. Although designed independently, taking different approaches in the setup and instrumentation, both fan test rigs follows the British Standard (BSI 1980). Comparing the results from the two test rigs clearly shows a difference in the measured pressure rise across the fan unit, both in the normal operating range and, especially, at low flow rates where stall occurs on the rotor blades. However, it was found that the differences were systematic and a calibration procedure was proposed by Randall *et al.* (1996), enabling similar results from the two test rigs.

During interpretation of the results, the comments concluding section 1.1 must be remembered. Especially for comparisons of spanwise distributions, the inviscid model cannot capture the boundary layers at the hub and tip where discrepancies are experienced. Furthermore, effects from tip clearance and other installation effects are not included in the aerodynamic model. Finally, the uncertainty of the airfoil data, discussed in section 1.5.1, must be remembered during interpretation of the results.

For flow rate and integrated properties (pressure rise and shaft power), data are presented *with dimensions* to exemplify the large differences in pressure rise and flow rate capabilities of the fan units investigated. For some of the fan units investigated, the pressure rise is several thousand Pascals. Although this implies a changed density, no attempts have been made to include this in the calculations.

Appendix B contains detailed geometrical descriptions of the rotors and stators used in the experimental setups.

2.2 Initial Investigations

Employing the Newton-Raphson method for the solution of the discretized system of equations is advantageous since *quadratic convergence* is expected. In Fig. 2.1, the convergence history for a representative fan-calculation, using the rotor-only version of section 1.4, is shown. The quadratic convergence is clearly seen and in all of the following performed calculations, approximately seven iterations are necessary to obtain a solution converged to machine accuracy.

As stated in section 1.4.2, the computational effort in each iteration of the Newton-

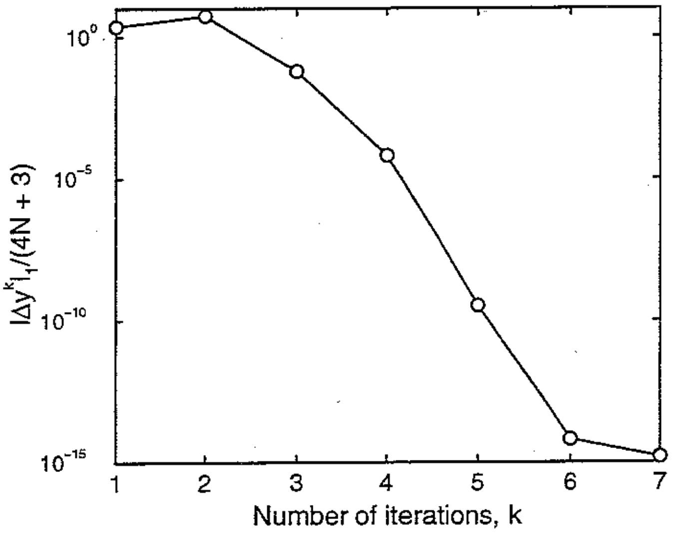

Figure 2.1: Convergence history of the case 1 rotor from section 2.3.1. $N = 33$, $Q = 1.84m^3/s$, $\Omega = 1000$ RPM.
o: One-norm divided by number of unknowns.

Raphson method depends approximately *linearly* on the number of blade elements. To determine the sufficient number of blade elements to use in the calculations, a number of calculations are performed on the same fan configuration with varying number of blade elements. Again, the rotor-only version of the model is used. In Fig. 2.2 the efficiency is depicted as a function of k, $N = 2^k + 1$, relative to the case of $k = 12$ which is used as the 'true' reference value. The accuracy is seen to improve with the number of blade elements and $N = 2^5 + 1$ blade elements is found to yield results within 0.01% of the reference value. This accuracy is found acceptable and thus $N = 33$ blade elements are used in all of the validations in this chapter as well as for the optimizations carried out in later chapters.

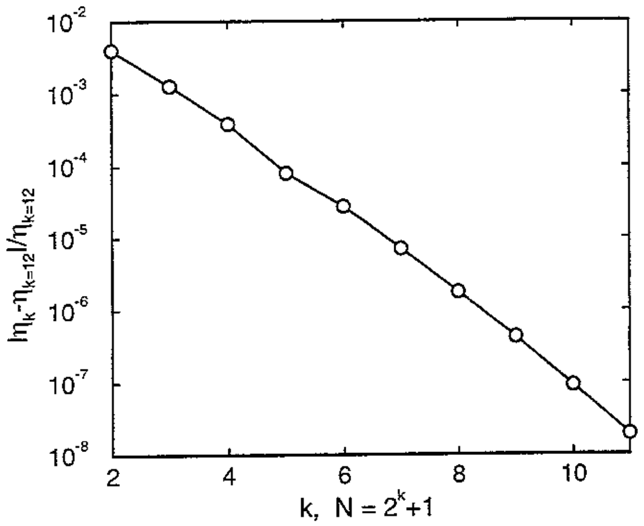

Figure 2.2: Dependency on the number of blade elements of the case 1 rotor from section 2.3.1. $Q = 1.84 m^3/s$, $\Omega = 1000$ RPM. The number of blade elements is $N = 2^k + 1$ and the case $k = 12$ ($N = 2^{12} + 1 = 4097$) is used as a reference value.
o: Efficiency relative to the reference case.

The final question raised is whether the general purpose aerodynamic model of sections 1.2 - 1.3 yields the same results as the rotor-only model of section 1.4. Naturally, this should only be the case when a rotor-only configuration is examined, since the rotor-only version does not include prerotation upstream of the rotor disc. Using the same fan configuration as in the above investigations, calculations are performed with both models, for varying number of blade elements. In Fig. 2.3, the difference in the predicted efficiency is depicted as a function of the number of blade elements, and a good agreement between the models is seen. The minor differences are believed to occur mainly because the streamtubes in the rotor-only model are fixed at the rotor disc whereas, in the general model, they are fixed at the inlet, thus allowing the streamtubes at the rotor disc to move. Furthermore, the difference in predicted efficiency is seen to decrease with increasing number of blade elements.

Performing calculations of a rotor-only fan stage, the calculation time for each flow rate analysis is approximately 0.02 seconds on a Pentium PC for the rotor-only version of the model. For the general model, the calculation time is approximately three times larger. The difference is important for fan optimizations since thousands of calculations are performed before reaching the optimum.

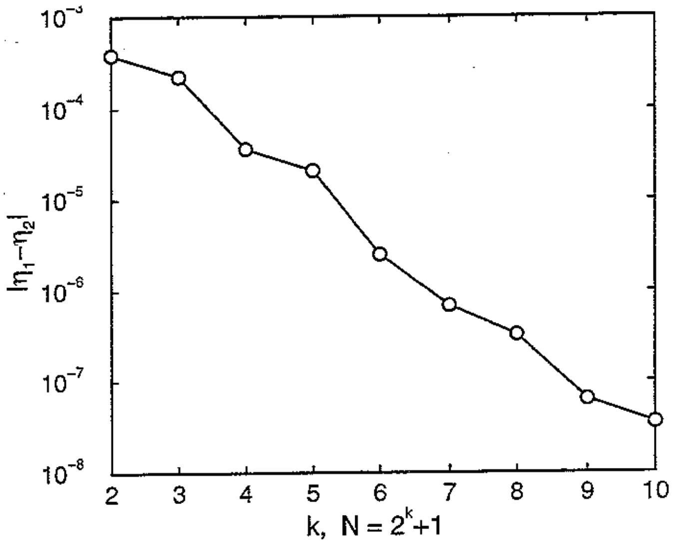

Figure 2.3: Difference in efficiency-prediction between the general aerodynamic model and the rotor-only version. Case 1 rotor from section 2.3.1. $Q = 1.84m^3/s$, $\Omega = 1000$ RPM.
o: Difference in predicted efficiency by the two versions of the model as a function of the number of blade elements.

2.3 Rotor-Only Configurations

For the calculations of the rotor-only configurations in this section, the rotor-only version of the aerodynamic model is used (as opposed to the general aerodynamic model from section 1.2). The main reason for this is to demonstrate the velocity correction method of section 1.4.3 when the rotors become heavily loaded. For the general aerodynamic model, no correction is implemented and the Newton-Raphson method diverges for heavily loaded rotors.

2.3.1 Work by Downie *et al.* (1993)

In the work by Downie *et al.* (1993), an extensive measurement program was established. Using a five hole pressure probe, spanwise distributions of axial, tangential and radial velocity, as well as static and total pressure, were measured downstream of three rotor configurations. Global parameters, e.g. rotor total pressure rise and efficiency as a function of flow rate, were also determined. The experimental setup has an inner tube with hub diameter installed after the rotor. This enables measurements of the local spanwise distributions of velocity and pressure, and eliminates the uncertainties from pressure losses when expanding to full tube area.

In the following, calculations are compared with measurements from Downie *et al.* (1993) for two test cases: Case 1 rotor, denoted *Mark 3* in Downie *et al.*, designed using F-series airfoils. Case 2 rotor, denoted *Mark 1* in Downie *et al.*, designed using cambered flat plate airfoils. The rotor geometries were obtained from Thompson (1996).

To enable comparisons, the definitions of rotor total pressure rise, p_T, and efficiency, η, from Downie *et al.* (1993) are used. The rotor total pressure rise is the area-integrated sum of the total pressure rise, including the contribution from the tangential velocity component. The efficiency is defined as

$$\eta = \frac{Q \cdot p_T}{P},$$

where P is the mechanical shaft power required to run the fan, calculated from L and D.

Predicted efficiency, η, and rotor total pressure rise, p_T, for the case 1 rotor, compared with measurements presented in Wallis (1993), are shown in Figs. 2.4 and 2.5. The efficiency is generally 10% underpredicted by the analysis model but the measured and calculated curves have the same shape. The total pressure rise is well determined, but again the calculated values are below the measurements. It may be noted that the calculated results from Wallis (1993) show approximately the same deviation from measurements. Since both models are essentially inviscid, calculations are expected to result in excessive values of efficiency, contrary to what is found.

One explanation for the above discrepancies may be found in the magnitude of the secondary drag contribution, eq. (1.40). During construction of the experimental setup described by Downie *et al.* (1993), care was taken to minimize tip clearance and furthermore, the installation of an inner cylinder downstream of the rotor removed losses associated with the expansion after the rotor. Thus, for the secondary drag, the expression in the model may actually be too pessimistic. This is further investigated in section 2.6.

At small flow rates ($Q < 1.55m^3/s$), the model is invalid at the inner control volumes and the proposed velocity correction determines the axial velocity in the outlet. It can be seen that, even at small flow rates, a reasonable magnitude of the efficiency is found.

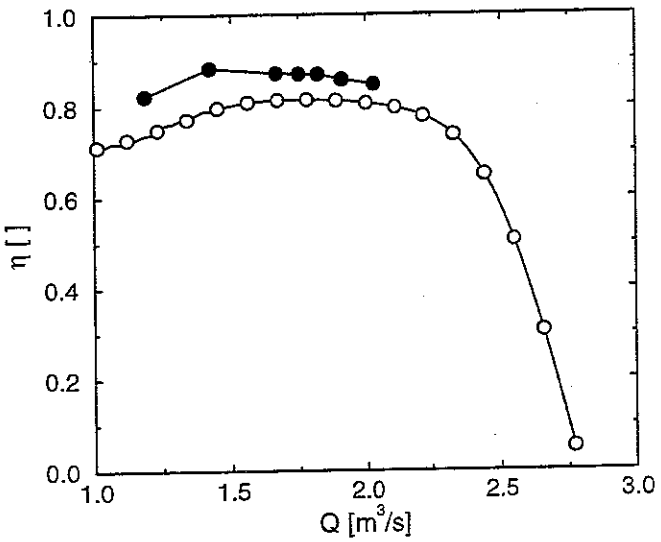

Figure 2.4: Efficiency of case 1 rotor for $\Omega = 1000$ RPM at various flow rates.
●: measured, ○: calculated

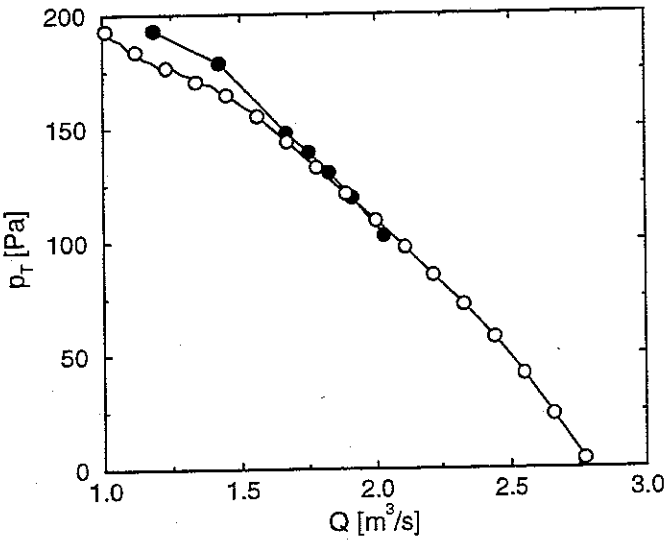

Figure 2.5: Total pressure rise of case 1 rotor for $\Omega = 1000$ RPM at various flow rates.
●: measured, ○: calculated

To further validate the model, global properties for the case 2 rotor are examined. In Figs. 2.6 and 2.7, efficiency and rotor total pressure rise are compared with measurements from Wallis (1993). Although not as pronounced as for the case 1 rotor, again efficiency and pressure rise are underpredicted by the analysis model for medium to high flow rates. For low flow rates, stalled conditions are clearly seen from the measurements. This is not as pronounced from the calculations, mainly due to inaccurate airfoil data.

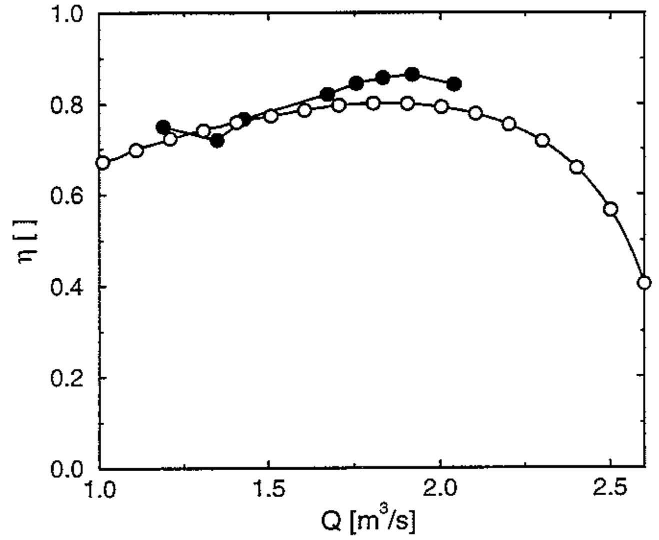

Figure 2.6: Efficiency of case 2 rotor for $\Omega = 1000$ RPM at various flow rates.
●: measured, ○: calculated.

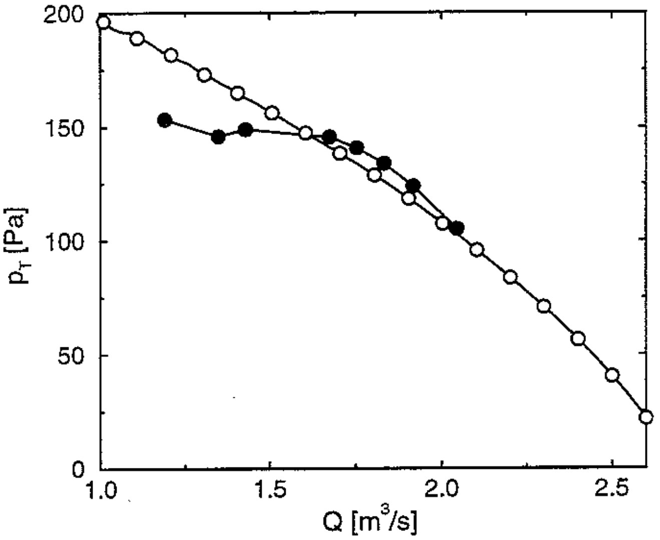

Figure 2.7: Total pressure rise of case 2 rotor for $\Omega = 1000$ RPM at various flow rates.
●: measured, ○: calculated.

Local parameters for the case 1 rotor were calculated at two flow rates. In Figs. 2.8 - 2.10 spanwise distributions of axial velocity, tangential velocity and static pressure are compared to measurements by Downie *et al.* (1993). The two velocity components are nondimensionalized with the inflow velocity, the static pressure with the inflow dynamic pressure and the radius with the tip radius. Hub, tip and wall shear clearly influence the measured axial velocity distribution (Fig. 2.8). This influence cannot be modelled with the present method which, except for the forces on the blade elements, is inviscid. The flow rates for the calculations are the same as for the measurements; thus the excessive axial velocity, predicted at the hub and tip, is compensated by a decreased velocity along the center part of the blade. For the high flow rate $Q = 1.84m^3/s$, near the design point, calculations compare well with measurements, but for the lower flow rate $Q = 1.44m^3/s$, the prediction at the inboard section of the blade is poor. This is mainly due to the fact that the velocity correction to the model becomes effective at the inner control volumes, fixing the axial velocity ratio at 1/4.

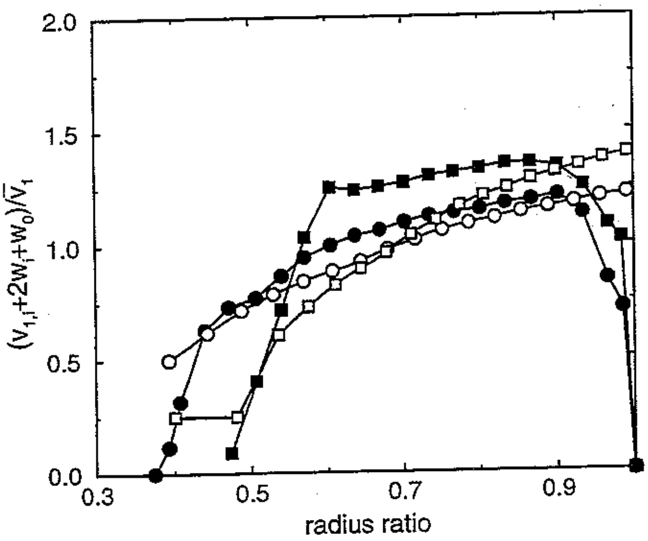

Figure 2.8: Spanwise distribution of axial velocity far downstream of case 1 rotor, $\Omega = 1000$ RPM.
●: measured, $Q = 1.84m^3/s$, ○: calculated, $Q = 1.84m^3/s$, ■: measured, $Q = 1.44m^3/s$, □: calculated, $Q = 1.44m^3/s$.

At the hub and tip, some discrepancies in the tangential velocity distribution (Fig. 2.9) are found, which is also due to viscous effects. The velocity correction of the axial velocity for $Q = 1.44m^3/s$ is seen to influence the tangential velocity at the hub. The static pressure rise (Fig. 2.10) is predicted well, except near the hub, for $Q = 1.44m^3/s$, where the influence from the reversed flow is not captured by the velocity correction method.

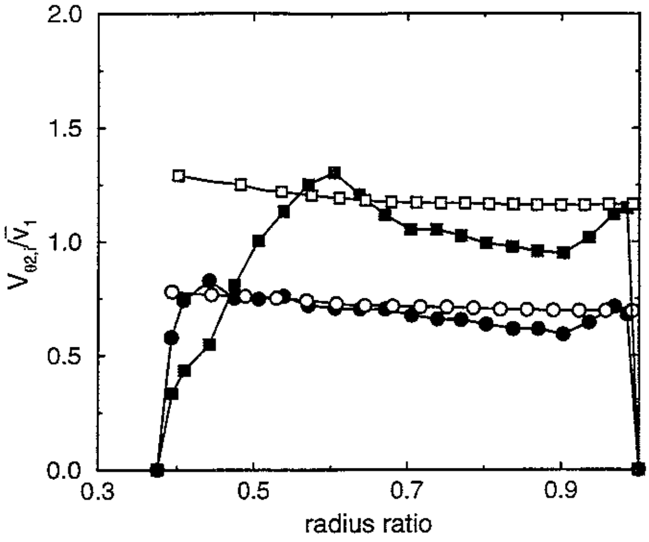

Figure 2.9: Spanwise distribution of tangential velocity far downstream of case 1 rotor, $\Omega = 1000$ RPM.
●: measured, $Q = 1.84m^3/s$, ○: calculated, $Q = 1.84m^3/s$, ■: measured, $Q = 1.44m^3/s$, □: calculated, $Q = 1.44m^3/s$.

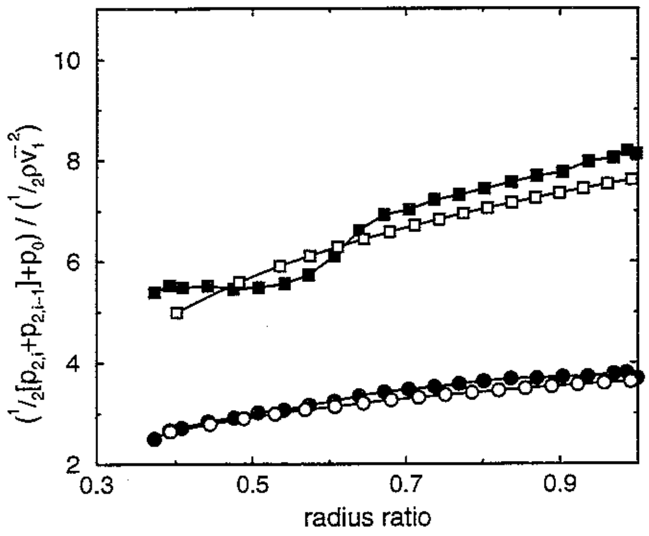

Figure 2.10: Spanwise distribution of static pressure far downstream of case 1 rotor, $\Omega = 1000$ RPM.
●: measured, $Q = 1.84m^3/s$, ○: calculated, $Q = 1.84m^3/s$, ■: measured, $Q = 1.44m^3/s$, □: calculated, $Q = 1.44m^3/s$.

2.3.2 Work by Kahane (1948)

In the work by Kahane (1948), investigations were performed to determine whether three-dimensional flow may be utilized in axial fans with the purpose of increasing the pressure rise capabilities. A simplified design method for arbitrary vortex flow fans was proposed and two rotors were tested against experiments. Rotating a yaw head as well as static and total pressure tubes along a radial axis enabled determination of spanwise distributions of flow angle, pressures and velocities. The downstream measurement station was located 1.4 chord lengths behind the blade trailing edges. The method proposed by Kahane (1948) is a design method and as such, he only compares calculations with measurements at the design flow rate.

The two rotors were designed for uniform tangential velocity and solid body rotation, respectively, at the design flow rate. It was found that the latter could be constructed as a straight blade with uniform chord and airfoil section along the span. The NACA 65-(12)10 airfoil was chosen (section 1.5.1). The hub-to-tip ratio is 0.69 and the rotor consists of 24 blades. The solidity is 1.22 at the hub and 0.84 at the tip of the blades

To compare measurements and calculations, the definitions of rotor static and total pressure rise from Kahane (1948) are used. The integrated properties are mass-weighted as compared to the area-weighted properties used in the rest of this study. The difference in predicted pressure rise by the two methods is within 1-2 %. The dimensionless parameters from Kahane (1948) have been transformed by a density of $\rho = 1.21 kg/m^3$ and a fan angular velocity of 3000 RPM. The design flow rate is $Q = 4.45 m^3/s$.

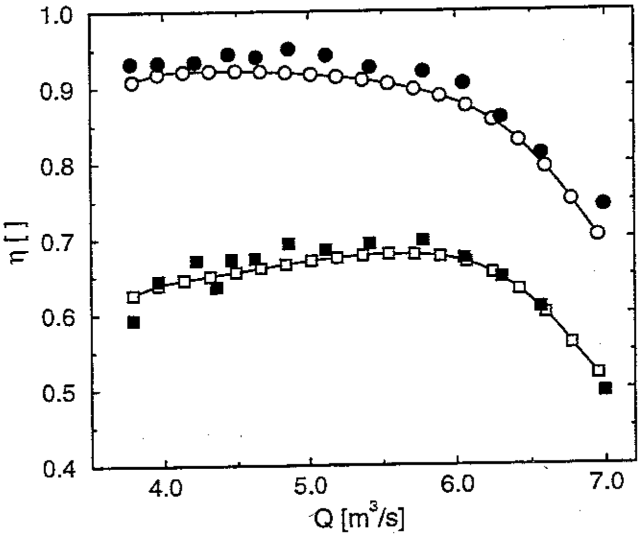

Figure 2.11: Efficiency at various flow rates.
o: efficiency based on total pressure rise, □: efficiency based on static pressure rise. Filled symbols are measured values, open symbols are the calculated values.

Predicted efficiencies based on static and total pressure, respectively, is shown in Fig. 2.11. The efficiency is generally underpredicted by approximately two percent, which is found to be very good. Especially since the maximum efficiency occurs approximately at the same flow rate and the shape of the curves is very much alike in general.

The static and total pressure rises are depicted in Fig. 2.12. Again, the agreement is found to be good, although the pressure rise is underpredicted with up to 4 %. In Fig. 2.13, the shaft power is depicted and again an underprediction of a few percent is seen. Generally, the discrepancies between the global measured and calculated values are found to be small and fully acceptable. Especially since the deviations are systematic across the range of flow rates investigated.

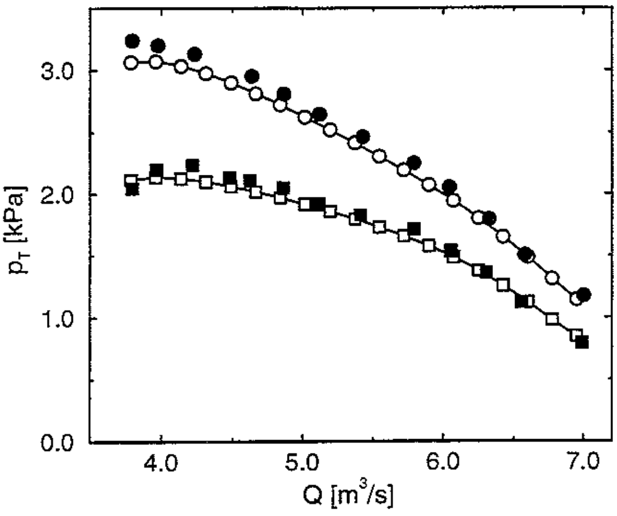

Figure 2.12: Pressure rise at various flow rates.
○: total pressure rise, □: static pressure rise. Filled symbols are measured values, open symbols are the calculated values.

To further validate the model, local flow properties are compared to the measurements. The two velocity components are nondimensionalized with the inflow velocity, the static pressure with the inflow dynamic pressure and the radius with the tip radius.

In Figs. 2.14 - 2.16, the spanwise distribution of axial velocity at three flow rates are depicted. Fig. 2.14, is at a high flow rate and the calculation compares well with the measurements. The main reason for the high quality of the prediction may be attributed to the very thin boundary layers at this high flow rate. Fig. 2.15 shows the axial velocity distribution at the design flow rate. Again the comparisons are good, however, the boundary layers have a large effect on the global flow field. Finally, Fig. 2.16 depicts the axial velocity at a low flow rate and the global flow pattern is seen to be highly affected by the boundary layers. Also, the calculated axial velocity distribution exhibits a bend around the midspan. This is believed to be due to inaccuracies in the extrapolations of the airfoil data, further described in section 1.5.1, which will mainly be used at the lower flow rates.

In Fig. 2.17, the tangential velocity is depicted at three different flow rates. Again the calculations compare well with the measurements. However, a systematic deviation is seen with smaller calculated tangential velocities at the hub and higher calculated values

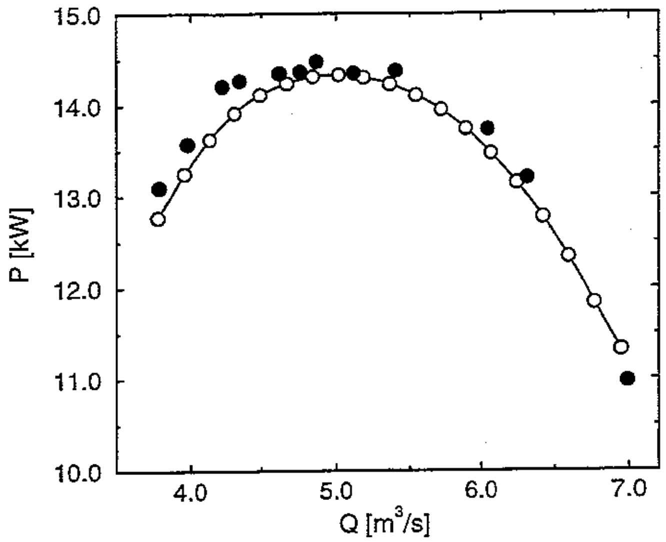

Figure 2.13: Shaft power at various flow rates.
○: calculated shaft power, ●: measured shaft power.

at the tip. No explanation for this can be given. However, it may be noted that the same deviation was found, at the design flow rate of $Q = 4.45m^3/s$, in the original work by Kahane (1948).

Finally, in Fig. 2.18, the spanwise distribution of static pressure is depicted. Again the comparisons are good, however at the design flow rate, the static pressure is underestimated by approximately 5 %.

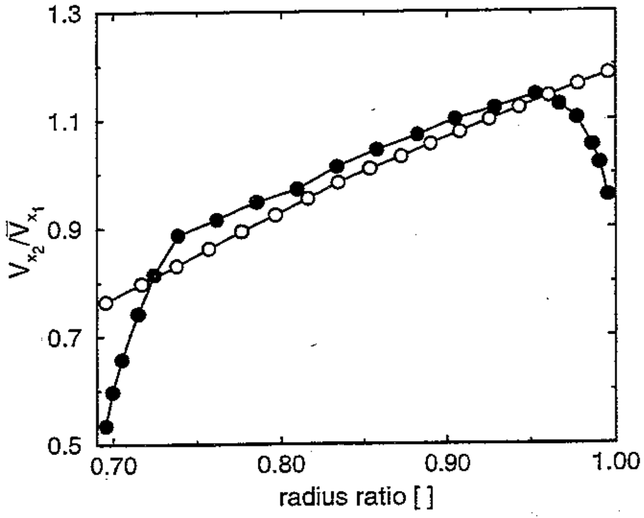

Figure 2.14: Axial velocity distribution at a flow rate of $Q = 6.31m^3/s$.
○: calculated, ●: measured.

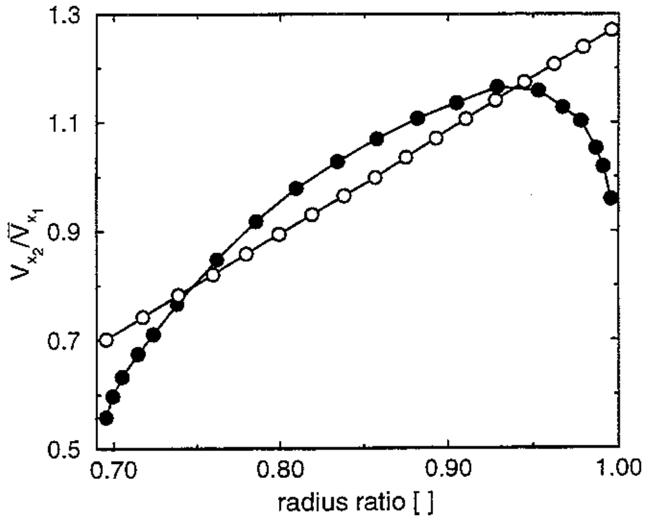

Figure 2.15: Axial velocity distribution at a flow rate of $Q = 4.45m^3/s$ (design flow rate).
○: calculated, ●: measured.

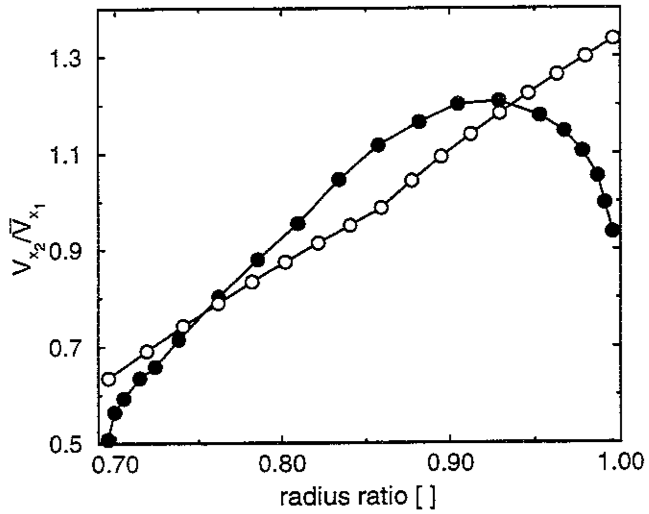

Figure 2.16: Axial velocity distribution at a flow rate of $Q = 3.79m^3/s$.
○: calculated, ●: measured.

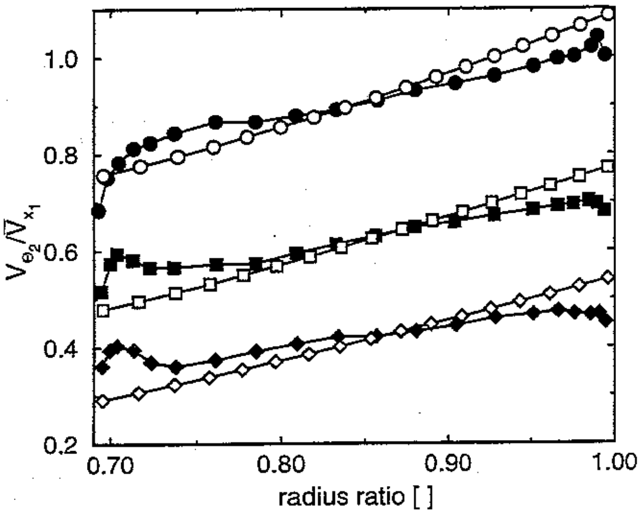

Figure 2.17: Tangential velocity distributions at three flow rates.
○: $Q = 4.45m^3/s$ (design flow rate), □: $Q = 5.41m^3/s$ ◇: $Q = 6.31m^3/s$. Filled symbols are measured values, open symbols are the calculated values.

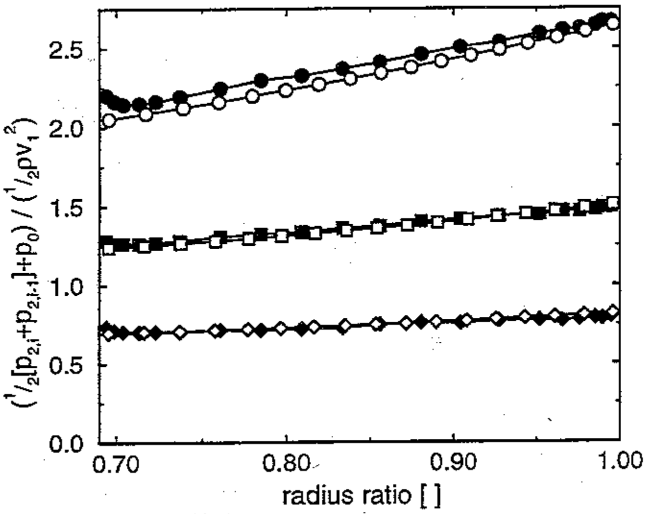

Figure 2.18: Static pressure distributions at three flow rates.
○: $Q = 4.45m^3/s$ (design flow rate), □: $Q = 5.41m^3/s$ ◇: $Q = 6.31m^3/s$. Filled symbols are measured values, open symbols are the calculated values.

2.4 Rotor-Rotor Configuration (Bell and DeKoster 1942)

In the work by Bell and DeKoster (1942), the potential of increased pressure rise capabilities of two counter-rotating rotors was investigated. Only integrated properties (pressure rise and shaft power) were measured as a function of the flow rate. The fan unit was mounted on rollers which enabled measurements of the thrust produced by the fan. The magnitude of the thrust was then used as a measure of the pressure rise. The mechanical shaft power of the individual rotors was determined by suitable calibrations of the electrical power consumed by the motors.

To enable direct comparisons, the experimental definition of pressure rise is used in the aerodynamic model. I.e., the axial force from each blade element is integrated to yield the total force on the fan unit which, when divided by the annulus, provides the pressure rise. The dimensionless parameters from Bell and DeKoster (1942) have been transformed by a density of $\rho = 1.21kg/m^3$ and a fan angular velocity of 3600 RPM.

The hub-to-tip ratio is 0.69 and identical blades, employing 12 % thick RAF 6E airfoils of constant chord length, are used for both rotors. Two configurations were investigated: one with 24 blades in both front and rear rotor and another with only 12 blades in the rear rotor. Measurements of the aerodynamic properties were performed for various blade setting angles and three cases have been chosen for the following comparisons.

Case 1 considers a rotor-only fan setup with 24 blades at a hub pitch angle of 30.5^o. Case 2 is a rotor-rotor fan setup with 24 blades at a hub pitch angle of 50.5^o in the front rotor and 24 blades at a hub pitch angle of 30.5^o in the rear rotor. Finally, case 3 is a rotor-rotor fan setup with 24 blades at a hub pitch angle of 30.5^o in the front rotor and 12 blades at a hub pitch angle of 30.5^o in the rear rotor.

As described further in section 1.5.1, airfoil data were determined by the CFD-method. For the two rotors with 24 blades, airfoil data were determined at five evenly spaced spanwise stations. Investigations of the predicted fan performance showed that a decrease from five to three spanwise stations resulted in almost unchanged performance predictions and only three spanwise stations were used for the 12 blade rotor.

In a previous study, Bell (1942) measured the performance of the 24 blade rotor in a rotor-only setup. To validate the airfoil data as well as the aerodynamic model, Fig. 2.19 depicts the shaft power of the case 1 rotor-only setup. Two curves are shown for the measured shaft power. The upper curve shows measurements in a rotor-only setup whereas the lower curve is measurements of the front rotor in a rotor-rotor configuration. Although the difference in measured shaft power is small, the rear rotor seems to influence the front rotor slightly. In the aerodynamic model, the front rotor is independent of the rear rotor and thus, the predicted shaft power should be compared to the rotor-only measurements of the rotor. Although the shaft power is slightly underestimated, a good comparison is found and thus the quality of the airfoil data predicted by the CFD-method is believed to be good. However, for flow rates above $4.5m^3/s$, the calculated shaft power bends upwards, away from the measurements. This may be explained by the airfoil data predicted by the CFD-method, described in section 1.5.1. Fig. 1.5 depicts the airfoil data used for the calculations and it seems that the lift curves bend upward for low angles of attack. This corresponds to the deviations found in Fig. 2.19,

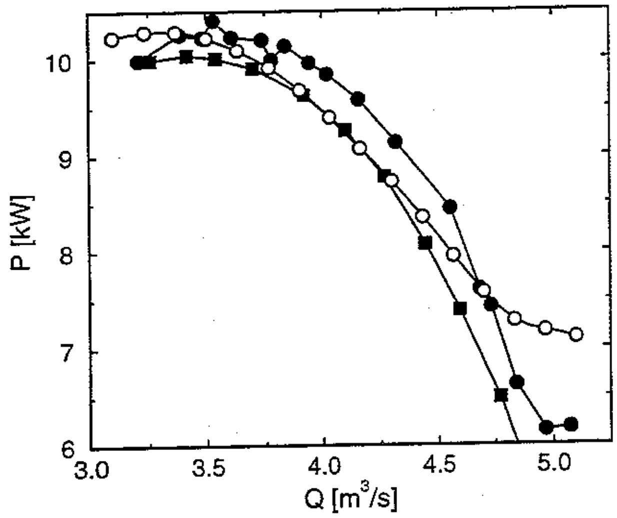

Figure 2.19: Shaft power at various flow rates of the case 1 rotor-only setup. ●: measured in a rotor-only setup from Bell (1942), Fig. 24. ■: measured in the present rotor-rotor setup with a rear rotor present. ○: calculated.

In Fig. 2.20, comparisons are made of the measured and calculated shaft powers of the case 2 rotor-rotor setup. Individual curves for the front and rear rotor are depicted as well as the total contribution for both rotors. For the front rotor, the agreement between measured and calculated shaft powers is very good for all flow rates, although slightly underpredicted at low flow rates. For the rear rotor, the calculations agree well with measured values at the low flow rate. However, for high flow rates, the shaft power tends to be overpredicted. Again, this may be explained by the low-angle region of the airfoil data for the 24 blade rotor with a hub setting angle of 30.5°, where the lift curves tend to bend upwards at small angles of attack. Although slightly underestimated at low flow rates, the summation of the individual contributions agrees well with the measurements. Again, the influence from the excessive shaft power of the rear rotor is seen for high flow rates.

Fig. 2.21 depicts the total pressure rise across the two rotors. The calculations slightly underestimate the pressure rise at low flow rates. At high flow rates, the calculated pressure rise exceeds the measurements which can be explained by the excessive lift coefficients of the rear rotor at low angles of attack. Finally, Fig. 2.22 shows the comparison of efficiency and a good agreement is found.

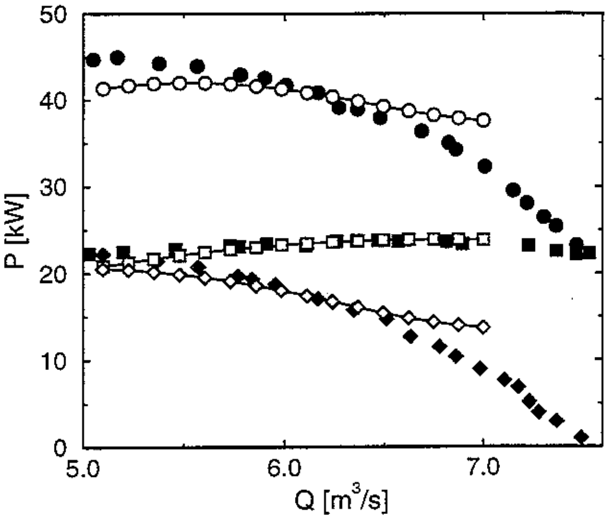

Figure 2.20: Shaft power at various flow rates of the case 2 rotor-rotor setup. ○: sum of the individual shaft powers from the two rotors. □: shaft power for the front rotor. ◇: shaft power for the rear rotor. Filled symbols are measured values, open symbols are calculated values.

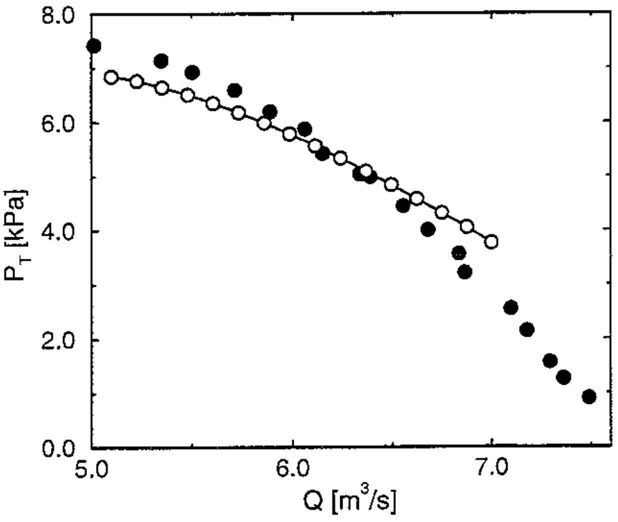

Figure 2.21: Pressure rise at various flow rates of the case 2 rotor-rotor setup. ●: measurements. ○: calculations.

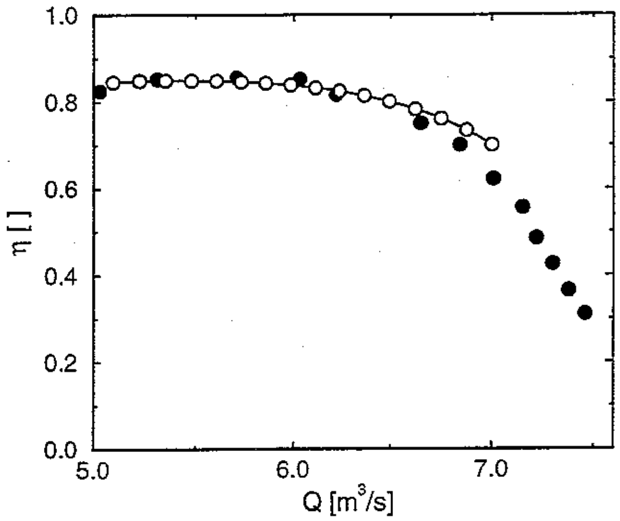

Figure 2.22: Efficiency as a function of flow rate of the case 2 rotor-rotor setup.
●: measurements. ○: calculations.

To further validate the aerodynamic model, the case 3 rotor-rotor setup is investigated. The flow rate interval, in which calculated results were found, is limited to values above $4.1m^3/s$, since lower flow rates result in a model-breakdown with too small axial velocities after the rear rotor.

In Fig. 2.23, the shaft power of the two rotors is depicted. For the lower flow rates, excellent agreement is found. However, for large flow rates, the angles of attack of the front rotor become small, resulting in excessive predictions of the lift coefficients as described previously in this section. Fig. 2.24 depicts the pressure rise across the fan unit and again, the agreement is good for the low flow rates. Finally, Fig. 2.25 shows the efficiency and, except for the high flow rates, the agreement is found to be good.

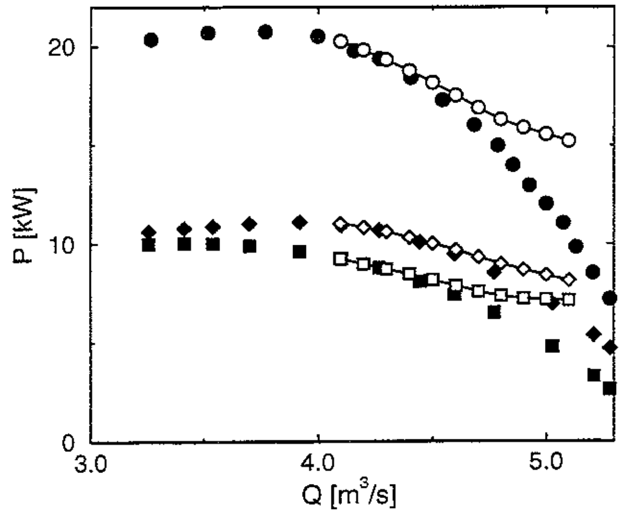

Figure 2.23: Shaft power as a function of flow rate of the case 3 rotor-rotor setup.
○: sum of the individual shaft powers from the two rotors. □: shaft power for the front rotor. ◇: shaft power for the rear rotor. Filled symbols are measured values, open symbols are calculated values.

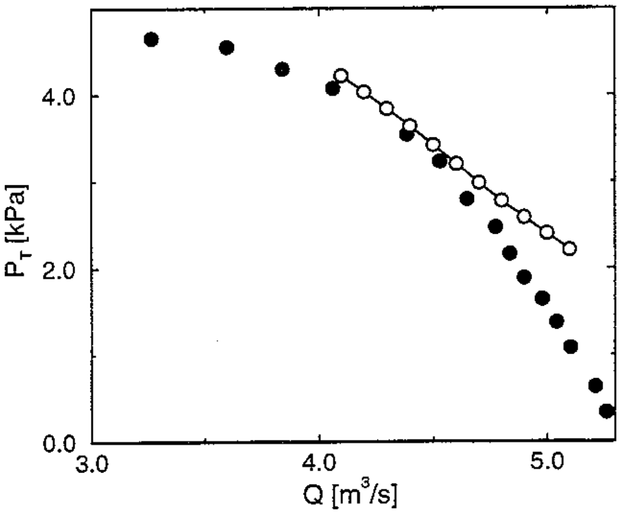

Figure 2.24: Pressure rise at various flow rates of the case 3 rotor-rotor setup.
●: measurements. ○: calculations.

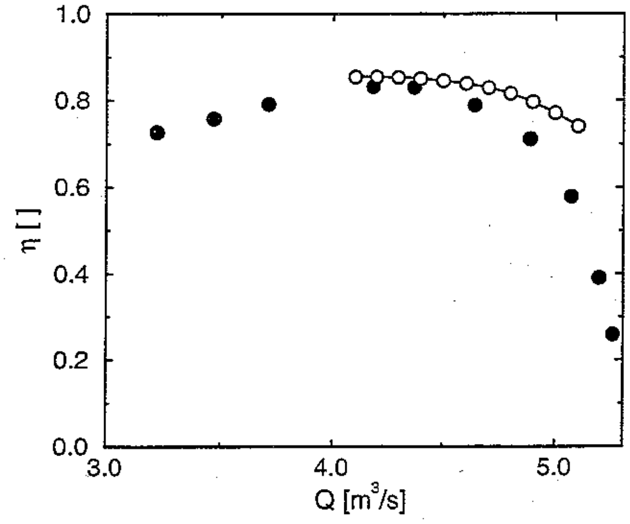

Figure 2.25: Efficiency at various flow rates of the case 3 rotor-rotor setup. ●: measurements. ○: calculations.

2.5 Stator-Rotor-Stator Configuration (Mathews *et al.* 1967)

Increased production from a mine at Mount Isa necessitated a reconstruction of the main ventilation system. The dimensioning of the ventilation system was considered in detail so as to lower the energy consumption as well as the maintenance costs. The required flow rate through the mine system is approximately $1000m^3/s$ and the pressure loss around 1000 Pa. Rather than being necessary for dust-removal, the large flow rate is required to lower the temperature of the cave areas since a high temperature gradient exists in the ground.

Besides the mine shafts, caving to the surface often occurs. Thus, air flow from the surroundings to the cave area may occur through uncontrolled openings if the fan system is designed as an exhaust system, with all fans being upcast only. Contrary, air flow from the cave area to the surroundings may occur if the fan system is designed as a pressure system, with all fans being downcast only. To circumvent either of these undesirable situations, the system was designed as a pressure-exhaust system with two downcast fans and one upcast fan. This way, near-atmospheric pressure is accomplished at the lower levels of the mine shaft system and large leakage flows are unlikely to occur (Mathews and North 1967).

A decision was made to create three identical fans. This way, both production and maintenance costs were kept at a minimum. Flexibility was an important design criterion and it was decided to create the fan systems with variable pitch rotors, thus enabling a large range of possible flow rates and pressure duties in which the fans could operate at near-maximum efficiency. The specifications required a fan total pressure rise interval of $p_T = [625, 1000]$ Pa at a flow rate of $Q = 470m^3/s$ and air density of $\rho = 1.09kg/m^3$. Noise considerations imposed the limit $\Omega = 295$ RPM on rotor angular velocity. The pitching arrangement was automatically controlled, based on pre-determined total pressure measurements in the mine shaft (Menzies and Challen 1967). To allow for a large change in blade pitch angle, the root of the blades were cut square.

In the work by Wallis (1967) and Wallis and Ruglen (1967), the design, construction and performance trials of each of the (identical) fan units are provided. The fan was designed using the free vortex flow model, and initial studies indicated that the fan outer diameter should be 6.1 m (20 feet). Furthermore, the fan stage should include a stator (prerotator) upstream of the rotor as well as a stator downstream of the rotor. Both stators were designed using C4-airfoils and the rotor was designed using a Clark Y airfoil which exhibits a flat lower surface. This enables a convenient reference surface to determine the pitch of the rotor blades.

After construction of the ventilation system, a thorough test of the aerodynamic performance was done. Traverses using pitot tubes enabled measurement of pressure and a yawmeter was used to determine the flow angle. The mechanical shaft power was determined from the power consumption of the motor by a suitable calibration.

The geometries of rotor and stators are provided in Wallis (1967). A further description of the free vortex calculations is presented in Wallis (1993). It is argued that, due to the large size of the fan unit as well as the high Reynolds number, the secondary drag constants should be altered. The constants, introduced in section 1.5.2, should be lowered to $b = 0$ for both rotor and stators and $a = 0.015$ for the rotor and prerotator. For the stator, $a = 0.018$. The same values are used in the present study.

In Fig. 2.26, the measured total pressure rise across the fan unit at three different pitch angle settings are compared to the present calculations. Although the total pressure rise is slightly overestimated, the agreement is found to be very good.

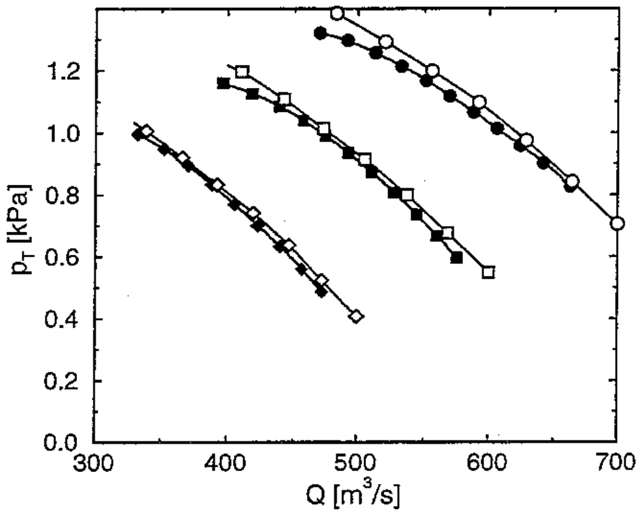

Figure 2.26: Fan total pressure rise at three rotor blade setting angles. $\rho = 1.20 kg/m^3$.
○: Setting angle 0°, □: $-4°$ and ◇: $-8°$. Filled symbols are measurements from Wallis (1967), Fig. 4, open symbols are the calculated values.

In Fig. 2.27, the efficiency is depicted. Although exhibiting the same shape as the measured values, the calculations overestimate the efficiency with approximately three percent. This might be explained by the square cutting of the blade roots. According to Wallis (1967), a $0.9m$ diameter scale model of the fan was constructed prior to the full scale fans. Tests showed that the square cutting of the blade roots resulted in an increased motor power of two to three percent compared to circular blade roots. Based on this, the predicted efficiency from Wallis (1967), using the free vortex flow analysis, were decreased with two to three percent depending on the pressure rise, to take into account the influence of the square cutting of the blade roots. Investigating Fig. 2.27, it is seen that a decrease in calculated efficiencies of two to three percent results in a very good agreement with measurements.

In Fig. 2.28, the mechanical shaft power is depicted. Generally, the shaft power is overestimated.

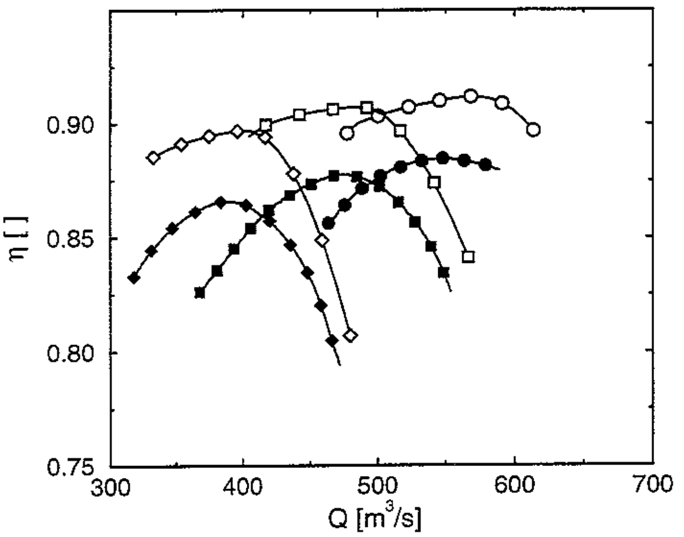

Figure 2.27: Efficiency at three rotor blade setting angles.
○: Setting angle 0°, □: −4° and ◇: −8°. Filled symbols are measurements from Wallis and Ruglen (1967), Fig. 9, open symbols are the calculated values.

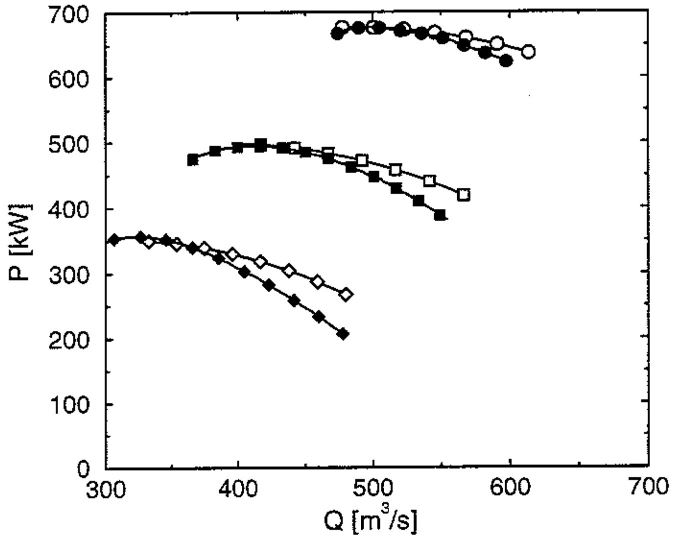

Figure 2.28: Mechanical shaft power at three rotor blade setting angles. $\rho = 1.09 kg/m^3$.
○: Setting angle 0°, □: −4° and ◇: −8°. Filled symbols are measurements from Wallis and Ruglen (1967), Fig. 7, open symbols are the calculated values.

The spanwise distribution of local tangential to axial velocity downstream of the prerotator is depicted in Fig. 2.29. A good agreement is found, although the wall boundary layers cannot be captured with the present model.

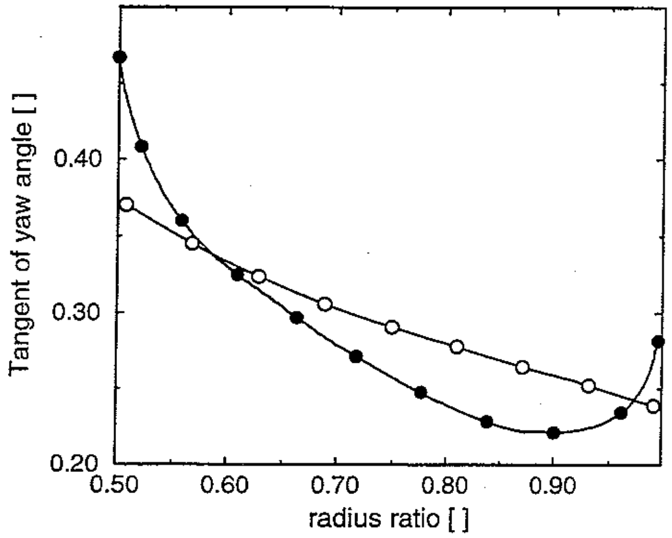

Figure 2.29: Spanwise distribution of the Ratio of local tangential to local axial velocity. The measurement position is downstream of the prerotator, before the rotor.
●: Measurements from Wallis and Ruglen (1967), Fig. 12, ○: Calculated values.

Similarly, the tangential to axial velocity ratio downstream of the rotor is depicted in Fig. 2.30. Again, the overall flow picture is captured by the model. However, it seems that the measurements are influenced more from the wall boundary layers after the rotor than after the prerotator. This agrees with the fact that a large tangential force will act on the flow in the boundary layers, where the angles of attack become large due to the lowered axial velocities.

Fig. 2.31 shows the spanwise distribution of total pressure rise downstream of the rotor, but before the stator. Again, the comparisons are good. However, confirming with the overestimation of the pressure shown in Fig. 2.26, the calculated values are in excess of the measured.

Finally, it must be emphasized that, since the fan unit is designed using the free vortex flow method, the results obtained by the present arbitrary vortex flow model are not expected to give improved results, compared to the original design data from Wallis (1967) and Wallis and Ruglen (1967). Especially since the off-design free vortex analyses are only carried out in a small interval around the design point.

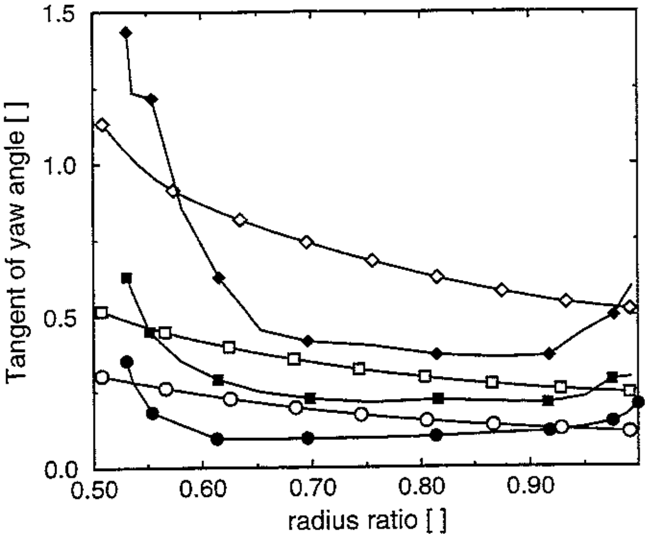

Figure 2.30: Spanwise distribution of the Ratio of local tangential to local axial velocity at three flow conditions. The measurement position is downstream of the rotor, before the stator.
○: Setting angle −2° at $Q = 411m^3/s$, □: −8° at $Q = 392m^3/s$ and ◇: −8° at $Q = 434m^3/s$. Filled symbols are measurements from Wallis and Ruglen (1967), Fig. 14, open symbols are the calculated values.

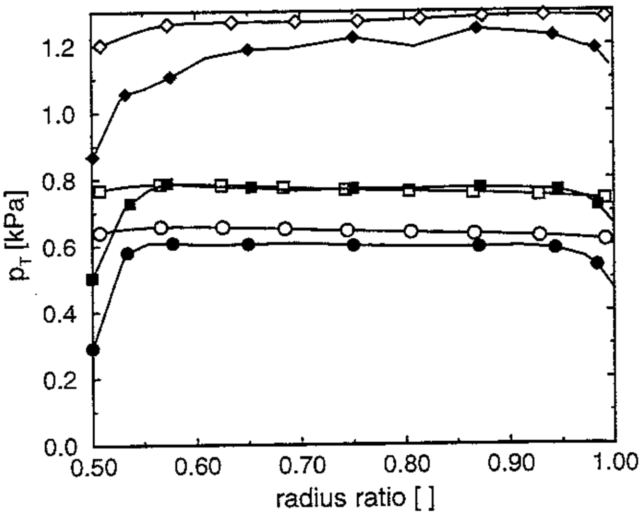

Figure 2.31: Spanwise distribution of total pressure rise at three flow conditions. The measurement position is downstream of the rotor. Although not stated, a density of $\rho = 1.09kg/m^3$ is assumed.
○: Setting angle −2° at $Q = 411m^3/s$, □: −8° at $Q = 392m^3/s$ and ◇: −8° at $Q = 434m^3/s$. Filled symbols are measurements from Wallis and Ruglen (1967), Fig. 13, open symbols are the calculated values.

2.6 Secondary Drag

As described in section 1.5.2, losses from wall shear, etc. are included in the model as a secondary drag coefficient. In this section, the influence from the secondary drag term is further discussed and a few results are given to show the dependency of the fan characteristics on the secondary drag term. Restating eq. (1.17)

$$\begin{aligned} L &= \frac{1}{2}\rho V_{rel}^2 c\Delta r_d C_L, \\ D &= \frac{1}{2}\rho V_{rel}^2 c\Delta r_d \left(C_D + C_{D,s}\right), \end{aligned} \tag{1.17}$$

it is seen that the secondary drag coefficient is added to the profile drag coefficient, resulting in an increased drag force, D, used for the calculations. Further implications of this may be found from the equations for axial and tangential forces,

$$\begin{aligned} f_x &= \frac{B\left(L\sin\beta - D\cos\beta\right)}{2\pi\bar{r}_d\Delta r_d}, \\ f_\theta &= \frac{B\left(L\cos\beta + D\sin\beta\right)}{2\pi\bar{r}_d\Delta r_d} \end{aligned} \tag{1.18}$$

For a value of β close to 90^o, $\cos\beta$ approaches zero and $\sin\beta$ unity. This implies that the axial force is basically lift dependent and that the tangential force is highly dependent on the drag force, even though the magnitude of the drag is usually much smaller than the lift force. This in turn implies that a fan blade exhibiting large stagger angles will have a tangential force which is highly dependent on the secondary drag term. On the other hand, for a low-stagger blade, the excessive magnitude of the lift force results in axial and tangential forces being almost independent on the secondary drag coefficient.

For the work by Downie *et al.* (1993), the blades of the rotors were typical fan blades, exhibiting large stagger angles, and thus the influence from the secondary drag on the tangential force is expected to be large. The calculations in section 2.3 indicated an underprediction of the efficiency and total pressure rise. It was argued that this may be attributed to the secondary drag contribution since the experimental setup was constructed to minimize all kinds of losses. To investigate this further, calculations are performed with altered expressions for the secondary drag. Besides the original calculation from Fig. 2.4, Fig. 2.32 holds three curves, calculated for a small flow rate interval, which shows predicted efficiency for changed expressions for the secondary drag. The lower of the three new curves corresponds to eq. (1.40) without influence from $\bar{C}_L$ ($a = 0$). The next curve has $b = 0$ and the upper curve has $a = b = 0$. It is found that the secondary drag contribution has a large influence on the determined efficiency. In contrast, only a small effect was found on the total pressure rise (Fig. 2.33), but the tendency for all three decreases in secondary drag is to increase the rotor total pressure rise slightly.

The above findings, combined with the uncertainty of the secondary drag contribution expressed by e.g. Wallis (1993), indicates the need for further investigation into the

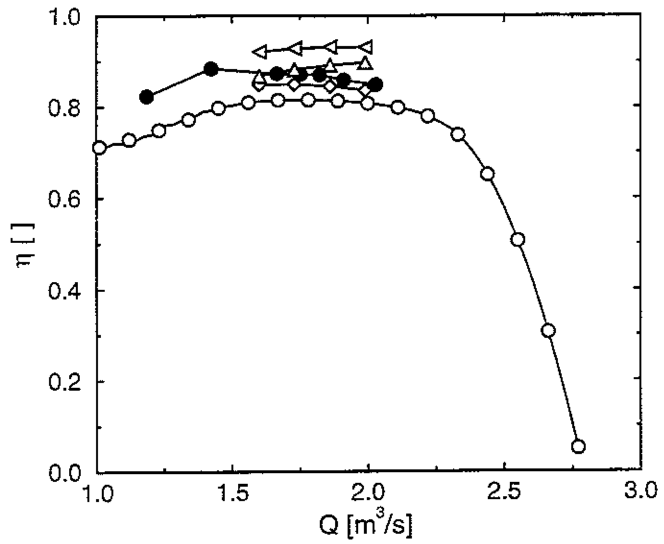

Figure 2.32: Efficiency of case 1 rotor for $\Omega = 1000$ RPM at various flow rates. Included is predicted efficiency for changed expressions for the secondary drag contribution.
●: measured, ○: calculated, ◇: calculated, $a = 0$, △: calculated, $b = 0$ and ◁: calculated, $a = b = 0$.

secondary drag contribution. It may be noted that the total omission of secondary drag in Fig. 2.32 ($a = b = 0$) results in a predicted efficiency in excess of the measured values, indicating that the secondary drag contribution should be included in some form.

Combining the analysis model with a numerical optimization program, a minimum pressure rise may be imposed as a constraint, corresponding to demands from the manufacturer. It is thus very important that the total pressure rise is well predicted by the analysis model. A reasonable property for comparing different fan designs is likely to be the efficiency. Even though the level of the efficiency is found to be dependent on the chosen expression for the secondary drag, the shape of the predicted efficiency characteristics as a function of flow rate is not likely to change very much (as can be seen from Fig. 2.32). The dependency on the secondary drag is thus approximately the same for all fan designs and it may be anticipated that the fan design found using the analysis model will be close to optimum, even though the magnitude of the efficiency may be slightly wrong.

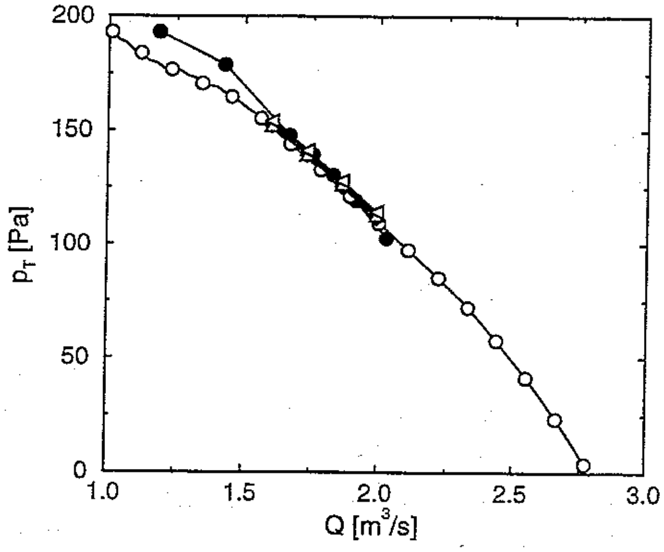

Figure 2.33: Total pressure rise of case 1 rotor for $\Omega = 1000$ RPM at various flow rates. Included is predicted total pressure rise for changed expressions for the secondary drag contribution.
●: measured, ○: calculated, ◇: calculated, $a = 0$, △: calculated, $b = 0$ and ◁: calculated, $a = b = 0$.

CHAPTER 3

Optimization Algorithm

This chapter presents the algorithm used for the optimization studies presented in the following chapters. After a brief review of the background for optimization, the sequential quadratic programming (SQP) algorithm is presented in section 3.2. Specific details of the implementation of the optimization algorithm are discussed in section 3.3.

3.1 Background

In *conventional design*, engineering experience and intuition are used to design a given product. The construction and testing of prototypes may be very expensive and time-consuming and much *trial and error* may be necessary before an acceptable design is found. Furthermore, three main problems arise when using this approach:

1. The quality of the design depends strongly on the intuition, experience and skills of the design-engineer.
2. There is no guarantee that the final design is even close to the "best" possible design.
3. Preferences of the design-engineer may exclude high-quality designs, not conforming to the generally accepted standard.

With the introduction of computer codes for analysing designs, the experimental trial and error process can be replaced by a numerical one. If the analysis model is reasonably simple, the expenses and time involved in the design process may be reduced significantly. However, the three problems listed above still apply and, furthermore, the analysis model must be valid for the range of designs investigated in the design process.

Using the computer further, the trial and error process could be replaced by an automated procedure, consisting of a number of loops which cycle through many combinations of different designs. However, even though this procedure may eliminate the three problems mentioned above, the computing time required to find an "optimum" design increases rapidly with the number of controlling (design) variables for this *exhaustive search* method.

Finally, introducing *design optimization*, a logical approach to the above exhaustive search is taken. Here, trends in the design are used to guide the optimization algorithm towards an optimum and the computing time is reduced significantly compared to the exhaustive search. The stringent mathematical formulation used in the optimization algorithm requires the designer to explicitly specify a set of design variables, a cost function to be minimized and a set of constraints, limiting the design.

It must be emphasized that validity of the analysis model is especially important in combination with a design optimization algorithm since no preferences towards traditional design-solutions exist in the process of finding an optimum. If, based on judgement of the engineer, an unrealistic optimum design occurs, additional constraints may be posed to limit the design or some of the design variables may be fixed to "traditional" values. However, this most often results in an increased cost function and thus in an inferior design, at least according to the analysis model.

After these introductory remarks, the remainder of this section is used to describe the optimization problem. Furthermore, some basic concepts for an optimum solution are introduced, and they will be used by the optimization algorithm, described in the following section.

The standard nonlinear optimization problem with nonlinear constraints can be formally stated as

$$\begin{array}{lll} \text{Minimize} & F\left(\Phi_n\right) & n = 1,2,\ldots,\text{NDV} \\ \text{subject to} & g_j\left(\Phi_n\right) = 0 & j = 1,\ldots,\text{NEQ}, \\ \text{subject to} & g_j\left(\Phi_n\right) \geq 0 & j = \text{NEQ}+1,\ldots,\text{NCON}, \end{array}$$

where NDV denotes the number of design variables and NCON the number of constraints. NEQ is the number of equality constraints. Thus, the number of inequality constraints is NCON-NEQ.

The objective function, F, describes the fitness (figure of merit) of the possible designs. The design variables, denoted by Φ_n, define the possible configurations, which can be altered by the optimizer so as to find the minimum of F. Finally, g_j denotes the constraints which describe restrictions of the designs.

The *design variables* are the parameters chosen to describe the design of a system. Assigning numerical values to all design variables results in a known design of the system. If the specified values do not satisfy all constraints of the problem, the design is *infeasible* and thus not usable. If all constraints are satisfied, the design is *feasible*. However, a feasible design is not necessarily the best.

Introducing the *objective function* enables selection of the feasible design which is the *best* according to a chosen criterion to compare various designs. The criterion is a scalar and the numerical value must be a function of the design variables. In the following, the objective function will always be minimized and thus a maximization of a function F is performed as a minimization of $-F$.

The *constraints* of the problem are introduced to exclude absurd designs (e.g. negative chord or radius). Furthermore, desired features of the optimum design can be formulated and posed as constraints (e.g. specified pressure rise or non-stalled flowconditions). All constraints must be a function of one or more design variables. If, at the optimum solution, an inequality constraint is satisfied at equality, the constraint is said to be *active*.

Before introducing some basic concepts of nonlinear constrained optimization, a few convenient conditions are stated, assumed to apply for the optimization problems solved in the following chapters. The objective function and constraints are assumed to be appropriately smooth, which typically means two times differentiable. Furthermore, at the optimum, the active constraints are assumed to be linearly independent.

In an unconstrained minimization problem, a *necessary condition* for the solution, $\boldsymbol{\Phi}^*$, is that the gradient of the objective function with respect to the design variables is zero, thus $\nabla F(\boldsymbol{\Phi}^*) = 0$. Furthermore, a *sufficient condition* for $\boldsymbol{\Phi}^*$ to be a local minimum is that the Hessian of the objective function is positive definite. The above conditions do not apply for a constrained minimization problem. Here, active constraints imply that the gradient of the objective function need not be zero at the solution. However, introducing the Lagrangian function as

$$L_F(\boldsymbol{\Phi}, \boldsymbol{\lambda}) = F(\boldsymbol{\Phi}) - \sum_{j=1}^{\mathrm{NCON}} \lambda_j g_j(\boldsymbol{\Phi}), \tag{3.1}$$

it can be shown that, besides being a feasible point, the *necessary conditions* for an optimal solution, $\boldsymbol{\Phi}^*$, is that $\nabla L_F(\boldsymbol{\Phi}^*, \boldsymbol{\lambda}^*) = 0$. Here, the Lagrangian multipliers, $\lambda_j \geq 0$ for inequality constraints and $\lambda_j = 0$ for inactive inequality constraints. If, furthermore, the Hessian of the Lagrangian function is positive definite at $\boldsymbol{\Phi}^*$, it is a *sufficient condition* for an optimum solution.

Basically, all algorithms for optimal design are iterative, and in each iteration the solution is updated as $\boldsymbol{\Phi}^{(k+1)} = \boldsymbol{\Phi}^{(k)} + \Delta\boldsymbol{\Phi}^{(k)}$, where k denotes the k'th iteration. Determination of $\Delta\boldsymbol{\Phi}^{(k)}$ is further decomposed into two subproblems as $\Delta\boldsymbol{\Phi}^{(k)} = \alpha_l^{(k)}\boldsymbol{h}^{(k)}$, where $\boldsymbol{h}^{(k)}$ is the search direction and $\alpha_l^{(k)}$ the step-length in that direction.

3.2 Method

The algorithm chosen for the solution of the problem is the sequential quadratic programming (SQP) algorithm by Han (1976), extended by Powell (1978b). The method is computationally efficient with regards to the number of evaluations of the objective function and constraints and, furthermore, the method is robust, enabling calculations of a large number of problems (Powell 1978a; Arora 1989). The present implementation of the SQP algorithm has been used successfully in Sørensen and Sørensen (1996). An outline of the algorithm is given in Fig. 3.1.

```
choose initial $\mathbf{\Phi}^{(0)}$;
$\boldsymbol{B}^{(0)} = \boldsymbol{I}$;
$\boldsymbol{\lambda}^{(0)} = \mathbf{0}$;
repeat
    determine $(\boldsymbol{h}^{(k)}, \boldsymbol{\lambda}^{(k)})$ from quadratic subproblem;
    determine $\alpha_l$ from one-dimensional linesearch;
    $\mathbf{\Phi}^{(k+1)} = \mathbf{\Phi}^{(k)} + \alpha_l \boldsymbol{h}^{(k)}$;
    find $\boldsymbol{B}^{(k+1)}$ from BFGS formula;
until convergence is achieved;
```

Figure 3.1: Outline of the algorithm for the sequential quadratic programming algorithm

The model is based on the Newton-Raphson method performed on $\nabla L_F(\mathbf{\Phi}, \boldsymbol{\lambda})$ with the following exceptions:

1. Each iteration in the Newton-Raphson method is solved as a quadratic programming problem to enable inclusion of inequality constraints in the problem.

2. The Hessian of the Lagrangian function is approximated by a positive definite matrix. The approximation is based on first derivatives only and thus, it is not necessary to perform an explicit calculation of the Hessian.

3. A linesearch is performed to avoid divergence of the iterations in the initial part of the solution.

Derivation of the Quadratic Subproblem

Before proceeding with the description of the method, the derivation of the quadratic subproblem is given (Arora 1989). Assuming that the nonlinear problem has only equality constraints, the necessary conditions for an optimum solution is recalled from the previous section as

$$\begin{aligned} \nabla L_F(\boldsymbol{\Phi},\boldsymbol{\lambda}) &= \nabla F(\boldsymbol{\Phi}) - \sum_{j=1}^{\mathrm{NCON}} \lambda_j \nabla g_j(\boldsymbol{\Phi}) = 0 \\ g_j(\boldsymbol{\Phi}) &= 0, \quad j = 1,\mathrm{NCON}. \end{aligned} \tag{3.2}$$

These are nonlinear equations so the Newton-Raphson method may be used for the solution. Introducing a compact notation and writing eq. (3.2) as $\boldsymbol{F}(\boldsymbol{y}) = \mathbf{0}$, where

$$\boldsymbol{F} = \begin{bmatrix} \nabla L_F \\ \boldsymbol{g} \end{bmatrix} \text{ and } \boldsymbol{y} = \begin{bmatrix} \boldsymbol{\Phi} \\ \boldsymbol{\lambda} \end{bmatrix}, \tag{3.3}$$

where $\boldsymbol{g}$ and $\boldsymbol{\lambda}$ are vectors containing the NCON constraints and Lagrangian multipliers, respectively. An iteration in the Newton-Raphson method involves solution of the system of linear equations:

$$\nabla \boldsymbol{F}^T(\boldsymbol{y}^{(k)})\Delta \boldsymbol{y}^{(k)} = -\boldsymbol{F}(\boldsymbol{y}^{(k)}), \tag{3.4}$$

which expands to the following system of linear equations

$$\begin{bmatrix} \nabla^2 L_F & -\boldsymbol{G} \\ -\boldsymbol{G}^T & \mathbf{0} \end{bmatrix}^{(k)} \begin{bmatrix} \Delta\boldsymbol{\Phi} \\ \Delta\boldsymbol{\lambda} \end{bmatrix}^{(k)} = \begin{bmatrix} -\nabla L_F \\ \boldsymbol{g} \end{bmatrix}^{(k)}. \tag{3.5}$$

Here, the columns in $\boldsymbol{G}$ contain the gradients of the constraints, $\nabla^2 L_F$ is the Hessian of the Lagrangian function and furthermore, $\Delta\boldsymbol{\Phi}^{(k)} = \boldsymbol{\Phi}^{(k+1)} - \boldsymbol{\Phi}^{(k)}$ and $\Delta\boldsymbol{\lambda}^{(k)} = \boldsymbol{\lambda}^{(k+1)} - \boldsymbol{\lambda}^{(k)}$.

The first equation of eq. (3.2) can be written in compact form as

$$\nabla L_F^{(k)} = \nabla F^{(k)} - \boldsymbol{G}^{(k)} \cdot \boldsymbol{\lambda}^{(k)}.$$

Inserting the above together with $\Delta\boldsymbol{\lambda}^{(k)} = \boldsymbol{\lambda}^{(k+1)} - \boldsymbol{\lambda}^{(k)}$ in eq. (3.5) eliminates $\boldsymbol{\lambda}^{(k)}$, except from the dependency in $\nabla^2 L_F$. Thus the Newton-Raphson iteration rewrites to

$$\begin{bmatrix} \nabla^2 L_F & -\boldsymbol{G} \\ -\boldsymbol{G}^T & \mathbf{0} \end{bmatrix}^{(k)} \begin{bmatrix} \boldsymbol{\Phi}^{(k+1)} - \boldsymbol{\Phi}^{(k)} \\ \boldsymbol{\lambda}^{(k+1)} \end{bmatrix} = \begin{bmatrix} -\nabla F \\ \boldsymbol{g} \end{bmatrix}^{(k)}. \tag{3.6}$$

To show that an iteration in the Newton-Raphson solver can be expressed as a solution to a certain quadratic programming problem with linear constraints, assume the problem to be defined as

$$\begin{array}{lll} \text{minimize} & Q_F(\boldsymbol{h}) \equiv \nabla F^T \boldsymbol{h} + \frac{1}{2}\boldsymbol{h}^T \nabla^2 L_F \boldsymbol{h} & \\ \text{subject to} & \nabla g_j^T \boldsymbol{h} + g_j = 0, & j = 1, \text{NCON}. \end{array} \tag{3.7}$$

The Lagrangian function for the problem in eq. (3.7) is

$$L_F = \nabla F^T \boldsymbol{h} + \tfrac{1}{2}\boldsymbol{h}^T \nabla^2 L_F \boldsymbol{h} - \sum_{j=1}^{\text{NCON}} \lambda_j \left(\nabla g_j^T \boldsymbol{h} + g_j \right) \tag{3.8}$$

and, treating $\boldsymbol{h}$ as the unknown variable and writing in compact form, the necessary conditions for an optimum solution become

$$\begin{aligned} \nabla L_F &= \nabla F + \nabla^2 L_F \boldsymbol{h} - \boldsymbol{G\lambda} = \boldsymbol{0} \\ \boldsymbol{G}^T \boldsymbol{h} + \boldsymbol{g} &= \boldsymbol{0}, \end{aligned} \tag{3.9}$$

which may be rearranged to give the same matrix form as eq. (3.6) with $\boldsymbol{h} = \boldsymbol{\Phi}^{(k+1)} - \boldsymbol{\Phi}^{(k)}$. Thus, the iterations in the Newton-Raphson method may be substituted by a quadratic programming subproblem. Furthermore, this enables inclusion of inequality constraints in the original problem.

The above implies that the quadratic subproblem to be solved in each iteration of the SQP algorithm may be written as

$$\begin{array}{lll} \text{minimize} & Q_F(\boldsymbol{h}) \equiv \nabla F^T \boldsymbol{h} + \frac{1}{2}\boldsymbol{h}^T \boldsymbol{B} \boldsymbol{h} & \\ \text{subject to} & \nabla g_j^T \boldsymbol{h} + g_j = 0, & j = 1, \text{NEQ} \\ \text{subject to} & \nabla g_j^T \boldsymbol{h} + g_j \geq 0, & j = \text{NEQ} + 1, \text{NCON}. \end{array} \tag{3.10}$$

Here, $\boldsymbol{B}$ could be $\nabla^2 L_F$ or some appropriate approximation. As described below, the SQP algorithm is defined so that $\boldsymbol{B}$ is a positive definite approximation to $\nabla^2 L_F$.

The algorithm used for solving the above quadratic programming problem is based on the work by Fletcher (1971) where $\boldsymbol{B}$ may take any form. However, since the algorithm is used to solve the quadratic subproblem from the SQP where $\boldsymbol{B}$ by definition is symmetrical and positive definite, a simplified version of the algorithm is used (Madsen 1991). Furthermore, it is assumed that the constraints are linearly independent.

The algorithm is based on the fact that a quadratic problem exhibiting equality constraints only, can be easily solved using Lagrange multiplier techniques. The algorithm works by keeping a basis of the active inequality constraints which are being treated as equality constraints, thus creating a quadratic problem with equality constraints. The minimum of the subproblem is found and if any of the inequality constraints, not in the basis, are violated at the new solution, the constraint is included in the basis. However, if the minimum does not result in any new constraints added to the basis, the Lagrange multipliers of the basis is investigated to see if any of the active inequality constraints should be removed. If this is not the case, the minimum is found. Otherwise, the constraint is removed from the basis and the process restarted.

Approximation to the Hessian of the Lagrangian Function

At a certain iteration of the SQP algorithm, ∇F, ∇g_j and g_j in eq. (3.10) are determined directly from the nonlinear problem. The actual Hessian of the Lagrangian function of the nonlinear problem could be used for $\nabla^2 L_F$, however, second derivatives must be calculated and, furthermore, the Hessian is not necessarily positive definite. Thus, rather than using the Hessian, an approximation is used which is positive definite and calculated using first derivatives only.

Denoting the approximation to the Hessian matrix of the Lagrangian function by $\boldsymbol{B}$, the determination of $\boldsymbol{B}^{(k+1)}$ is found from an update of $\boldsymbol{B}^{(k)}$ by using the BFGS formula. Experience from unconstrained minimization suggests that $\boldsymbol{B}^{(k+1)}$ depends on $\boldsymbol{B}^{(k)}$ and on the difference in gradient of the Lagrangian function

$$\gamma^{(k)} = \nabla L_{F,\boldsymbol{\Phi}}(\boldsymbol{\Phi}^{(k)} + \boldsymbol{\delta}, \boldsymbol{\lambda}^{(k)}) - \nabla L_{F,\boldsymbol{\Phi}}(\boldsymbol{\Phi}^{(k)}, \boldsymbol{\lambda}^{(k)}), \tag{3.11}$$

where $\boldsymbol{\delta} = \alpha_l \boldsymbol{h}^{(k)}$ is the change in variables, $\boldsymbol{\delta} = \boldsymbol{\Phi}^{(k+1)} - \boldsymbol{\Phi}^{(k)}$, found as the solution to the quadratic subproblem followed by a one-dimensional linesearch.

When the solution of the SQP is close to the minimum, it is reasonable to assume that the Lagrangian multipliers, $\boldsymbol{\lambda}$, from the quadratic subproblem are good approximations to the values of the original nonlinear problem. Thus, $\boldsymbol{\lambda}^{(k)}$ in the above equation is determined as part of the solution to the quadratic subproblem.

To ensure that the update of $\boldsymbol{B}$ remains positive definite, the expression from eq. (3.11) is replaced by

$$\eta = \Theta\gamma^{(k)} + (1-\Theta)\boldsymbol{B}^{(k)}\boldsymbol{\delta}, \;\; 0 \le \Theta \le 1, \tag{3.12}$$

where Θ is chosen so that η is closest to γ, subject to the condition that

$$\boldsymbol{\delta}^T\eta \ge 0.2\boldsymbol{\delta}^T\boldsymbol{B}\boldsymbol{\delta},$$

where the empirical value of 0.2 is chosen from numerical experiments. The value of Θ in eq. (3.12) is determined as

$$\Theta = \begin{cases} 1 & , \;\; \boldsymbol{\delta}^T\gamma \ge 0.2\boldsymbol{\delta}^T\boldsymbol{B}\boldsymbol{\delta} \\ \frac{0.8\boldsymbol{\delta}^T\boldsymbol{B}\boldsymbol{\delta}}{\boldsymbol{\delta}^T\boldsymbol{B}\boldsymbol{\delta}-\boldsymbol{\delta}^T\gamma} & , \;\; \boldsymbol{\delta}^T\gamma < 0.2\boldsymbol{\delta}^T\boldsymbol{B}\boldsymbol{\delta} \end{cases} . \tag{3.13}$$

Finally, the BFGS update formula is stated as

$$\boldsymbol{B}^{(k+1)} = \boldsymbol{B}^{(k)} - \frac{\boldsymbol{B}^{(k)}\delta\delta^T\boldsymbol{B}^{(k)}}{\delta^T\boldsymbol{B}^{(k)}\delta} + \frac{\eta\eta^T}{\delta^T\eta}. \tag{3.14}$$

The identity matrix, which is positive definite as well as symmetrical, is chosen as the initial value of the approximate Hessian, $\boldsymbol{B}^{(0)}$.

One-dimensional Linesearch Method

After determination of the approximation to the Hessian of the Lagrangian function, the remaining issue to complete the description of the SQP algorithm is the derivation of the one-dimensional linesearch method, used in each iteration of the algorithm. Especially in the initial iterations of the SQP algorithm, restrictions of the step-length parameter, α_l may be necessary to ensure convergence of the method.

Besides reducing the objective function, the linesearch procedure must also, in some way, include the constraints. Here, a penalty function is introduced according to Powell (1978b)

$$\Psi(\boldsymbol{\Phi}, \boldsymbol{\mu}) = F(\boldsymbol{\Phi}) + \sum_{j=1}^{\text{NEQ}} \mu_j \left|g_j(\boldsymbol{\Phi})\right| + \sum_{j=\text{NEQ}+1}^{\text{NCON}} \mu_j \left|min\left\{0, g_j(\boldsymbol{\Phi})\right\}\right|, \tag{3.15}$$

where $\mu_j \geq |\lambda_j|$ ensures decrease of the penalty function, $\Psi(\boldsymbol{\Phi} + \alpha_l \boldsymbol{h}, \boldsymbol{\mu})$ when α_l is increasing from zero. Thus, the use of the penalty function from eq. (3.15) ensures that an improved solution can be found.

The penalty factors, μ_j are initially put equal to $|\lambda_j|$. On subsequent iterations, the penalty factors are updated using

$$\mu_j^{(k)} = max\left\{\left|\lambda_j^{(k)}\right|, \tfrac{1}{2}\left(\mu_j^{(k-1)} + \left|\lambda_j^{(k)}\right|\right)\right\}. \tag{3.16}$$

To determine the step-length parameter, α_l, the function $h(\alpha_l) = \Psi(\boldsymbol{x} + \alpha_l \boldsymbol{h}, \boldsymbol{\mu})$, $\alpha_l \geq 0$ is considered. Investigation of eq. (3.15) reveals that the penalty function has derivative discontinuities whenever an equality constraint changes sign or when an inequality constraint changes from active to inactive or vice versa. If a differentiable penalty function is used, a suitable step-length is often taken as the value of α_l which ensures a decrease of the penalty function below a line starting in $h(0)$ with a slope of $k \cdot \Delta$, with e.g. $k = 0.1$ and where Δ is the slope at $\alpha_l = 0$, i.e. $\Delta = h'(0)$. However, when the penalty function is non-differentiable, this may pose problems and, rather than using the slope at $\alpha_l = 0$ for the value of Δ, the following approach is taken in which Δ is found from the linearized form of the penalty function:

Introducing the function ℓ as eq. (3.15) with all terms linearized yields

$$\begin{aligned}\ell(\alpha_l) = F(\Phi) + \alpha_l \nabla F(\Phi)^T \boldsymbol{h} + \sum_{j=1}^{\text{NEQ}} \mu_j \left| g_j(\Phi) + \alpha_l \nabla g_j(\Phi)^T \boldsymbol{h} \right| \\ + \sum_{j=\text{NEQ}+1}^{\text{NCON}} \mu_j \left| min\left\{0, g_j(\Phi) + \alpha_l \nabla g_j(\Phi)^T \boldsymbol{h}\right\} \right| .\end{aligned} \tag{3.17}$$

Defining $\Delta = \ell(1) - \ell(0)$, which is always negative, a value of α_l, which gives a suitable decrease of the penalty function, is defined as one which ensures that

$$h(\alpha_l) \leq h(0) + 0.1 \cdot \Delta \cdot \alpha_l. \tag{3.18}$$

I.e. $h(\alpha_l)$ is below a line through $h(0)$ with the slope 0.1Δ. The initial guess for α_l is $\alpha_l = 1$ which, according to the theory for the SQP algorithm, will often satisfy eq. (3.18). If this is not the case, α_l is appropriately decreased.

3.3 Implementation Details

The SQP algorithm allows infeasible designs during intermediate iterations. If the constraints are violated too much, non-physical designs may come up in the line search, e.g. negative chord. If this happens, the step length is reduced until a realistic design appears. This procedure is also applied if the Newton-Raphson method in the aerodynamic performance code diverges. This may happen if the initial guess, i.e. the solution from the previous iteration in the optimizer, is too far from the solution to the non-linear system of equations in the aerodynamic model. Since the chosen line search method results in improved solutions to the optimization problem for infinitely small (positive) step lengths, the above procedure is justifiable but may result in an increased number of iterations in the optimizer.

The algorithm requires gradients of the objective function and constraints with respect to the design variables. Explicit differentiation of the performance model is very complicated and the derivatives are evaluated approximately, using finite differences. To evaluate the gradients accurately, the central difference scheme is used rather than a one-sided difference. This means that for each iteration in the optimization algorithm, 2NDV + 1 evaluations of the aerodynamic performance must be calculated. Furthermore, in the line search algorithm, a number of evaluations may be performed to reduce the step length and thus 2NDV + 1 is the lowest number of evaluations required in each iteration of the optimizer. The fan performance model is solved to machine accuracy (in double precision) and thus a small finite difference interval may be chosen so as to ensure accurate gradient evaluation. Numerical investigations showed that a value of 10^{-8} resulted in a low number of evaluations in the optimizer.

The solution to the optimization problem may only be a local optimum. To increase the probability of finding the global optimum, several calculations are made for various initial geometries. If several local optima are found, the superior one is assumed to be the global optimum. Usually, the same optimum is found for the various initial geometries. However, two Bézier curves can exhibit almost the same shape with large differences in the Bézier polygons and thus a local minimum may be found.

To ensure robustness of the optimization algorithm, as well as a high rate of convergence, scaling is performed on the objective function, design variables and constraints.

Scaling of the objective function. For the optimizations in chapter 4, the objective function to maximize is the efficiency (defined in eq. (4.1)), which is typically larger than one half and always below one, and thus no scaling is necessary. In chapter 5, the objective function to minimize is the sound pressure level which is around 60 dB. A scaling is thus advantageous and a division by 40 seems to result in high convergence rates.

Scaling of the design variables. The chord length is expected to be around 0.05m and the angular velocity around 3000 RPM. Thus five orders of magnitude exist between the smallest and the largest design variable, and scaling is highly desirable. Here, a linear expression from Gill *et al.* (1981) is applied. The variables are scaled with the interval in which each design variable is expected to occur during the optimization. If the i'th design variable is expected to lie in the range $a_i \leq x_i \leq b_i$, the scaled design variable y_i is defined as $y_i = (2x_i - a_i - b_i)/(b_i - a_i)$, where $-1 \leq y_i \leq 1$ if x_i is within $[a_i, b_i]$

Scaling of the constraints. The constraints are scaled by dividing the constraint inequality by the constraining value (Arora 1989). Thus, e.g., the constraint for total pressure rise: $[p_T(Q) - 300]_{min} > 0$, becomes $[p_T(Q)/300 - 1]_{min} > 0$.

CHAPTER 4

Optimization for Maximum Efficiency

Here, the aerodynamic model for rotor-only axial fans is combined with the sequential quadratic optimization algorithm. Thus providing a tool for optimization for maximum efficiency. Considering rotor-only axial fans only, optimizations are carried out to illustrate various aspects of the maximization of efficiency. Following a background for the study, section 4.2 defines the optimization problem. In section 4.3, a discussion of the expected behaviour for the optimum design is given and initial investigations are carried out in section 4.4. After this the dependence of the efficiency on the number of blades (section 4.5), the design interval width (section 4.6) and the hub radius (section 4.7) are investigated. The aerodynamic performance of one of the optimum designs is investigated experimentally in section 4.8. Finally, a further optimization and experimental verification is carried out in section 4.9.

4.1 Background

Fan engineers are frequently faced with the problem of designing high-efficiency fans at a given flow rate and for a given pressure duty. Design techniques are typically based on *engineering experience*, and may involve much *trial and error* before an acceptable design is found. Integrating the concept of free vortex flow design (Wallis 1961) in the process reduces the need to build and evaluate new designs. However, the restrictions of the spanwise distributions of velocity and pressure in the free vortex flow design imply that analysis of the fan at off-design duties has only limited validity.

Few authors have investigated extensively the potential benefit of improved fan performance through modifications of the fan geometry and of the working conditions. In the work by Wallis (1968), a *stator-rotor-stator* fan stage was investigated. The system considered was of the free vortex flow type and several important parameters, e.g. lift-to-drag ratio, were fixed at reasonable values. This resulted in *explicit* expressions for efficiency and total pressure rise as a function of tip speed ratio, hub-to-tip ratio and downstream losses. Parametrical studies of efficiency and pressure rise as a function of the three variables were then carried out.

Recently, Dugao *et al.* (1996) considered numerical design optimization of a *rotor-stator* configuration for mining ventilation. Employing a free vortex flow design method, considerable improvement in efficiency was gained as compared to an existing installation. Furthermore, as an extra advantage, it was found that the noise emission from the fan installation was reduced.

A different approach was taken by Von Backström *et al.* (1996), where the minimization of the exit loss of a rotor-only axial fan in an exhaust configuration was considered. The spanwise distributions of axial and tangential velocity which fulfilled the radial equilibrium equation downstream of the rotor were considered. The objective of the optimization was then to find the distributions which minimized the exit loss while fulfilling the desired flow rate and pressure rise duty. Compared to the free vortex flow type of fan, a decrease in exit loss of up to 1.8 percent was found.

The above investigations concerned fan performance for a fixed flow rate and pressure rise, i.e. at a pre-defined *design point*. Operating the fan under other conditions was not considered and it is therefore possible that it may behave poorly away from the design point. In practice, fans often operate far from the design point and often with low efficiency Bolton (1990).

Employing an arbitrary vortex flow model, as described in chapter 1, for fan analysis enables the designer to investigate a fan operating under various conditions. Furthermore, a wide range of *design alternatives* may be tested numerically with equal validity. However, the increased degree of freedom of the arbitrary vortex flow model implies a trial and error process before an acceptable design is found. This in turn limits the number of design variations that may be investigated as well as the complexity of the geometric requirements and operating conditions for the fan.

Design optimization techniques may be used to *automate* the fan design process. Here, searching algorithms maximize the efficiency while enforcing constraints on geometry and operating conditions. Design parameters are automatically varied by the optimization algorithm and the corresponding changes in efficiency and constraints are used to determine an optimal design. Combining an optimization algorithm with the arbitrary vortex flow model enables the fan designer to investigate a large range of design alternatives in an efficient manner. Furthermore, *parametrical studies* of optimum designs for various operating conditions and geometric requirements are easily carried out.

Many fan configurations are compared in the optimization algorithm and a computationally efficient implementation of the arbitrary vortex flow model is required. In the present work, a Newton-Raphson method was used to solve the equations of the model, and solutions converged to machine accuracy are found at small computing costs (section 1.3.2). Furthermore, the validations of chapter 2 show good agreement with measurements and this model is therefore used in the present work.

The efficiency of the fan is considered over a *design interval* of flow rates rather than at a design point. This enables the design of a fan that operates well under various conditions. The fan duty and size are determined from the specific application of the fan. In the present case, the fan is to be combined with an existing heat exchanger system and the fan duty is determined by the manufacturer.

Most of the contents of the present chapter is taken from Sørensen *et al.* (1997).

4.2 Defining the Optimization Problem

Objective Function

Defining a design interval of flow rates and denoting the design interval center by Q_c and width by ΔQ, respectively, the primary goal of the optimization is to maximize the mean value, $\bar{\eta}$, of the aerodynamic fan efficiency in the design interval, $Q \in [Q_c - \frac{1}{2}\Delta Q;\ Q_c + \frac{1}{2}\Delta Q]$ $[m^3/h]$. The mean value is defined by

$$\bar{\eta} = \frac{1}{\Delta Q}\int_{Q_c-\frac{1}{2}\Delta Q}^{Q_c+\frac{1}{2}\Delta Q} \eta(Q)dQ, \tag{4.1}$$

where the efficiency of the fan at a given flow rate, $\eta = \eta(Q)$, is calculated using the model described in chapter 1. In the present work, $\eta(Q)$ is defined as

$$\eta = Q \cdot p_T/P, \tag{4.2}$$

where Q is the flow rate, $p_T = p_T(Q)$ is the total pressure rise across the rotor and $P = P(Q)$ the mechanical shaft power. Here, the total pressure rise across the rotor is determined as a spanwise integration of the total pressure rise across each streamtube. Similarly, the mechanical shaft power is determined by an integration of the lift and drag contributions. For the rotor-only configuration considered here, the dynamic pressure contained in the tangential velocity cannot be regained and is not included in the calculation of p_T. In the following, the result from the optimization, i.e. the optimum (maximum) value of $\bar{\eta}$, is denoted $\bar{\eta}_{max}$.

To evaluate the integral in eq. (4.1), the design interval is divided into N_d equally spaced flow rate evaluation-points and the efficiency, η, is calculated at each of these points. The mean value, $\bar{\eta}$, is then calculated using an accurate numerical integration method of order $O(1/N_d^4)$ from Press *et al.* (1992). The integral is constructed by fitting cubic polynomials through successive groups of four points.

Design Variables

The chosen design variables, which define the various possible fan configurations, are the hub radius of the rotor, r_0, the number of blades, B, the angular velocity of the rotor, Ω, and the spanwise distributions of chord length, $c(r)$, and pitch angle, $\phi(r)$, from the rotor plane.

The number of blades is a discrete property and thus not suitable for inclusion in the optimization procedure chosen here. Thus, separate optimizations must be performed for each blade number. In the present work, four to eight blades are considered reasonable from a practical point of view.

The spanwise distributions of chord length and pitch angle are defined using Bézier curves. The radial positions of the vertices in the Bézier polygon are fixed and distributed evenly from hub to tip, whereas the lateral movement of the vertices defines the spanwise distribution of chord and pitch. Thus, the number of design variables describing either chord or pitch corresponds to the number of vertices in the Bézier polygon.

Besides the above geometrical parameters, the type of airfoil used for the blades may also be used as a variable. For axial fan blades, at the low Reynolds numbers relevant, only limited data are available and the uncertainty of these data is large. Thus, rather than changing the airfoil type, the F-series airfoil with 2.5% nose droop is used throughout the optimizations. According to investigations carried out by Wallis (1977), this type of airfoil is suitable for axial flow fans of the size considered in the present investigation.

The performance of the fan depends also on the camber angle. Since a larger camber angle generally results in higher lift-to-drag ratios, the optimization will lead to maximizations of the camber angle. In practice, there will be an upper limit for the lift-to-drag ratio, since a larger camber angle will lead to more pronounced secondary flows (and losses) and a more abrupt stall characteristic. These effects are difficult to incorporate into the design model. Thus, rather than including the camber angle in the optimization, a reasonable spanwise distribution based on experience is prescribed, decreasing linearly from six to four percent from the hub to the tip.

Constraints

Requirements from the manufacturer determine the specifications of the fan and thereby also the constraints. These may be due either to some geometrical restrictions or to some desired property of the fan as discussed below. In the present case, we consider a situation in which the fan is to be incorporated into existing heat exchanger equipment for office ventilation with the following specifications:

- The tip radius of the fan is fixed at 14.5 centimeters.
- The total pressure rise should be above 300 Pa for all flow rates.
- The angular velocity should be below 3100 RPM.
- It should be possible to mold the rotor as a whole and thus the chord must everywhere be smaller than the interblade spacing to avoid blade overlap.

For the spanwise distributions of chord and pitch, differentiable constraints are ensured by calculating the constraints from the parameterized Bézier curve rather than from the discrete points governing the streamtube centers. In the present work, the following constraints are imposed:

Hub radius, r_0: Due to manufacturing requirements, r_0 should be larger than 5 centimeters. Furthermore, the gap between hub and tip should be larger than 4 centimeters. Thus $r_0 - 0.05 > 0$ and $r_n - 0.04 - r_0 > 0$. Here, r_n designates the tip radius of the rotor.

Chord distribution, c: Due to structural requirements, the chord should be larger than 3 centimeters, thus $[c(r) - 0.03]_{min} > 0$. An upper limit to the chord length is imposed by the requirement that blades cannot overlap if the rotor is to be molded in one piece. Thus, denoting the spacing by s, $s = 2\pi r/B$, $[s(r) - c(r)]_{max} > 0$. Since the blade is twisted, the above constraint ensures a finite gap between the blades.

Pitch distribution, ϕ: No natural restrictions apply to the pitch angle and it is bounded between 2 and 88 degrees to aid the optimization algorithm in narrowing the possible values. Thus $[\phi(r) - 2]_{min} > 0$ and $[88 - \phi(r)]_{max} > 0$.

Angular velocity, Ω: The angular velocity is not allowed to exceed 3100 RPM in order to keep the noise emission at a reasonable level. Thus $3100 - \Omega > 0$.

Total pressure rise, p_T: The designed fan must be able to produce the required total pressure rise for all flow rates in the design interval. In the present work, $p_T = 300$ Pa was chosen as a reasonable minimum pressure rise for ventilating a small office building. Thus $[p_T(Q) - 300]_{min} > 0$.

Axial velocity in outlet: As discussed in section 1.4.3, the analysis model is unreliable if very small outlet velocities are found. A constraint is imposed, ensuring that the optimum design does not result in outlet velocities less than 0.26 of the inlet velocity at any flow rate in the design interval. As described in the results section, this constraint is rarely active.

Maximum angle of attack, α_{max}: At high angles of attack, the flow on the blades may stall. This results in large unsteady forces acting on the blades, followed by fatigue problems. Furthermore, a large increase in noise emission occurs under stalled conditions (Sharland 1964). To ensure a flow which is not stalled at any flow rate in the design interval, an upper limit is imposed on the angle of attack, stating that the angle of attack must be less than one degree below the stall limit. This is also advantageous with respect to the use of airfoil data which is not well defined above α_{max}.

4.3 Expected Behaviour for an Optimum Design

The following proposed guidelines apply for an optimum design and will be further discussed later:

- The pressure rise decreases with increasing flow rate. Therefore, the pressure rise constraint applies at the highest flow rate in the design interval.
- The angle of attack on the blade increases with decreasing flow rate. Thus, the angle of attack constraint applies at the lowest flow rate in the design interval.
- Both of the above constraints are expected to be active for all optimum designs. This allows for the largest degree of freedom to maximize the efficiency, essentially by increasing the lift-to-drag ratio. For larger flow rate intervals, the constraints imposed will be hard to fulfil, leaving limited freedom to maximize the efficiency.
- The angular velocity of the rotor is expected to be maximized, resulting in large relative velocities on the blades. This enables the largest degree of freedom for the design. Furthermore, a larger angular velocity lowers the interval of the tip-speed ratio, i.e. the ratio of inflow axial to angular velocity. This in turn keeps the angle of attack on the blades close to the one with optimum lift-to-drag ratio in the design interval.

4.4 Initial Investigations

Number of Bézier vertices. As discussed in section 3.3, the number of calls to the performance analysis model in each iteration increases approximately linearly with the number of design variables. Furthermore, the number of iterations in the optimizer tends to increase with increasing number of design variables. It is thus extremely important to keep the number of vertices, N_B, in the Bézier polygons, describing chord length and pitch angle, to a minimum without sacrificing too much of the freedom of the design. Also, applying a small number of vertices decreases the possibility of finding a local minimum with the optimizer. Finally, many points in the Bézier polygons may result in large variations in the spanwise distributions of chord and pitch and thus in secondary flows around the blade, especially if constraints are active. This cannot be described by the aerodynamic model used here and hence the N_B must be kept small.

A series of optimizations was carried out for different number of vertices in the Bézier polygons for chord and pitch distributions, all with six blades and 19 points in the design interval, $Q = 2100 \pm 500 m^3/h$ and $p_T = 300$ Pa. It was found that using five vertices in the Bézier polygon results in an optimum efficiency, $\bar{\eta}_{max}$, determined within approximately 0.1% of the optimum value found using 18 vertices in the Bézier polygon, which is taken as the "true" optimum (Fig. 4.1). This accuracy is adequate and thus five vertices in the Bézier polygon is used in all of the following calculations.

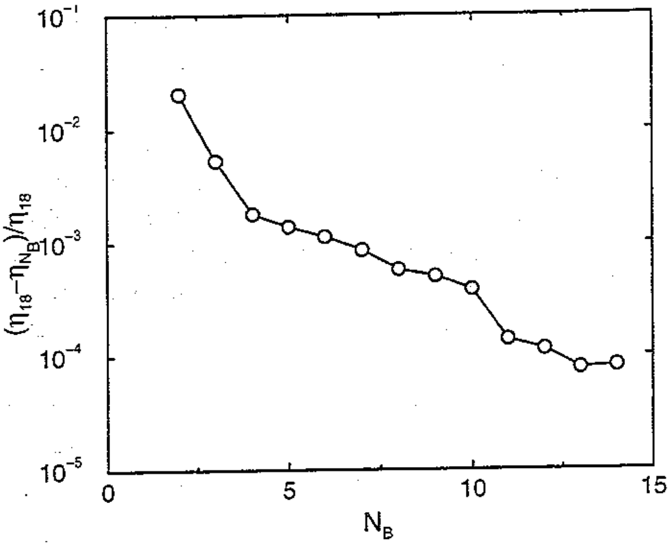

Figure 4.1: Optimum efficiency as a function of number of vertices in the Bézier polygons for spanwise chord and pitch distributions. The efficiency is depicted relative to the case $N_B = 18$, which is taken as the 'true' optimum. Performance curve divided into 19 points. Six blades, $\Delta p_T = 300$ Pa.

Number of divisions of design interval. Another important factor affecting the computational effort during optimization is the number of points, N_d, chosen to divide the design interval when evaluating the integral in eq. (4.1). A linear dependence exists between the number of points and the calculation time.

A series of optimizations employing six blades, $Q = 2100 \pm 500m^3/h$, $p_T = 300$ Pa and varying number of divisions was carried out and it was found that $N_d = 13$ points sufficed to determine $\bar{\eta}_{max}$ within 0.01% of the exact value, which is taken as the one found using 99 points (Fig. 4.2). This is adequate to ensure that the optimum design is essentially independent of the number of divisions. Thus $N_d = 13$ points are used in all of the subsequent calculations of $\bar{\eta}$.

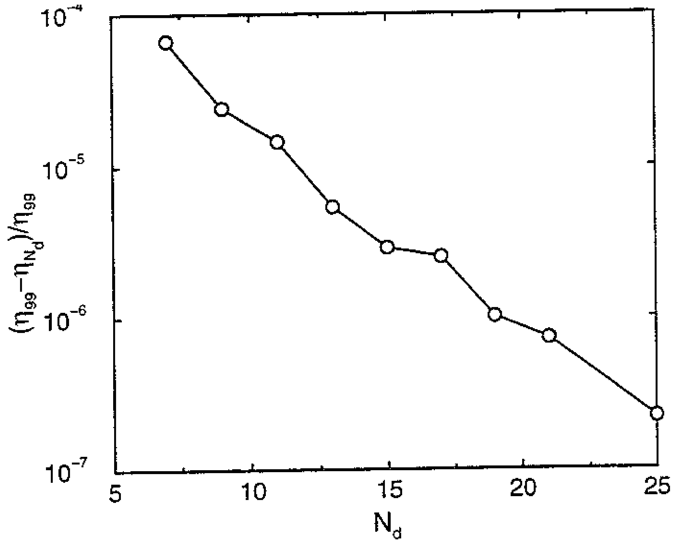

Figure 4.2: Optimum efficiency as a function of the number of divisions of the design interval, N_d. The efficiency is depicted relative to the case of $N_d = 99$ which is taken as the 'true' optimum. Number of Bézier vertices is five. Six blades, $\Delta p_T = 300$ Pa.

4.5 Dependence on Number of Blades

To investigate the dependence of the optimum efficiency, $\bar{\eta}_{max}$, on the number of blades, a series of optimizations was carried out using four to eight blades. For the investigation described in this section, the design interval of interest is set at $Q = 2100 \pm 500m^3/h$. In Table 4.1, $\bar{\eta}_{max}$ is depicted with the number of blades used. Furthermore, the hub-radius and angular velocity for the optimum designs are given.

Table 4.1: Optimization for maximum efficiency, $Q = 2100 \pm 500m^3/h$: Summary of optimum mean value of efficiency, hub radius and angular velocity for four to eight blades.

No. of blades	$\bar{\eta}_{max}$	*Hub radius* (cm)	*Angular velocity* (RPM)
4	0.602	8.90	3100
5	0.635	9.01	3100
6	0.656	9.07	3100
7	0.672	9.12	3100
8	0.684	9.18	3100

In accordance with the introductory remarks in section 4.3, the maximum angular velocity of the rotor allowed was achieved for all optimizations. Furthermore, both the pressure rise constraint and the angle of attack constraint were found to be active. The axial velocity constraint was not active for any of the optimizations.

To enable the pressure rise at the high flow rate, the spacing constraint was active in all cases at the inboard section of the blade. Also, the hub radius was found to be almost constant which indicates that it is determined by the requirement of the constraints. In Fig. 4.3, the chord distributions for four, six and eight blades are shown and the constrained chord at the hub can be seen. In Fig. 4.4, the corresponding optimum pitch distributions are depicted.

As will become evident in section 4.6, $Q = 2100 \pm 500m^3/h$ is almost the broadest design interval possible when the constraints must be met. For more narrow design intervals, investigated in section 4.7, the optimum hub radius was found to increase with increasing number of blades.

From Table 4.1, $\bar{\eta}_{max}$ is seen to increase with increasing number of blades. This is generally found for all designs and is due to the following component of the secondary drag term in the aerodynamic model (eq. (1.40)):

$$C_{D_s} = \ldots + bc/(\sigma[r_N - r_0]) = \ldots + 2b\pi r/(B[r_N - r_0]). \qquad (4.3)$$

Here, b is a positive constant, r is the radius at the blade element, r_0 and r_N the hub and tip radius, respectively, and σ is the solidity, $\sigma = c/s$. It is readily seen that the secondary

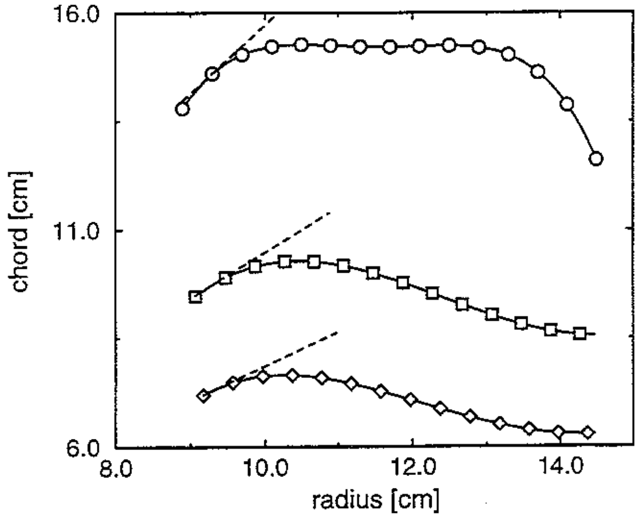

Figure 4.3: Chord distribution for the optimum designs found in section 4.5. $Q = 2100 \pm 500m^3/h$. Dotted lines show the constraint ensuring chord less than spacing.
○: four blades, □: six blades, ◇: eight blades.

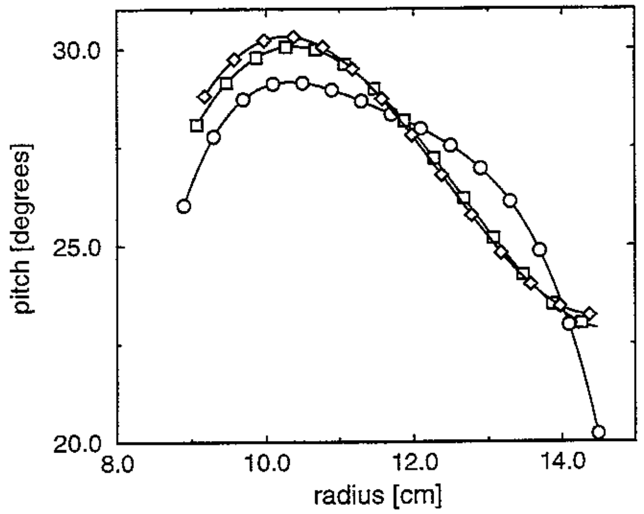

Figure 4.4: Pitch distribution for the optimum designs found in section 4.5. $Q = 2100 \pm 500m^3/h$.
○: four blades, □: six blades, ◇: eight blades.

drag decreases with increasing number of blades. Furthermore, a decrease in hub radius results in a decreased secondary drag term. This is further discussed in section 4.7. If the above term is removed in the evaluation of the secondary drag, the optimum efficiency is independent of the number of blades. This statement is based on the assumption that airfoil data are independent of the Reynolds number which decreases for smaller chords.

As an example, the calculated efficiencies, $\eta(Q)$, for the computed optimum designs is shown in Fig. 4.5 for four, six and eight blades. In all three cases, the maximum efficiency occurs within the design interval. The corresponding pressure distributions (not shown) are almost coincident since they all intersect at $p_T = 300$ Pa for $Q = 2600 m^3/h$ and the slope of the pressure distributions is almost independent of the number of blades.

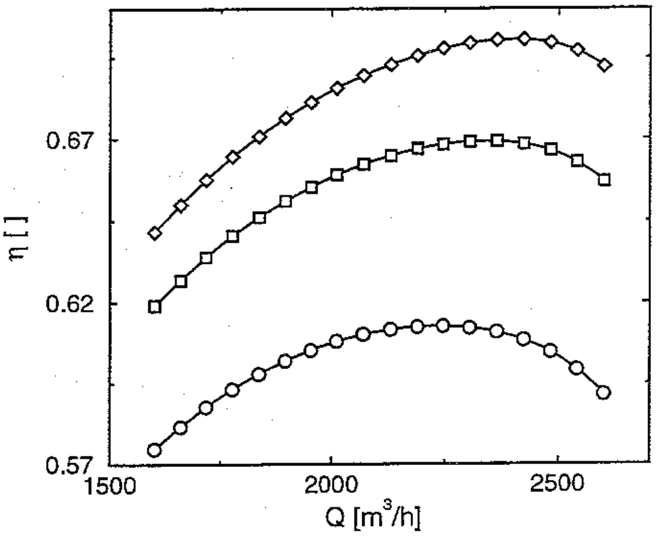

Figure 4.5: Efficiency as a function of flow rate for the optimum designs found in section 4.5. Design interval $Q = 2100 \pm 500 m^3/h$.
o: four blades, □: six blades, ◇: eight blades.

4.6 Dependence on Design Interval Width

In order to clarify the dependence of optimum efficiency, $\bar{\eta}_{max}$, on the width of the design interval, a series of optimizations was carried out for various values of ΔQ. The center of the design interval was $Q_c = 2100m^3/h$ for all cases. In Fig. 4.6 the results for four, six and eight blades are shown. For large ΔQ, a rapid decrease in efficiency is seen. Here, the constraints are difficult to meet and thus only limited freedom to maximize the mean value of the efficiency exists. Especially, it may be noted that $\Delta Q = 1000m^3/h$ is close to the maximum possible value and thus the designs described in section 4.5 are highly constrained. Conversely, for small ΔQ, $\bar{\eta}_{max}$ is seen to be only weakly dependent on ΔQ. Thus an axial fan which operates well in a design interval of e.g. $\Delta Q = 400m^3/h$ has a decrease in $\bar{\eta}_{max}$ of only about 0.02 compared to the case of $\Delta Q = 0m^3/h$. This indicates that axial fans with improved characteristics for stall, etc., may be designed with the present method.

For ΔQ larger than the values shown in Fig. 4.6, it was not possible to obtain a feasible design. For the largest flow rate interval resulting in a solution, the geometry of the rotor is completely determined by the constraints and thus independent of the objective function used.

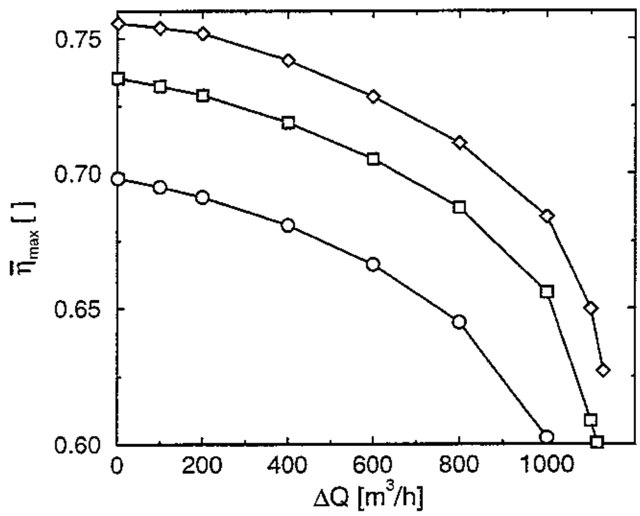

Figure 4.6: Optimum efficiency as a function of design interval width, $Q = 2100m^3/h \pm \frac{1}{2}\Delta Q$.
○: four blades, □: six blades, ◇: eight blades.

4.7 Dependence on Hub Radius

In the previous sections, $\bar{\eta}_{max}$ was found without considering the mixing losses downstream of the rotor, except for the secondary drag term discussed in section 4.5. According to Wallis (1968), the magnitude of the mixing losses in the downstream diffusor is very uncertain, but can be of a considerable size. The downstream losses will typically increase with increasing hub radius and, furthermore, the losses depend on the length and design of the tail fairing. The influence from the hub radius is partly expressed in the secondary drag (eq. (4.3)), but the length and design of the tail fairing is not included in the model. An investigation of the sensitivity of the efficiency to the hub radius may aid the designer in choosing a hub radius for a known downstream construction.

A series of optimizations for varying hub radius, r_0, has been performed and in Fig. 4.7, the efficiency as a function of hub radius is shown for four, six and eight blades. To ensure a reasonable freedom in the design, the flow rate interval is narrowed to $Q = 2100 \pm 200 m^3/h$. For all three cases examined, the chord is constrained due to the spacing requirement for the case of $r_0 = 6$ and 7 centimeters. Also, for $r_0 = 6$ centimeters, the constraint ensuring a reasonable value of the axial velocity at the outlet was active for all three cases.

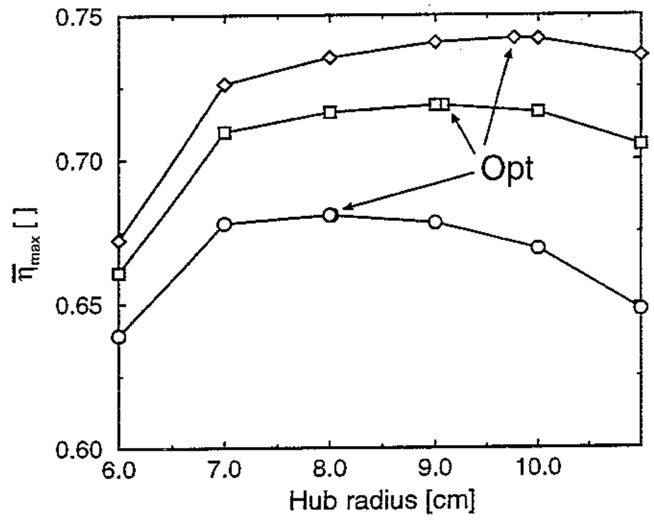

Figure 4.7: Optimum efficiency as a function of hub radius. $Q = 2100 \pm 200 m^3/h$.
o: four blades, □: six blades, ◇: eight blades. Points designated *Opt* are $\bar{\eta}_{max}$ values found from the investigations described in section 4.6. Here, the hub radius was included as a variable in the optimization.

Two competing effects influence the finding of an optimum hub radius. For larger values of r_0, the secondary drag term is large and thus a decrease in the hub radius results in an increased $\bar{\eta}_{max}$. The contrary is experienced at small hub radii. Here, a decrease in hub radius results in a decreased $\bar{\eta}_{max}$ value because the constraints are difficult to satisfy and thus the solution is more or less fixed without the possibility of increasing $\bar{\eta}_{max}$.

Examining Fig. 4.7, it is seen that for the rotor with eight blades, the hub radius can be reduced from approximately ten to seven centimeters with a loss in efficiency of only two percent. For the case of six blades, a two centimeter decrease in hub radius is possible with a reduction of only one percent in efficiency. Finally, for four blades, a reduction of one centimeter is possible with almost no penalty on the efficiency. Summing up, it is seen that $\bar{\eta}_{max}$ is only weakly dependent on the hub radius and it may therefore be feasible to specify a small hub radius rather than include the hub radius as a variable in the optimization.

It must be emphasized that if a larger design interval is required, there are fewer possibilities in specifying the hub radius since the constraints are more difficult to meet.

4.8 Experimental Verification of Optimum Design - First Case

To investigate the validity of the defined optimization problem as well as the aerodynamic model, one of the optimum designs were selected for experimental verification of the aerodynamic performance. The hub and blades were manufactured in aluminium at the Danish Institute of Technology where the measurements were carried out under supervision of M. Sc. (Mech. Eng.) C. Drivsholm. The experimental setup was constructed according to the recently published International Standard ISO 5801 (1997).

The most important quality of the fan, when combined with the heat exhanger equipment, is high efficiency and pressure rise in a large interval of flow rates. It was thus decided to create a prototype of the fan employing eight blades from section 4.5. The fan was optimized for high efficiency in a design interval of $Q = 2100 \pm 500m^3/h$.

The experimental setup has a long shaft, supported in both ends, from the motor to the fan rotor. During startups, the angular velocity passed through eigenmodes of the shaft which resulted in a large bending of the shaft. Due to this, an oscillating motion of the hub and rotor-blades occured and the latter collided with the outer casing. To circumvent this, it was necessary to sand the tips considerably. After sanding, the tip clearance was approximately two millimeters.

As summarized in Table 4.1, the optimum hub radius is 9.18 centimeters and the fan should be running at 3100 RPM. The spanwise distributions of optimum chord and pitch are depicted in Figs. 4.3 and 4.4, respectively. Due to manufacturing difficulties, the trailing edge of the blades had to be rounded with a radius of 0.25 millimeters. Thus, the chord is slightly smaller than determined by the optimization. However, the calculated results have not been changed accordingly since this is less than one percent of the chord length.

As described in section 1.5.1, the lift and drag coefficients, used for the optimizations, were obtained by correcting isolated airfoil data for solidity and stagger effects. However, due to the large discrepancies between measurements and calculations, a second set of airfoil data was created using the CFD-method of the airfoils in cascade. In the following, comparisons of measured and calculated characteristics of the fan are carried out and two curves are depicted for the calculations. One using the corrected isolated data and one using the calculated airfoil data from the CFD-method.

In Fig. 4.8, the measured and calculated shaft power are depicted as a function of flow rate. Both calculations of the shaft power are much too high and, although the lift coefficients predicted by the two methods are highly different, the integrated shaft power by the two sets of airfoil data are almost the same.

Fig. 4.9 depicts the measured and calculated pressure rise of the fan. Again, the calculated results are in excess of the measurements. Finally, Fig. 4.10 shows the measured and calculated fan efficiency and the calculations are seen to predict efficiencies above the measurements.

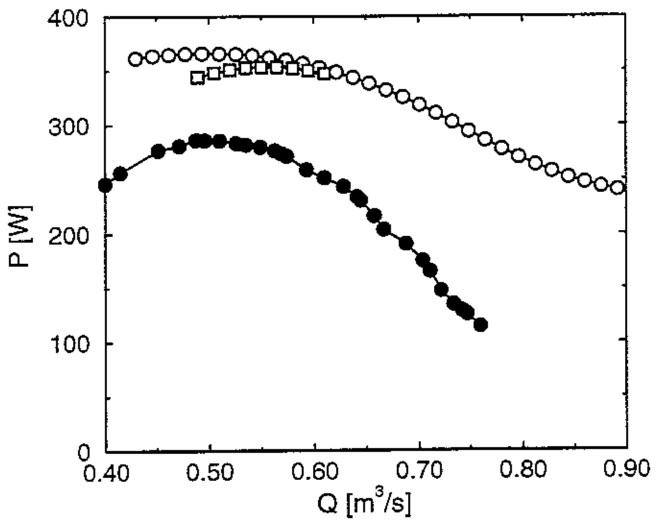

Figure 4.8: Shaft power as a function of flow rate.
●: measurements, ○: calculations using corrected isolated airfoil data, □: calculations using airfoil data from the CFD-method.

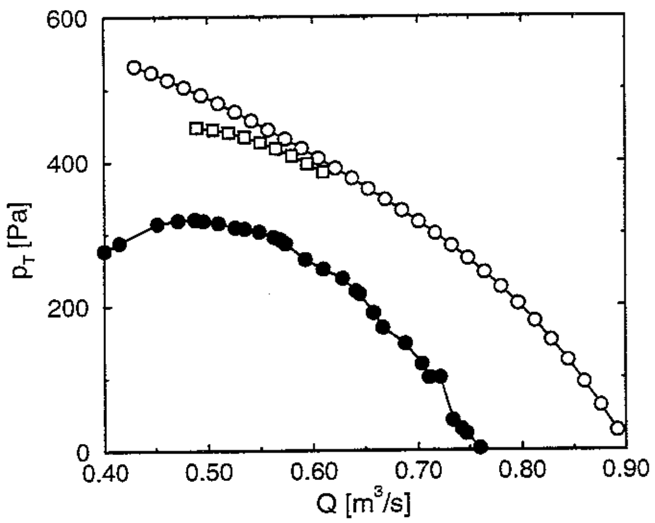

Figure 4.9: Pressure rise as a function of flow rate.
●: measurements, ○: calculations using corrected isolated airfoil data, □: calculations using airfoil data from the CFD-method.

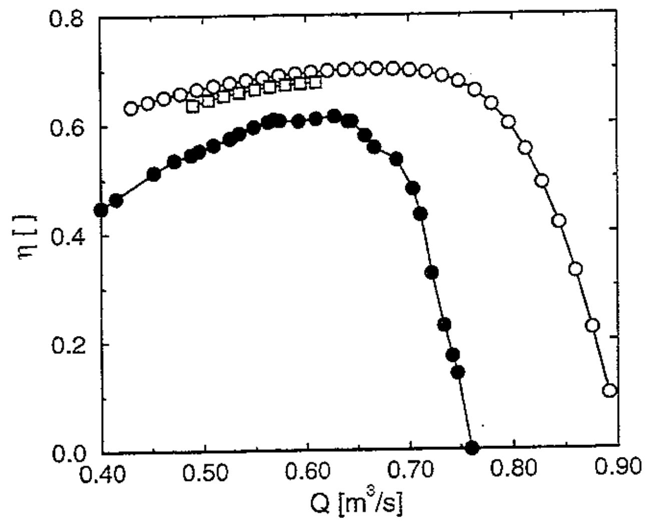

Figure 4.10: Fan efficiency as a function of flow rate.
●: measurements, ○: calculations using corrected isolated airfoil data, □: calculations using airfoil data from the CFD-method.

A possible explanation for the large discrepancies between measured and calculated fan performance may be found in the tip clearance. According to Wallis (1993), a tip clearance of more than one percent of the blade span may decrease efficiency and pressure rise of a fan considerably. In the present case, a tip clearance of two millimeters corresponds to 3.7% of the blade span.

The decrease in total pressure rise for three fan configurations, due to tip clearance, is provided in Fig. 10.3 of Wallis (1993). According to the figure, a tip clearance of 3.7% blade span results in a decrease in pressure rise of approximately 15%. Furthermore, for a free vortex fan, the following expression for the decrease in efficiency is suggested by Wallis:

$$\Delta\eta = 2\left(\frac{\text{tip clearance}}{\text{blade span}} - 0.01\right), \tag{4.4}$$

resulting in an efficiency decrease of 5.4% for a tip clearance of 3.7% blade span.

Employing the corrections for pressure rise and efficiency on the calculated performance curves results in Figs. 4.11 and 4.12 for the pressure rise and efficiency, respectively. Although a considerable improvement in the calculated results is found, the calculated efficiency and pressure rise are still in excess of the measurements.

The above tip clearance corrections apply mainly for free vortex fans, for which a constant total pressure rise occurs along the blade. For the present rotor, the predicted total pressure rise increases with increasing radius and thus, a larger total pressure rise occurs at the tip of the blades. It is thus possible that the tip clearance losses exceed the proposed values from Wallis (1993). However, a thorough investigation of the influence of tip clearance on different spanwise pressure rise distributions must be performed before any conclusions can be drawn.

Finally, it must be emphasized that effects from non-uniform inflow, wall boundary layers, etc., may also result in discrepancies between measured and calculated fan characteristics. However, besides the measurements described in the following section, the experimental setup has only been used for the above fan-unit. Effects from non-uniform inflow, etc. can thus not be quantified.

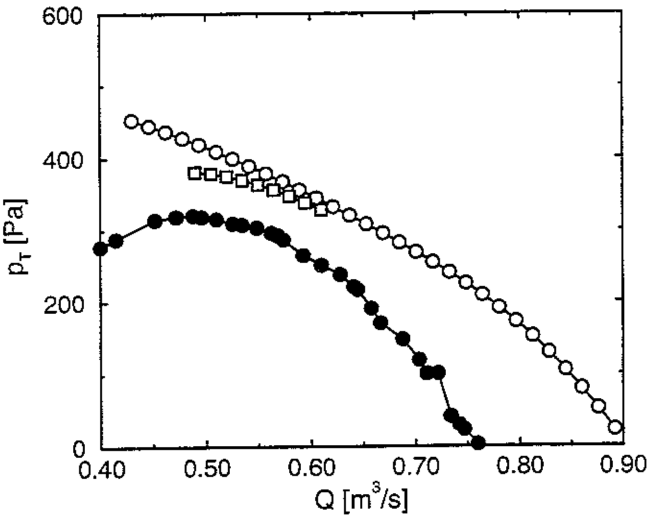

Figure 4.11: Pressure rise, with a decrease of 15% in the calculated performances due to tip clearance, as a function of flow rate.
●: measurements as in Fig. 4.9, ○: calculations using airfoil data from corrected isolated airfoil data, □: calculations using airfoil data from the CFD-method.

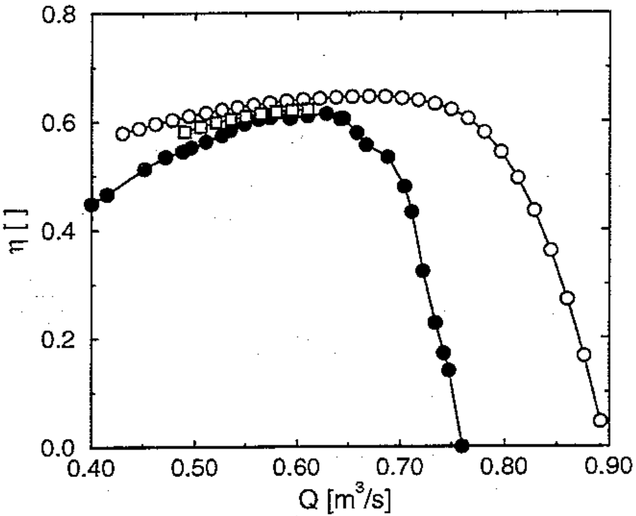

Figure 4.12: Fan efficiency, with a decrease of 5.5% in the calculated performances due to tip clearance, as a function of flow rate.
●: measurements as in Fig. 4.10, ○: calculations using airfoil data from corrected isolated airfoil data, □: calculations using airfoil data from the CFD-method.

4.9 Experimental Verification of Optimum Design - Second Case

Due to the poor agreement between measured and calculated fan performance in section 4.8, it was decided to design another fan rotor for experimental verification. Based on the discussions in section 1.5.1, the validity of the airfoil data for the F-series airfoil is questionable. Therefore, the new rotor was designed using the NACA 65-(12)10 airfoil and measured lift and drag data from Herrig *et al.* (1951) were used for the calculations.

To limit the expences, the hub-diameter was fixed at 9.18 centimeters, thus enabling a reuse of the hub created for the measurements of section 4.8. Furthermore, rather than cutting the blades in aluminium, they were moulded in an epoxy compound. Thus, these blades are more fragile than the aluminium blades, used in the previous section.

The design interval of flow rates was limited to $Q = 2100 \pm 200 m^3/h$, with a lower limit of $p_T = 300$ Pa on the pressure rise (excluding tangential velocity). To avoid excessive extrapolation of the airfoil data, the angular velocity of the rotor was fixed at 2521 RPM. The chord length of the eight blades was fixed at 10 centimeters along the span, resulting in a solidity of 1.39 at the root and a solidity of 0.88 at the tip of the blade. The only variable in the optimization was the spanwise pitch of the blade. For simplicity, a linear distribution of pitch was chosen. Although severly restricting the degree of freedom of the optimum solution, the above choices were made to enable a simple construction of the blades. Furthermore, the geometry of the moulded blades could easily be investigated for inconsistencies, regarding both airfoil shape and blade shape. To conclude, the optimization was carried out with only two design variables, namely root and tip pitch angle.

As described in section 4.2, constraints were imposed on the minimum and maximum pitch angle. Furthermore, the constraint ensuring a pressure rise of 300 Pa was used. Also, the minimum value of axial velocity was constrained as described in section 4.2. The measured airfoil data from Herrig *et al.* (1951) are depicted as a function of free-stream inlet angle and the maximum inlet angle corresponds approximately to stalled conditions on the blades. Rather than imposing a constraint on the angle of attack at maximum lift, a constraint was added which ensured that the used airfoil data were always within the measurements of the inlet angle. Thus, a total of five constraints restrict the optimization problem.

Carrying out the optimization resulted in a root pitch angle of 44.0^o and a tip pitch angle of 26.7^o. The optimum mean value of efficiency in the design interval, $\bar{\eta}_{max}$, was 0.638. Compared to $\bar{\eta}_{max} = 0.684$ for the rotor investigated in the previous section, this seems rather small. Especially since the width of the design interval was lowered from $Q = 2100 \pm 500 m^3/h$ to $Q = 2100 \pm 200 m^3/h$. However, the smaller angular velocity of the rotor (2521 RPM as opposed to 3100 RPM) combined with the lowered number of design variables restricts the degree of freedom of the design. However, this is acceptable since the main emphasis of the present design was to create a set of blades with experimentally obtained airfoil data and, furthermore, the geometry of the blades should be verifyable.

During the experimental verification of the fan performance it was found that a tip clearance of as much as four millimeters was necessary to avoid destruction of the fragile blades during startup of the rotor. Thus the ratio of tip clearance to blade span is as high as 7.5%. The correction for the decrease in total pressure rise due to tip clearance (Wallis 1993) has a limit of the ratio at 5.0% and extrapolations were necessary to determine suitable corrections for the present rotor. Accordingly, it was found that the efficiency of the fan should be decreased by 13% and that the fan pressure rise should be decreased by 35%

In Figs. 4.13-4.15, comparisons between measured and calculated shaft power, pressure rise and efficiency of the optimum rotor are depicted. Furthermore, calculated curves, corrected for tip clearance are shown. Again, the originally calculated performances are in excess of the measured. However, employing the corrections seems to yield satisfactory results for pressure rise and efficiency.

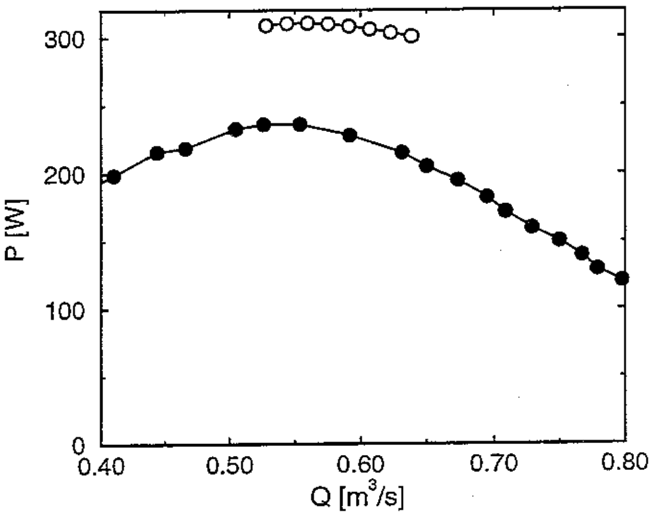

Figure 4.13: Shaft power as a function of flow rate.
●: measurements, ○: calculations.

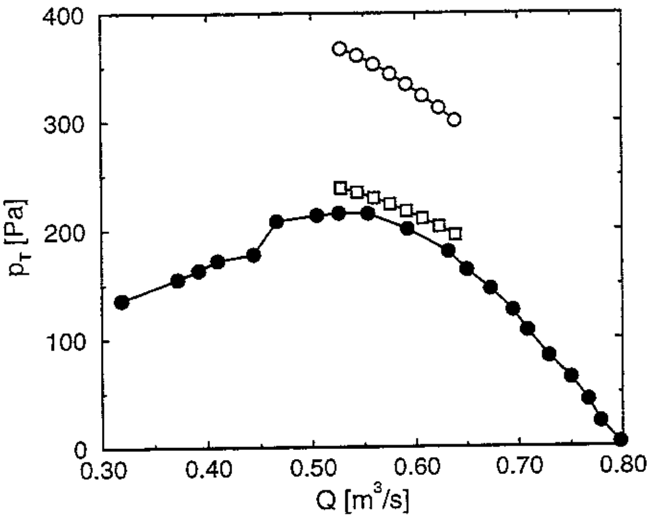

Figure 4.14: Pressure rise as a function of flow rate.
●: measurements, ○: calculations. □: calculations with a decrease of 35% due to tip clearance.

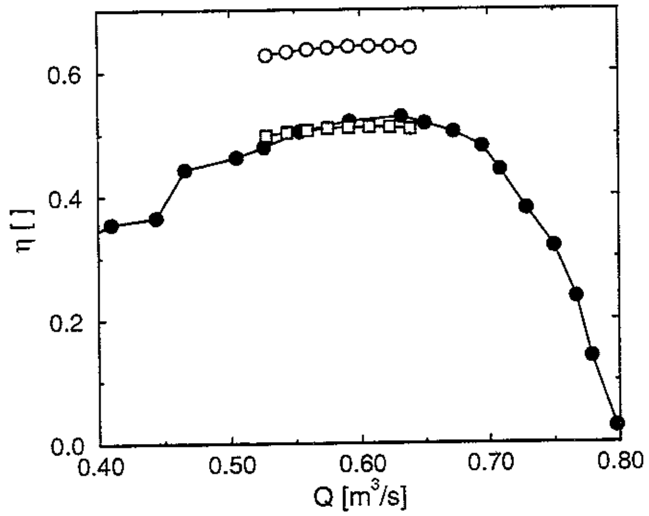

Figure 4.15: Efficiency as a function of flow rate.
●: measurements, ○: calculations. □: calculations with a decrease of 13% due to tip clearance.

CHAPTER 5

Optimization for Minimum Vortex Shedding Noise

In this chapter, the aerodynamic model from chapter 1 is combined with a model for the broad-band noise caused by vortex shedding from the trailing edge of the rotor blades. This provides a tool which predicts performance as well as noise emission from the fan. Limiting the investigations to rotor-only axial fans and integrating the models with the optimization scheme, optimizations are carried out to illustrate different formulations for the minimization of vortex shedding noise. In section 5.1, a review of some of the noise generating mechanisms is provided and section 5.2 defines the optimization problem. In section 5.3 a discussion of the expected behaviour for the optimum design is given. In section 5.4, optimizations for minimum noise, maximum efficiency and minimum angular velocity is performed and comparisons of the achieved designs are made. The influence on the minimum vortex shedding noise of constraining the efficiency is investigated in section 5.5. Finally, in section 5.6, the hub radius is excluded as a design variable and the minimum vortex shedding noise is found for fixed values of the hub radius.

5.1 Background

In recent years, low noise emission has become a highly competitive factor in the purchase of fan equipment and fan engineers frequently face demands for design of low-noise fans from manufacturers as well as consumers. The noise generating mechanisms are very complicated and a thorough analysis of sound spectra from a given fan either involves extensive measurements or time-consuming calculations.

Identification of noise generating mechanisms, followed by guidelines for reductions, has been investigated by many researchers. Basically it has been found that the aerodynamic noise emission can be divided into two different types.

The *periodic* (or rotational) noise emission has discrete frequency peaks in the noise spectrum at the blade passing frequency and its harmonics. Some of the most important sources of periodic noise emission, as well as means of reducing them, have been identified as:

- *Upstream obstacles*, e.g. struts or a row of stators. Locally, these change the magnitude and direction of the flow velocity, resulting in varying angle of attack on the rotor. This in turn results in a periodic lift force and the production of a discrete frequency noise emission. Considering fans of the rotor-only type, all upstream influences can be removed by supporting the hub downstream of the rotor (Doak and Vaidya 1969).

- *Downstream obstacles*. Downstream of the rotor, the wake will influence obstacles in the same way as discussed above. For rotor-only configurations, the distance from the rotor to the supporting struts may be increased considerably in order to reduce the velocity-deficit in the rotor-wake and thus the noise emission. Noise emission from downstream obstacles is significantly smaller than the noise emission from the rotor due to upstream obstacles and thus a noise reduction may be anticipated by moving struts downstream of the rotor (Filleul 1966).

- *Tip clearance eccentricity* was investigated by Fukano *et al.* (1986). Especially for small tip clearances a considerable discrete frequency noise was found at the blade passing frequency. This suggests that constructions with small tip clearance must be accompanied by a very accurate centering of the rotor axis. Furthermore, the duct must be highly circular and all blades of exactly the same length.
- *Blade irregularities* can cause discrete frequencies below the blade passing frequency if e.g. some blades have an error in the stagger angle setting (Fukano *et al.* 1980).

The *broad band* noise (or non-rotational) is random in nature and, although not exhaustive, the following sources have been identified as some of the most important:

- *Tip clearance* between blade and outer wall has a large impact on the broad band noise. For rotor axis centered with duct axis, a reduction in tip clearance results in a large decrease in noise emission. Furthermore, an improved efficiency of the fan may be anticipated (Fukano *et al.* 1986; Longhouse 1976).
- *Turbulence.* Large scale inflow turbulence results in lift fluctuations which can increase the broad band noise considerably and thus a smooth inflow is essential. Furthermore, pressure fluctuations in the turbulent boundary layer on the blade surface may develop noise. Investigations have shown that this noise source is insignificant compared to noise from inflow turbulence and vortex shedding (Sharland 1964).
- *Blade stall* will create large fluctuating forces on the suction side of the fan blades, which in turn generates noise (Sharland 1964).
- *Vortex shedding* noise is due to the vorticity shed from the trailing edge of the blades which produces local lift fluctuations. Some of the factors affecting the vortex shedding have been identified by Fukano *et al.* (1977a) and incorporated into an engineering prediction model. The model was afterwards validated against experiments by varying the following factors: chord length, number of blades and blade camber (Fukano *et al.* 1977b), angular velocity, blade thickness and outer blade profile (Fukano *et al.* 1978). Longhouse (1977) investigated the possibility of reducing the vortex shedding noise by introducing vortex generators on the suction side of the blades.

Considering both the periodic and broad band noise, the only significant noise generating mechanisms originating from the rotor itself, is the blade stall noise and the vortex shedding noise. All of the other noise sources mentioned above can be more or less removed by means of carefully manufacturing the blades and duct to remove tip effects, upstream struts and inflow turbulence.

For the minimization of the vortex shedding noise by means of numerical design optimization, a reliable, yet numerically efficient, analysis model is necessary. Here, the model developed by Fukano *et al.* (1977a) has been chosen. This model has been thoroughly validated against experiments and is adequate for comparing different designs in the optimization process. In appendix C, a brief description of the prediction model for the vortex shedding noise is presented.

In a recent work a similar, but more elaborate, model for the vortex shedding noise is presented (Lee *et al.* 1993). Here, comparisons show that the new prediction model is in slightly better agreement with experiments than the model by Fukano *et al.* (1977a). Lee *et al.* (1993) argues that this may be due to the boundary layer parameters in their work being based on airfoils in cascade, whereas flat plate parameters are used in Fukano *et al.* (1977a). Combined with an optimization scheme, the same noise prediction model is used to compare different designs. If the model used is able to, qualitatively, determine the differences in noise level to variations in the geometry of the fan, the quantitative determination of the noise emission is of less importance. Due to its simplicity and thorough validation, the model from Fukano *et al.* (1977a) is chosen here.

Besides a noise prediction model, an aerodynamic model is needed to calculate the aerodynamic constraints, posed as part of the optimization problem. Furthermore, the model provides axial and tangential velocities relative to the rotating blade which is required by the noise prediction model. Fan engineers often employ the free vortex flow model for the design of high-efficiency fans. However, this model imposes restrictions on the radial distributions of axial and tangential velocity across the rotor, thus limiting the degree of freedom of the design. To avoid this, an arbitrary vortex flow model is required and here, the model presented in chapter 1 is used.

The vortex shedding model due to Fukano *et al.* (1977a) has been used by Yang and Nie (1986) to investigate the potential of noise minimization of axial fans. As in Kahane (1948), the cascade method is employed for predicting the axial velocity distribution which corresponds to a prescribed tangential velocity distribution. Also, the pressure rise is predicted and, by using the velocities, the vortex shedding noise can be determined. Integrating an optimization algorithm, the optimum spanwise distribution of tangential velocity resulting in minimum vortex shedding noise, while satisfying the pressure rise across the rotor, can be determined. Comparing measurements of the noise emission for the optimum fan with a fan, designed for a tangential velocity proportional to the square root of the inverse radial position, showed that a reduction in noise emission could be obtained.

5.2 Defining the Optimization Problem

Objective Function

In this chapter, the investigations are carried out in a design point of flow rate and pressure rise. In most of the investigations, the objective function to minimize is defined as the vortex shedding noise from the rotor. To compare different formulations of the optimization problem, section 5.4 furthermore considers objective functions to maximize the efficiency and to minimize the angular velocity of the rotor.

Design Variables

The design variables are the same as in chapter 4. Again, the blades are constructed using F-series airfoils with 2.5% nose droop. Also, the camber angle is varied from six to four percent from the hub to the tip.

Constraints

The constraints from chapter 4 are used in the present investigation. However, as described in the next section, minimization of the vortex shedding noise results in a large tangential velocity and a further constraint on the tangential velocity is required. For the investigations in section 5.5, constraints are imposed on the efficiency to create a low-noise fan with a predefined (minimum acceptable) value of efficiency. The above results in the following two constraints:

Tangential velocity in outlet: The ratio of tangential to axial velocity at the outlet must be smaller than 1.1 for all streamtubes. This limit is imposed to avoid vortex breakdown downstream of the rotor, a flow-state which cannot be captured by the aerodynamic model. The criterion for vortex breakdown is based on Squire (1960), where stability analysis was applied to three cases of uniform axial velocity with different spanwise distributions of tangential velocity. The analysis indicated that vortex breakdown occurs when the ratio of tangential to axial velocity is between 1.0 and 1.2, thus justifying the choice of 1.1 as the limit. As discussed in section 5.3, a large tangential velocity is anticipated when optimizing for minimum vortex shedding noise, and this constraint is almost always active. The constraint is also used for the maximization of efficiency and minimization of rotor angular velocity in section 5.4. However, in these cases, the constraint is not active.

Lower limit on η: For the investigations in section 5.5, a lower limit on the efficiency is ensured by imposing a constraint on the efficiency.

5.3 Expected Behaviour for an Optimum Design

When minimizing the vortex shedding noise, expected observations of the vortex shedding noise model, described in appendix C, are:

- The governing equations in the aerodynamic model (section 1.2) are coupled. This means that any change in geometry or angular velocity of the rotor will influence the solution for all streamtubes. $V_{rel,i}$ and thus the SPL are therefore altered by any change in geometry.

- The sound power level in eq. (C.5) contains the relative velocity $V_{rel,i}$ to the sixth power. Thus, to minimize the sound power level, $V_{rel,i}$ must be small. Continuity imposes restrictions on the axial velocity, whereas the tangential velocity can vary freely within the aerodynamic constraints. According to eq. (1.15), the tangential velocity will thus be large in order to minimize $V_{rel,i}$.

- From eq. (C.5) it can be seen that the sound power level is proportional to the number of blades. From eq. (C.6) it is seen that, even with $D_T = 0$, D is proportional to the chord to the power of 0.8 at the most. Therefore, the noise emission is generally lower for a rotor with few blades of large chord than for a rotor with many blades of small chords.

- The use of an approximate expression for the trailing edge boundary layer thickness may cause problems when rotors with large differences in camber are compared. In the present work this is not an issue since the camber is not included in the optimization. Also, under stalled conditions, the boundary layer thickness is radically changed. A constraint is imposed to ensure non-stalled conditions at the design point.

5.4 Minimum Noise, Maximum η and Minimum Ω

In the following, optimizations are performed to 1: minimize noise, 2: maximize η and 3: minimize Ω. The design point is chosen as $Q = 2100m^3/h$ and $p_T = 300$ Pa for all three optimizations and thus the same aerodynamic operating characteristics exist for the calculations. Optimizations are performed for four to eight blades.

In Fig. 5.1, the vortex shedding noise for the three optimal designs are depicted as a function of the number of blades. As expected, the lowest noise emission is found for the first case where the vortex shedding noise is minimized. The minimization of the angular velocity yields a higher vortex shedding noise and the maximization of the efficiency the highest vortex shedding noise. Furthermore, in all three cases, the vortex shedding noise increases with the number of blades which agrees with the observations in section 5.1. A difference of as much as 10 dB is found when comparing the vortex shedding noise for the minimum noise and maximum efficiency optimizations.

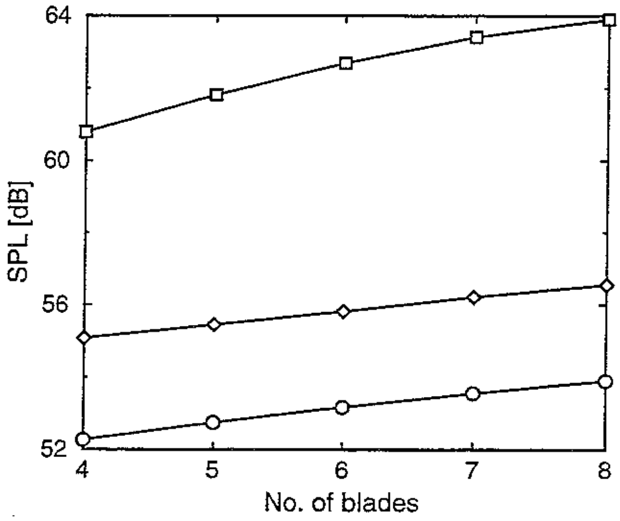

Figure 5.1: Vortex shedding noise for the optimum designs found in section 5.4. $Q = 2100m^3/h$, $p_T = 300$ Pa.
○: Optimization for minimum vortex shedding noise, □: Optimization for maximum efficiency, ◇: Optimization for minimum angular velocity.

In Fig. 5.2, the efficiencies for the three optimizations are shown. As expected, the highest efficiency is obtained in the second case where the efficiency is maximized. Optimization for minimum vortex shedding noise yields a considerably lower efficiency and the lowest efficiency is found when the angular velocity is minimized. A difference in efficiency of about 0.12 is found between the maximum efficiency and the minimum noise case. Corresponding to the findings in chapter 4, the efficiency typically increases with the number of blades.

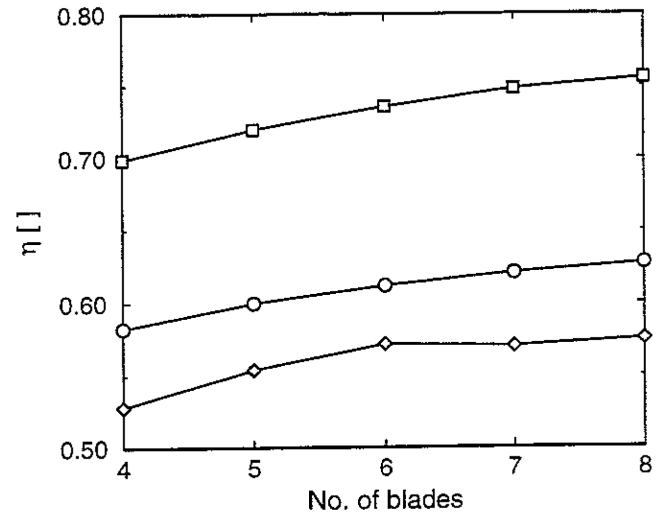

Figure 5.2: Efficiency for the optimum designs found in section 5.4. $Q = 2100m^3/h$, $p_T = 300$ Pa.
○: Optimization for minimum vortex shedding noise, □: Optimization for maximum efficiency, ◇: Optimization for minimum angular velocity.

Finally, Fig. 5.3 shows the angular velocity for the three optimizations. As expected, the lowest angular velocity is found in the third case where the angular velocity is minimized. A higher angular velocity is found for the minimum noise case and the highest angular velocity occurs for the maximum efficiency case. Especially, it may be noted that the angular velocity for the latter case increases to the constraining value of 3100 RPM for all number of blades. This corresponds to the findings in chapter 4 and is explained by the fact that a higher angular velocity results in a higher relative velocity on the blades and thus enables a higher energy transfer from the rotor to the fluid. This in turn implies a larger degree of freedom for the optimizer to increase efficiency. The high relative velocity results in a large vortex shedding noise, which can be seen in Fig. 5.1.

To summarize; optimization for minimum vortex shedding noise tends to increase the tangential velocity of the flow at the same time as the angular velocity of the rotor is lowered, both of which results in low relative velocity on the blades, followed by a low vortex shedding noise. When optimizing for maximum efficiency, opposite tendencies are experienced. The angular velocity of the rotor obtains the maximum allowed value and, furthermore, the tangential velocity is lowered since it does not contribute to the total pressure rise and thus not to the efficiency. The fact that optimization for minimum vortex shedding noise results in low-efficiency fans and that optimization for maximum efficiency yields high-noise fans, indicates that it is appropriate to perform optimizations where both vortex shedding noise and efficiency are considered. This is investigated in the following section.

It is a generally accepted belief that high-efficiency fans exhibit low overall noise characteristics. However, this is because several of the noise generating mechanisms, e.g. tip clearance, distorted inflow and blade stall, also result in increased aerodynamic losses. The findings in this chapter only apply to the noise generated due to vortex shedding from the blades. Thus, the obtained results do not contradict the above.

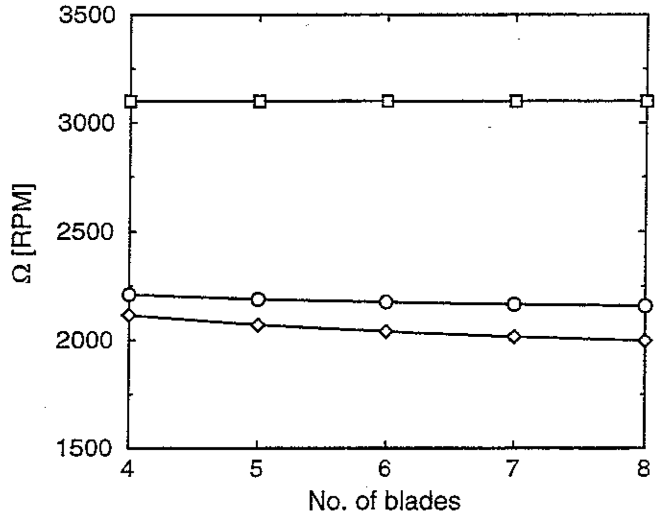

Figure 5.3: Angular velocity for the optimum designs found in section 5.4. $Q = 2100m^3/h$, $p_T = 300$ Pa.
○: Optimization for minimum vortex shedding noise, □: Optimization for maximum efficiency, ◇: Optimization for minimum angular velocity.

5.5 Minimum Noise, Constraining η

In section 5.4, it was shown that high efficiency results in a high vortex shedding noise and that low noise results in low efficiency. In this section, a situation is considered in which the vortex shedding noise is minimized while a minimum value constraint is imposed on the efficiency.

Fig. 5.4 shows the vortex shedding noise of optimizations performed for four blades, $Q = 2100m^3/h$ and $p_T = 300$ Pa or $p_T = 500$ Pa. In addition to the constraints used in the previous section, the efficiency is constrained to be above the values shown on the axis of the abscissa. A high pressure rise requirement is difficult to obtain and, as expected, the case of $p_T = 300$ Pa allows a larger variation in efficiency and vortex shedding noise than the $p_T = 500$ Pa case. Furthermore, the slope of the curves increases with increasing constraint value of the efficiency. This indicates that, for high-efficiency fans, a large reduction in vortex shedding noise can be obtained with only limited loss in efficiency. Furthermore, for the low-noise fans, a large increase in efficiency can be obtained with only a small increase in vortex shedding noise. The fan engineer can thus design a fan which either has a low noise emission or a high efficiency, depending on the requirements for the specific installation.

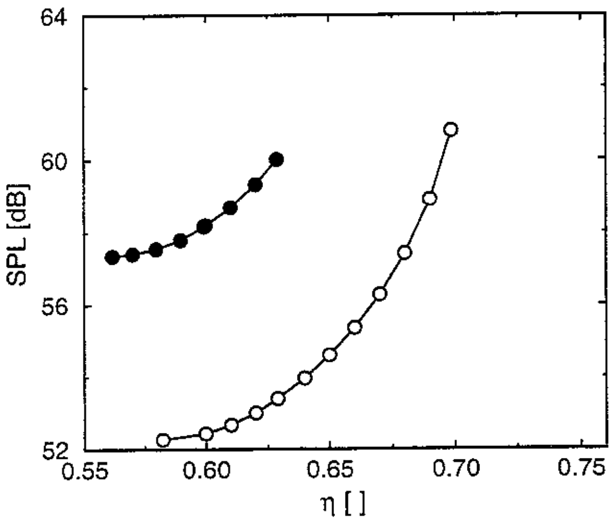

Figure 5.4: Minimum vortex shedding noise with constraint on efficiency, $Q = 2100m^3/h$, 4 blades.
○: $p_T = 300$ Pa, ●: $p_T = 500$ Pa.

Performing similar optimizations for rotors with six and eight blades, combining the curves, and only taking the part of the curves with the lowest vortex shedding noise for a given efficiency, results in Fig. 5.5. For the design point of $Q = 2100m^3/h$ and either $p_T = 300$ Pa or $p_T = 500$ Pa, the figure provides the fan engineer with a simple graphical representation which, for a given desired efficiency and vortex shedding noise, can be used to select the appropriate fan configuration. This, of course, requires access to the geometry and angular velocity resulting from each of the optimizations. Creating similar curves for various values of flow rate and pressure rise results in a very usable tool for fan selection purposes.

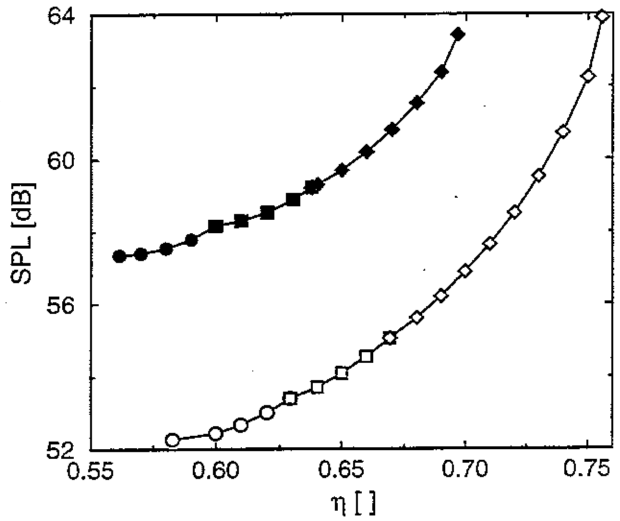

Figure 5.5: Minimum vortex shedding noise with constraint on efficiency, $Q = 2100 m^3/h$.
○: 4 blades, □: 6 blades, ◇: 8 blades. Open symbols: $p_T = 300$ Pa, filled symbols: $p_T = 500$ Pa.

5.6 Minimum Noise, Fixed Hub Radius

In the previous sections, the hub radius, r_0, was included as a design variable in the optimization. Here, excluding the hub radius as a design variable, the minimum vortex shedding noise is investigated as a function of the hub radius. A change of the hub radius results in a changed magnitude of the axial velocity component of the relative velocity. Thus, a smaller hub radius results in a smaller axial velocity and, since the vortex shedding noise generally increases with increasing relative velocity, it may be expected that a small value of r_0 is found for the optimum designs. Furthermore, the losses in the downstream diffusion process, partly included in the expression for secondary drag, increases with increasing hub radius. On the other hand, the pressure rise capability of the fan is reduced for smaller hub radii since the possible momentum exchange between the rotor and the flow is lowered for lowered relative velocities.

The above observations indicate that two opposing effects exist when designing a low-noise fan at a given pressure requirement. At low relative velocities, i.e. at small hub radius, it may be hard to fulfil the pressure rise required and thus only a limited degree of freedom in the design exists for minimizing the vortex shedding noise. Contrary to this, at high relative velocities, i.e. large hub radius, the pressure rise requirement may easily be met, but even though a large degree of freedom exists for the lowering of the vortex shedding noise, only a limited reduction is possible since the relative velocity is high.

It is thus expected that the design with the smallest possible vortex shedding noise is found at a hub radius not too small, nor too large. This is confirmed by optimizations performed for various values of hub radii. All at the design point of $Q = 2100m^3/h$ and either $p_T = 300$ Pa or $p_T = 500$ Pa. In Fig. 5.6, the minimum vortex shedding noise as a function of the hub radius is shown for the two pressure rise duties. It is seen that the curves exhibits a minimum, confirming the above discussions. The lower ending point of the curves is the lowest value of the hub radius for which a solution, satisfying the constraints, could be found. The upper ending point of the curves is the constraining value. As expected, the interval of hub radii in which a solution can be found is larger for the case of $p_T = 300$ Pa and, furthermore, the vortex shedding noise is lower than the case of $p_T = 500$ Pa. Both of which agrees with the fact that it is harder to fulfil the $p_T = 500$ Pa requirement and thus, the degree of freedom for the optimizer is limited.

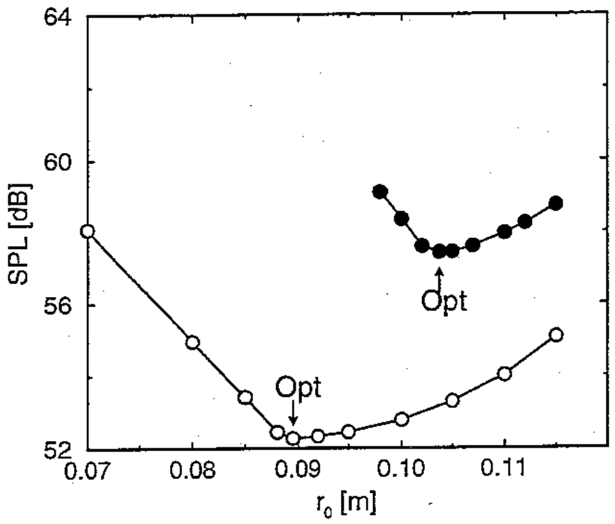

Figure 5.6: Minimum vortex shedding noise as a function of hub radius. Points designated *Opt* are values found when including the hub radius as a design variable in the optimization. $Q = 2100m^3/h$, 4 blades. ○: $p_T = 300$ Pa, ●: $p_T = 500$ Pa.

CHAPTER 6

Conclusion

6.1 The Aerodynamic Models

A numerically efficient mathematical model for the aerodynamics of axial fans of the arbitrary vortex flow type has been developed. Unlike the usually employed free vortex design method, no requirements for the spanwise distributions of velocity and pressure are necessary. Thus, the model can be used to analyse the aerodynamics of axial fans at the design and off-design flow rates, regardless of the flow type.

The model is based on a blade-element principle, whereby the rotor is divided into a number of annular streamtubes. For each of these streamtubes relations for velocity, pressure and radial position are derived from the incompressible conservation laws for mass, tangential momentum and energy. The resulting system of equations is non-linear and, due to mass conservation and pressure equilibrium far downstream of the rotor, strongly coupled.

The governing equations are formulated in a general way to enable calculations of rotor units, experiencing rotating inflow. Therefore, the model can be used for fan-stages constructed with one or more rotor units. The equations are solved using the Newton-Raphson method, and solutions converged to machine accuracy are found at small computing costs. To decrease the computational costs when analysing rotor-only fan stages, a "simplified" version of the model has been formulated, where the flow upstream of the rotor is uniform and non-rotating. Furthermore, for the rotor-only case, a correction to the governing equations is proposed for the solution of heavily loaded rotors.

The model has been validated against published measurements on various fan configurations, comprising two rotor-only fan stages, a counter-rotating fan unit and a stator-rotor-stator stage. For all the measurement setups, considerations have been given to provide a uniform inflow, avoid excessive tip clearance, etc. Thus, the measurements conform well with the assumptions for the aerodynamic model.

An essential requirement of the model is access to reliable lift and drag coefficients for the airfoils of the blades. For the validations, three sources of airfoil data have been used: 1: isolated airfoil data, empirically corrected for multiplane interference, 2: calculated airfoil data in cascade configurations and 3: airfoil data from measurements in a cascade wind-tunnel. Also, to account for wall boundary layers and other losses, an empirical secondary loss term is included in the drag contribution.

Comparisons with measured integrated properties, i.e. shaft power, pressure rise and efficiency, show that the computed results agree well with the measurements for various flow rates. As expected, the results are highly dependent on the quality of the airfoil data and, especially for low flow rates, the stall characteristics of the airfoils must be accurately described. When measurements of the airfoil data have been performed in a cascade wind-tunnel, as for the NACA 65-(12)10 airfoil, the validity of the model is found to be very good, even when stall is approached.

Comparisons of calculated and measured local properties, i.e. spanwise distributions of velocities and pressure, have been performed. Although the influence from boundary layers and secondary flows cannot be captured by the model, the agreement with the flowfield is generally satisfactory.

For one of the rotor-only cases considered, the correction for heavily loaded rotors becomes active at small flow rates. The correction mainly influences the flow at the inner part of the blades and, although the flow is altered locally, the integrated properties are in good agreement with the measurements.

6.2 The Optimization for Maximum Efficiency

Integrating a rotor-only version of the aerodynamic model with an algorithm for numerical design optimization provides a design-tool for axial fans. As opposed to the normally used free vortex design method, the arbitrary vortex flow model is valid for a range of flow rates. Optimizations can thus be performed to maximize the mean value of fan efficiency in a design interval of flow rates, designing a fan which operates well over a range of different flow conditions.

The angular velocity of the rotor, the hub radius and the spanwise distributions of pitch angle and chord length have been chosen as design variables in the optimizations. Constraints have been added to restrict the geometry, as well as the angular velocity of the rotor. Furthermore, constraints were imposed to ensure a required pressure rise of the rotor and non-stalled flow conditions on the blades. Finally, to ensure validity of the aerodynamic model, a constraint was imposed to keep the axial velocity at the hub above a certain minimum.

The optimization scheme is used to investigate the dependence of maximum efficiency on the number of blades and, due to the expression for secondary losses, it is found that more blades of small chord results in a higher efficiency than few blades of large chord.

The dependence of the maximum efficiency on the width of the design interval is examined and a considerable design interval width is possible with only limited reduction in maximum efficiency, compared to the maximum efficiency found for a single design point.

Finally, the dependence of the maximum efficiency on the hub radius is investigated and an optimum hub radius is found, for which a maximum efficiency exists. For smaller hub radii, the pressure rise requirement is hard to fulfill. For larger hub radii, the secondary losses become excessive. To obtain the largest degree of freedom for altering the blade geometries, the angular velocity of the rotor is maximized for all investigations. Furthermore, the constraints ensuring the required pressure rise and non-stalled flow conditions are always active.

To summarize, the combination of an optimization algorithm and an aerodynamic model for arbitrary vortex flow fans provides a general design-tool with a large degree of freedom. The possibility of specifying a design interval of flow rates is found to be especially valuable.

Prototypes of two of the optimum fan configurations have been constructed and tested in a measurement setup at the Danish Institute of Technology, and the agreement with the predictions from the aerodynamic model was found to be poor. The discrepancies are believed to be mostly caused by excessive tip clearances for the two fan rotors. However, further investigations are necessary before final conclusions can be drawn.

6.3 The Optimization for Minimum Noise

Although many sources of noise exist for axial fans, the blade stall noise and the vortex shedding noise from the trailing edge of the blades are the only significant noise sources originating from the rotor. To further investigate the use of design optimization, a model for the vortex shedding noise from the trailing edge of the blades has been incorporated into the optimization scheme and the noise emission from the blades was minimized in a flow rate design point. The same design variables and constraints from the efficiency-maximization have been used and, furthermore, a constraint has been imposed on the tangential velocity.

Comparing the vortex shedding noise, when performing a minimization of the noise, with the cases of maximization of the efficiency or minimization of the angular velocity of the rotor, shows that the potential of noise reduction is large. Also, the vortex shedding noise increases with increasing number of blades of the rotor.

Adding a constraint on the efficiency, it is found that, for a high-efficiency fan, a considerable noise reduction can be obtained with a limited reduction in fan efficiency. Furthermore, for a low-noise fan, a large increase in efficiency is possible with only limited increase in noise emission.

Finally, the dependence of the minimum vortex shedding noise on the hub radius is examined, and an optimum hub radius is found, for which a minimum vortex shedding noise exists. For smaller hub radii, the pressure rise requirement is hard to fulfill. For larger hub radii, the relative velocity on the blades becomes large, resulting in increased vortex shedding noise.

To summarize, the inclusion of a vortex shedding noise model in the optimization of axial fans provides a design-tool which, depending on the specific application of the fan, may be used to design a fan for a certain pressure rise, efficiency and noise level.

APPENDIX A

Differentiation of the Governing Equations

In this appendix, the discretized governing equations from section 1.3 are differentiated.

In section 1.2, the aerodynamic model for ducted axial flow fans with prerotations was formulated. In section 1.3, the governing equations were discretized and a description of the numerical solution method was given. The solution of the discretized equations are found using the Newton-Raphson method which exhibits quadratic convergence. As shown in eq. (1.27), the method requires the Jacobian matrix. Determination of the derivatives of the discretized governing equations with respect to the independent variables are trivial, but lengthy, and the explicit differentiation is presented in this appendix.

Alternatively, the Jacobian matrix may be calculated using finite difference approximations. The implementation is simpler since the only information needed is the discretized governing equations. However, the calculation-time for the finite difference approach are several orders of magnitude larger than the one employing explicit differentiation of the equations. In the present work, the initial implementation of the aerodynamic model was programmed using difference approximations. After preliminary investigations showed that the model compared well with measurements, the final version was implemented employing explicit differentiation of the Jacobian matrix. This two-step programming furthermore enabled validation of the differentiation of the governing equations.

As described in section 1.3, in each control volume, the independent variables in the model are:

- The radial position at the rotor disc, r_d.
- The radial position at the outlet, far downstream of the rotor disc, r_2.
- The axially induced velocity, w.
- The pressure far downstream of the rotor disc, p_2.
- The tangential velocity immediately downstream of the rotor disc, $V_{\theta_{d2}}$.

Furthermore, the three global variables of the model are:

- The pressure level, p_0.
- The induced velocity level, w_0.
- The average C_L value, C_{mid}.

To ease the following derivation of the differentiated governing equations, help-variables are defined and differentiated below.

First, the geometrical user-input of chord, pitch, camber and thickness of the blades as a function of radius is considered. The data are stored in one-dimensional arrays and values at given radii are determined using linear interpolation. In the aerodynamic model, the lift and drag forces are centered in the control volumes. For control volume i, this means that the geometrical properties depend on both $r_{d,i-1}$ and $r_{d,i}$.

Considering e.g. the chord for the i'th control volume, ch_i, and denoting the linear interpolation of the chord by LIN_{ch} yields

$$ch_i = LIN_{ch}\left(\frac{1}{2}\left(r_{d,i-1}+r_{d,i}\right)\right). \tag{A.1}$$

The derivative of the chord with respect to $r_{d,i}$ is found using a central difference approximation. Denoting the difference interval by 2Δ yields

$$\begin{aligned}\frac{\partial ch_i}{\partial r_{d,i}} &= \frac{LIN_{ch}\left(\frac{1}{2}\left(r_{d,i-1}+r_{d,i}+\Delta\right)\right) - LIN_{ch}\left(\frac{1}{2}\left(r_{d,i-1}+r_{d,i}-\Delta\right)\right)}{2\Delta},\\ \frac{\partial ch_i}{\partial r_{d,i-1}} &= \frac{\partial ch_i}{\partial r_{d,i}}.\end{aligned} \tag{A.2}$$

Similarly, values and derivatives of pitch, camber and thickness are denoted

$$\begin{aligned} pi_i,\ &\frac{\partial pi_i}{\partial r_{d,i-1}} \text{ and } \frac{\partial pi_i}{\partial r_{d,i}},\\ cam_i,\ &\frac{\partial cam_i}{\partial r_{d,i-1}} \text{ and } \frac{\partial cam_i}{\partial r_{d,i}},\\ th_i,\ &\frac{\partial th_i}{\partial r_{d,i-1}} \text{ and } \frac{\partial th_i}{\partial r_{d,i}}.\end{aligned} \tag{A.3}$$

The derivatives of the stagger angle, ξ_i, are found from the pitch angle since $\xi_i = 90 - pi_i$.

The solidity, σ, is defined by

$$\sigma_i = \frac{B \cdot ch_i}{\pi\left(r_{d,i-1}+r_{d,i}\right)}, \tag{A.4}$$

and the derivatives are

$$\begin{aligned}\frac{\partial \sigma_i}{\partial r_{d,i-1}} &= \frac{B}{\pi}\,\frac{\frac{\partial ch_i}{\partial r_{d,i-1}}\left(r_{d,i-1}+r_{d,i}\right) - ch_i}{\left(r_{d,i-1}+r_{d,i}\right)^2},\\ \frac{\partial \sigma_i}{\partial r_{d,i}} &= \frac{\partial \sigma_i}{\partial r_{d,i-1}}.\end{aligned} \tag{A.5}$$

The equation ensuring preserved circulation before the rotor is restated from section 1.2.1:

$$V_{\theta_1} \cdot \bar{r}_1 = V_{\theta_{d1}} \cdot \bar{r}_d. \tag{1.1}$$

Formulated in the independent variables and rearranging yields

$$V_{\theta_{d1},i} = V_{\theta_1,i}\frac{r_{1,i}+r_{1,i-1}}{r_{d,i}+r_{d,i-1}}. \tag{A.6}$$

Differentiating with respect to the independent variables, $r_{d,i}$ and $r_{d,i-1}$ yields

$$\begin{aligned}
\frac{\partial V_{\theta_{d1},i}}{\partial r_{d,i-1}} &= -\frac{V_{\theta_{d1},i}}{r_{d,i}+r_{d,i-1}},\\
\frac{\partial V_{\theta_{d1},i}}{\partial r_{d,i}} &= \frac{\partial V_{\theta_{d1},i}}{\partial r_{d,i-1}}.
\end{aligned} \tag{A.7}$$

The equation preserving circulation after the rotor is

$$V_{\theta_{d2}} \cdot \bar{r}_d = V_{\theta_2} \cdot \bar{r}_2. \tag{1.2}$$

Formulated in the independent variables and rearranging yields

$$V_{\theta_2,i} = V_{\theta_{d2},i} \frac{r_{d,i}+r_{d,i-1}}{r_{2,i}+r_{2,i-1}}. \tag{A.8}$$

Differentiating with respect to the independent variables, $r_{d,i}$, $r_{d,i-1}$, $r_{2,i}$, $r_{2,i-1}$ and $V_{\theta_{d2},i}$ yields

$$\begin{aligned}
\frac{\partial V_{\theta_{2,i}}}{\partial r_{d,i-1}} &= \frac{V_{\theta_{d2,i}}}{r_{2,i}+r_{2,i-1}},\\
\frac{\partial V_{\theta_{2,i}}}{\partial r_{d,i}} &= \frac{\partial V_{\theta_{2,i}}}{\partial r_{d,i-1}},\\
\frac{\partial V_{\theta_{2,i}}}{\partial r_{2,i-1}} &= -\frac{V_{\theta_{2,i}}}{r_{2,i}+r_{2,i-1}},\\
\frac{\partial V_{\theta_{2,i}}}{\partial r_{2,i}} &= \frac{\partial V_{\theta_{2,i}}}{\partial r_{2,i-1}},\\
\frac{\partial V_{\theta_{2,i}}}{\partial V_{\theta_{d2},i}} &= \frac{r_{d,i}+r_{d,i-1}}{r_{2,i}+r_{2,i-1}}.
\end{aligned} \tag{A.9}$$

The axial velocity at the rotor disc is

$$V_{x_d,i} = V_{x_1,i} + w_i, \tag{A.10}$$

which differentiates to

$$\frac{\partial V_{x_d,i}}{\partial w_i} = 1. \tag{A.11}$$

Far downstream of the rotor disc, the axial velocity is

$$V_{x_2,i} = V_{x_1,i} + 2w_i + w_0, \tag{A.12}$$

which differentiates to

$$\begin{aligned}
\frac{\partial V_{x_2,i}}{\partial w_i} &= 2,\\
\frac{\partial V_{x_2,i}}{\partial w_0} &= 1.
\end{aligned} \tag{A.13}$$

The tangential velocity relative to the blade at the rotor disc is

$$V_{\theta_d,i} = \frac{1}{2}\left(r_{d,i} + r_{d,i-1}\right)\Omega - \frac{1}{2}\left(V_{\theta_{d1},i} + V_{\theta_{d2},i}\right). \tag{A.14}$$

Differentiation of the above yields

$$\begin{aligned}
\frac{\partial V_{\theta_d,i}}{\partial r_{d,i-1}} &= \frac{1}{2}\Omega - \frac{1}{2}\frac{\partial V_{\theta_{d1},i}}{\partial r_{d,i-1}},\\
\frac{\partial V_{\theta_d,i}}{\partial r_{d,i}} &= \frac{1}{2}\Omega - \frac{1}{2}\frac{\partial V_{\theta_{d1},i}}{\partial r_{d,i}},\\
\frac{\partial V_{\theta_d,i}}{\partial V_{\theta_{d2},i}} &= -\frac{1}{2}.
\end{aligned} \tag{A.15}$$

Defining vv_i as the ratio of tangential-to-axial velocity yields

$$\begin{aligned}
vv_i &= \frac{V_{\theta_d,i}}{V_{x_d,i}},\\
\frac{\partial vv_i}{\partial r_{d,i-1}} &= \frac{\frac{\partial V_{\theta_d,i}}{\partial r_{d,i-1}}}{V_{x_d,i}},\\
\frac{\partial vv_i}{\partial r_{d,i}} &= \frac{\frac{\partial V_{\theta_d,i}}{\partial r_{d,i}}}{V_{x_d,i}},\\
\frac{\partial vv_i}{\partial V_{\theta_{d2},i}} &= \frac{\frac{\partial V_{\theta_d,i}}{\partial V_{\theta_{d2},i}}}{V_{x_d,i}},\\
\frac{\partial vv_i}{\partial w_i} &= \frac{-vv_i\frac{\partial\frac{\partial V_{x_d,i}}{\partial w_i}}{\partial w_i}}{V_{x_d,i}}.
\end{aligned} \tag{A.16}$$

Introducing the axial and tangential velocity definitions from eqs. (A.10) and (A.14) in the expression for the velocity relative to the rotor disc, eq. (1.15), and rewriting yields

$$V_{rel,i} = \sqrt{V_{\theta_d,i}^2 + V_{x_d,i}^2}. \tag{A.17}$$

Differentiating, yields

$$\begin{aligned}
\frac{\partial V_{rel,i}}{\partial r_{d,i-1}} &= \frac{1}{2V_{rel,i}}\left(2V_{\theta_d,i}\frac{\partial V_{\theta_d,i}}{\partial r_{d,i-1}}\right),\\
\frac{\partial V_{rel,i}}{\partial r_{d,i}} &= \frac{1}{2V_{rel,i}}\left(2V_{\theta_d,i}\frac{\partial V_{\theta_d,i}}{\partial r_{d,i}}\right),\\
\frac{\partial V_{rel,i}}{\partial V_{\theta_{d2},i}} &= \frac{1}{2V_{rel,i}}\left(2V_{\theta_d,i}\frac{\partial V_{\theta_d,i}}{\partial V_{\theta_{d2},i}}\right),\\
\frac{\partial V_{rel,i}}{\partial w_i} &= \frac{1}{2V_{rel,i}}\left(2V_{x_d,i}\frac{\partial V_{x_d,i}}{\partial w_i}\right).
\end{aligned} \tag{A.18}$$

Similarly, the equation for the angle between the axis of rotation and the relative velocity, eq. (1.16), is rewritten and differentiated as

$$\begin{aligned}
\beta_i &= \arctan\left(\frac{V_{\theta_d,i}}{V_{x_d,i}}\right), \\
\frac{\partial \beta_i}{\partial r_{d,i-1}} &= \frac{1}{1+vv_i^2}\frac{\partial vv_i}{\partial r_{d,i-1}}, \\
\frac{\partial \beta_i}{\partial r_{d,i}} &= \frac{1}{1+vv_i^2}\frac{\partial vv_i}{\partial r_{d,i}}, \\
\frac{\partial \beta_i}{\partial V_{\theta_{d2},i}} &= \frac{1}{1+vv_i^2}\frac{\partial vv_i}{\partial V_{\theta_{d2},i}}, \\
\frac{\partial \beta_i}{\partial w_i} &= \frac{1}{1+vv_i^2}\frac{\partial vv_i}{\partial w_i}.
\end{aligned} \tag{A.19}$$

Defining trigonometric equations as

$$\begin{aligned}
\sin\beta_i &= \frac{V_{\theta_d,i}}{V_{rel,i}}, \\
\cos\beta_i &= \frac{V_{x_d,i}}{V_{rel,i}},
\end{aligned} \tag{A.20}$$

differentiating yields

$$\begin{aligned}
\frac{\partial \sin\beta_i}{\partial r_{d,i-1}} &= \cos\beta_i \frac{\partial \beta_i}{\partial r_{d,i-1}}, \\
\frac{\partial \sin\beta_i}{\partial r_{d,i}} &= \cos\beta_i \frac{\partial \beta_i}{\partial r_{d,i}}, \\
\frac{\partial \sin\beta_i}{\partial V_{\theta_{d2},i}} &= \cos\beta_i \frac{\partial \beta_i}{\partial V_{\theta_{d2},i}}, \\
\frac{\partial \sin\beta_i}{\partial w_i} &= \cos\beta_i \frac{\partial \beta_i}{\partial w_i},
\end{aligned} \tag{A.21}$$

and

$$\begin{aligned}
\frac{\partial \cos\beta_i}{\partial r_{d,i-1}} &= -\sin\beta_i \frac{\partial \beta_i}{\partial r_{d,i-1}}, \\
\frac{\partial \cos\beta_i}{\partial r_{d,i}} &= -\sin\beta_i \frac{\partial \beta_i}{\partial r_{d,i}}, \\
\frac{\partial \cos\beta_i}{\partial V_{\theta_{d2},i}} &= -\sin\beta_i \frac{\partial \beta_i}{\partial V_{\theta_{d2},i}}, \\
\frac{\partial \cos\beta_i}{\partial w_i} &= -\sin\beta_i \frac{\partial \beta_i}{\partial w_i}.
\end{aligned} \tag{A.22}$$

The angle of attack experienced by the rotating blade is defined and differentiated as

$$\begin{aligned}
\alpha_i &= \beta_i - \xi_i, \\
\frac{\partial \alpha_i}{\partial r_{d,i-1}} &= \frac{\partial \beta_i}{\partial r_{d,i-1}} - \frac{\partial \xi_i}{\partial r_{d,i-1}}, \\
\frac{\partial \alpha_i}{\partial r_{d,i}} &= \frac{\partial \beta_i}{\partial r_{d,i}} - \frac{\partial \xi_i}{\partial r_{d,i}}, \\
\frac{\partial \alpha_i}{\partial V_{\theta_{d2},i}} &= \frac{\partial \beta_i}{\partial V_{\theta_{d2},i}}, \\
\frac{\partial \alpha_i}{\partial w_i} &= \frac{\partial \beta_i}{\partial w_i}.
\end{aligned} \tag{A.23}$$

Lift and drag coefficient for the blade elements are found by table-lookup. Since effects from multiplane interference is included in the airfoil data, lift and drag coefficients are functions of angle of attack, stagger, solidity, camber and thickness. The gradients of the coefficients are found using central difference approximations. The same procedure as described for the chord in eq. (A.2) is used. This results in the following items:

$$\begin{aligned}
&C_{L,i}, \ \frac{\partial C_{L,i}}{\partial \alpha_i}, \frac{\partial C_{L,i}}{\partial \xi_i}, \frac{\partial C_{L,i}}{\partial \sigma_i}, \frac{\partial C_{L,i}}{\partial cam_i}, \frac{\partial C_{L,i}}{\partial th_i}, \\
&C_{D,i}, \ \frac{\partial C_{D,i}}{\partial \alpha_i}, \frac{\partial C_{D,i}}{\partial \xi_i}, \frac{\partial C_{D,i}}{\partial \sigma_i}, \frac{\partial C_{D,i}}{\partial cam_i}, \frac{\partial C_{D,i}}{\partial th_i}.
\end{aligned} \tag{A.24}$$

And the coefficient differentiated with respect to the independent variables are

$$\begin{aligned}
\frac{\partial C_{L,i}}{\partial r_{d,i-1}} &= \frac{\partial C_{L,i}}{\partial \alpha_i}\frac{\partial \alpha_i}{\partial r_{d,i-1}} + \frac{\partial C_{L,i}}{\partial \xi_i}\frac{\partial \xi_i}{\partial r_{d,i-1}} + \frac{\partial C_{L,i}}{\partial \sigma_i}\frac{\partial \sigma_i}{\partial r_{d,i-1}} \\
&\quad + \frac{\partial C_{L,i}}{\partial cam_i}\frac{\partial cam_i}{\partial r_{d,i-1}} + \frac{\partial C_{L,i}}{\partial th_i}\frac{\partial th_i}{\partial r_{d,i-1}}, \\
\frac{\partial C_{L,i}}{\partial r_{d,i}} &= \frac{\partial C_{L,i}}{\partial \alpha_i}\frac{\partial \alpha_i}{\partial r_{d,i}} + \frac{\partial C_{L,i}}{\partial \xi_i}\frac{\partial \xi_i}{\partial r_{d,i}} + \frac{\partial C_{L,i}}{\partial \sigma_i}\frac{\partial \sigma_i}{\partial r_{d,i}} \\
&\quad + \frac{\partial C_{L,i}}{\partial cam_i}\frac{\partial cam_i}{\partial r_{d,i}} + \frac{\partial C_{L,i}}{\partial th_i}\frac{\partial th_i}{\partial r_{d,i}}, \\
\frac{\partial C_{L,i}}{\partial V_{\theta_{d2},i}} &= \frac{\partial C_{L,i}}{\partial \alpha_i}\frac{\partial \alpha_i}{\partial V_{\theta_{d2},i}}, \\
\frac{\partial C_{L,i}}{\partial w_i} &= \frac{\partial C_{L,i}}{\partial \alpha_i}\frac{\partial \alpha_i}{\partial w_i}.
\end{aligned} \tag{A.25}$$

Similar expressions exist for the drag coefficient.

The secondary drag contribution, eq. (1.40), is rewritten as

$$C_{D_s,i} = a\bar{C}_L^2 + b\frac{ch_i}{\sigma_i\left(r_N - r_0\right)}, \tag{A.26}$$

and differentiated as

$$\begin{aligned}
\frac{\partial C_{D_s,i}}{\partial r_{d,i-1}} &= \frac{b}{r_N - r_0} \cdot \frac{\frac{\partial ch_i}{\partial r_{d,i-1}}\sigma - ch_i \frac{\partial \sigma_i}{\partial r_{d,i-1}}}{\sigma_i^2}, \\
\frac{\partial C_{D_s,i}}{\partial r_{d,i}} &= \frac{b}{r_N - r_0} \cdot \frac{\frac{\partial ch_i}{\partial r_{d,i}}\sigma - ch_i \frac{\partial \sigma_i}{\partial r_{d,i}}}{\sigma_i^2}, \\
\frac{\partial C_{D_s,i}}{\partial \bar{C}_L} &= 2a\bar{C}_L.
\end{aligned} \tag{A.27}$$

Defining dummy variables $x1_i$, $x2_i$ and $x3_i$ as

$$\begin{aligned}
x1_i &= \frac{\rho B}{2\pi} \frac{ch_i}{r_{d,i} + r_{d,i-1}} V_{rel}^2, \\
x2_i &= C_{l,i} \sin(\beta) - (C_{D,i} + C_{D_s,i}) \cos(\beta), \\
x3_i &= C_{l,i} \cos(\beta) + (C_{D,i} + C_{D_s,i}) \sin(\beta),
\end{aligned} \tag{A.28}$$

and differentiating with respect to the independent variables yield

$$\begin{aligned}
\frac{\partial x1_i}{\partial r_{d,i-1}} &= \frac{\rho B}{2\pi} \left(\frac{\frac{\partial ch_i}{\partial r_{d,i-1}}(r_{d,i} + r_{d,i-1}) - ch_i}{(r_{d,i} + r_{d,i-1}]^2} V_{rel,i}^2 + \frac{ch_i}{r_{d,i} + r_{d,i-1}} 2V_{rel,i} \frac{\partial V_{rel,i}}{\partial r_{d,i-1}} \right), \\
\frac{\partial x1_i}{\partial r_{d,i}} &= \frac{\rho B}{2\pi} \left(\frac{\frac{\partial ch_i}{\partial r_{d,i}}(r_{d,i} + r_{d,i-1}) - ch_i}{(r_{d,i} + r_{d,i-1}]^2} V_{rel,i}^2 + \frac{ch_i}{r_{d,i} + r_{d,i-1}} 2V_{rel,i} \frac{\partial V_{rel,i}}{\partial r_{d,i}} \right), \\
\frac{\partial x1_i}{\partial V_{\theta_{d2},i}} &= \frac{\rho B}{2\pi} \frac{ch_i}{r_{d,i} + r_{d,i-1}} 2V_{rel,i} \frac{\partial V_{rel,i}}{\partial V_{\theta_{d2},i}}, \\
\frac{\partial x1_i}{\partial w_i} &= \frac{\rho B}{2\pi} \frac{ch_i}{r_{d,i} + r_{d,i-1}} 2V_{rel,i} \frac{\partial V_{rel,i}}{\partial w_i},
\end{aligned} \tag{A.29}$$

$$\begin{aligned}
\frac{\partial x2_i}{\partial r_{d,i-1}} &= \frac{\partial C_{L,i}}{\partial r_{d,i-1}}\sin(\beta_i) + C_{L,i}\frac{\partial \sin(\beta_i)}{\partial r_{d,i-1}} \\
&\quad - \left(\frac{\partial C_{D,i}}{\partial r_{d,i-1}} + \frac{\partial C_{D_s,i}}{\partial r_{d,i-1}}\right)\cos(\beta) - (C_{D,i} + C_{D_s,i})\frac{\partial \cos(\beta_i)}{\partial r_{d,i-1}}, \\
\frac{\partial x2_i}{\partial r_{d,i}} &= \frac{\partial C_{L,i}}{\partial r_{d,i}}\sin(\beta_i) + C_{L,i}\frac{\partial \sin(\beta_i)}{\partial r_{d,i}} \\
&\quad - \left(\frac{\partial C_{D,i}}{\partial r_{d,i}} + \frac{\partial C_{D_s,i}}{\partial r_{d,i}}\right)\cos(\beta_i) - (C_{D,i} + C_{D_s,i})\frac{\partial \cos(\beta_i)}{\partial r_{d,i}}, \\
\frac{\partial x2_i}{\partial V_{\theta_{d2},i}} &= \frac{\partial C_{L,i}}{\partial V_{\theta_{d2},i}}\sin(\beta_i) + C_{L,i}\frac{\partial \sin(\beta_i)}{\partial V_{\theta_{d2},i}} \\
&\quad - \frac{\partial C_{D,i}}{\partial V_{\theta_{d2},i}}\cos(\beta_i) - (C_{D,i} + C_{D_s,i})\frac{\partial \cos(\beta_i)}{\partial V_{\theta_{d2},i}}, \\
\frac{\partial x2_i}{\partial w_i} &= \frac{\partial C_{L,i}}{\partial w_i}\sin(\beta_i) + C_{L,i}\frac{\partial \sin(\beta_i)}{\partial w_i} \\
&\quad - \frac{\partial C_{D,i}}{\partial w_i}\cos(\beta_i) - (C_{D,i} + C_{D_s,i})\frac{\partial \cos(\beta_i)}{\partial w_i}, \\
\frac{\partial x2_i}{\partial \bar{C}_L} &= -\frac{\partial C_{D_s,i}}{\partial \bar{C}_L}\cos(\beta_i),
\end{aligned} \tag{A.30}$$

$$\begin{aligned}
\frac{\partial x3_i}{\partial r_{d,i-1}} &= \frac{\partial C_{L,i}}{\partial r_{d,i-1}}\cos(\beta_i) + C_{L,i}\frac{\partial \cos(\beta_i)}{\partial r_{d,i-1}} \\
&\quad + \left(\frac{\partial C_{D,i}}{\partial r_{d,i-1}} + \frac{\partial C_{D_s,i}}{\partial r_{d,i-1}}\right)\sin(\beta) + (C_{D,i} + C_{D_s,i})\frac{\partial \sin(\beta_i)}{\partial r_{d,i-1}}, \\
\frac{\partial x3_i}{\partial r_{d,i}} &= \frac{\partial C_{L,i}}{\partial r_{d,i}}\cos(\beta_i) + C_{L,i}\frac{\partial \cos(\beta_i)}{\partial r_{d,i}} \\
&\quad + \left(\frac{\partial C_{D,i}}{\partial r_{d,i}} + \frac{\partial C_{D_s,i}}{\partial r_{d,i}}\right)\sin(\beta_i) + (C_{D,i} + C_{D_s,i})\frac{\partial \sin(\beta_i)}{\partial r_{d,i}}, \\
\frac{\partial x3_i}{\partial V_{\theta_{d2},i}} &= \frac{\partial C_{L,i}}{\partial V_{\theta_{d2},i}}\cos(\beta_i) + C_{L,i}\frac{\partial \cos(\beta_i)}{\partial V_{\theta_{d2},i}} \\
&\quad + \frac{\partial C_{D,i}}{\partial V_{\theta_{d2},i}}\sin(\beta_i) + (C_{D,i} + C_{D_s,i})\frac{\partial \sin(\beta_i)}{\partial V_{\theta_{d2},i}}, \\
\frac{\partial x3_i}{\partial w_i} &= \frac{\partial C_{L,i}}{\partial w_i}\cos(\beta_i) + C_{L,i}\frac{\partial \cos(\beta_i)}{\partial w_i} \\
&\quad + \frac{\partial C_{D,i}}{\partial w_i}\sin(\beta_i) + (C_{D,i} + C_{D_s,i})\frac{\partial \sin(\beta_i)}{\partial w_i}, \\
\frac{\partial x3_i}{\partial \bar{C}_L} &= \frac{\partial C_{D_s,i}}{\partial \bar{C}_L}\sin(\beta_i).
\end{aligned} \tag{A.31}$$

Inserting the definitions of lift and drag force, eq. (1.17), in the expression for axial and tangential volume force, eq. (1.18), and using the above dummy-variables, eqs. (A.30-

A.32), these may be rewritten and differentiated as

$$
\begin{aligned}
f_{x,i} &= x1_i \cdot x2_i, \\
\frac{\partial f_{x,i}}{\partial r_{d,i-1}} &= x1_i \frac{\partial x2_i}{\partial r_{d,i-1}} + x2_i \frac{\partial x1_i}{\partial r_{d,i-1}}, \\
\frac{\partial f_{x,i}}{\partial r_{d,i}} &= x1_i \frac{\partial x2_i}{\partial r_{d,i}} + x2_i \frac{\partial x1_i}{\partial r_{d,i}}, \\
\frac{\partial f_{x,i}}{\partial V_{\theta_{d2},i}} &= x1_i \frac{\partial x2_i}{\partial V_{\theta_{d2},i}} + x2_i \frac{\partial x1_i}{\partial V_{\theta_{d2},i}}, \\
\frac{\partial f_{x,i}}{\partial w_i} &= x1_i \frac{\partial x2_i}{\partial w_i} + x2_i \frac{\partial x1_i}{\partial w_i}, \\
\frac{\partial f_{x,i}}{\partial \bar{C}_L} &= x1_i \frac{\partial x2_i}{\partial \bar{C}_L},
\end{aligned}
\tag{A.32}
$$

$$
\begin{aligned}
f_{\theta,i} &= x1_i \cdot x3_i, \\
\frac{\partial f_{\theta,i}}{\partial r_{d,i-1}} &= x1_i \frac{\partial x2_i}{\partial r_{d,i-1}} + x2_i \frac{\partial x1_i}{\partial r_{d,i-1}}, \\
\frac{\partial f_{\theta,i}}{\partial r_{d,i}} &= x1_i \frac{\partial x2_i}{\partial r_{d,i}} + x2_i \frac{\partial x1_i}{\partial r_{d,i}}, \\
\frac{\partial f_{\theta,i}}{\partial V_{\theta_{d2},i}} &= x1_i \frac{\partial x2_i}{\partial V_{\theta_{d2},i}} + x2_i \frac{\partial x1_i}{\partial V_{\theta_{d2},i}}, \\
\frac{\partial f_{\theta,i}}{\partial w_i} &= x1_i \frac{\partial x2_i}{\partial w_i} + x2_i \frac{\partial x1_i}{\partial w_i}, \\
\frac{\partial f_{\theta,i}}{\partial \bar{C}_L} &= x1_i \frac{\partial x3_i}{\partial \bar{C}_L}.
\end{aligned}
\tag{A.33}
$$

After all of these initial definitions, the discretized governing equations, eqs. (1.19-1.26), can be differentiated.

Continuity equation, inlet - rotor disc (D_i):

$$
\begin{aligned}
D_i \equiv & \left(r_{1,i}^2 - r_{1,i-1}^2\right)\left(V_{x_1,i}\right) \\
& - \left(r_{d,i}^2 - r_{d,i-1}^2\right)\left(V_{x_1,i} + w_i\right) = 0,
\end{aligned}
\tag{1.19}
$$

differentiating to

$$
\begin{aligned}
\frac{\partial D_i}{\partial r_{d,i-1}} &= 2 r_{d,i-1}\left(V_{x_1,i} + w_i\right), \\
\frac{\partial D_i}{\partial r_{d,i}} &= -2 r_{d,i}\left(V_{x_1,i} + w_i\right), \\
\frac{\partial D_i}{\partial w_i} &= -\left(r_{d,i}^2 - r_{d,i-1}^2\right).
\end{aligned}
\tag{A.34}
$$

However, when $i = N$, D_i is used to fix the tip radius by using the equations

$$\begin{aligned} D_i &\equiv r_{d,i} - r_N = 0, \\ \frac{\partial D_i}{\partial r_{d,i-1}} &= 0, \\ \frac{\partial D_i}{\partial r_{d,i}} &= 1, \\ \frac{\partial D_i}{\partial w_i} &= 0. \end{aligned} \tag{A.35}$$

Continuity equation, rotor disc - outlet (E_i):

$$\begin{aligned} E_i \equiv & \left(r_{d,i}^2 - r_{d,i-1}^2\right) V_{x_d,i} \\ & - \left(r_{2,i}^2 - r_{2,i-1}^2\right) V_{x_2,i} = 0, \end{aligned} \tag{1.20}$$

differentiating to

$$\begin{aligned} \frac{\partial E_i}{\partial r_{d,i-1}} &= -2 r_{d,i-1} V_{x_d,i}, \\ \frac{\partial E_i}{\partial r_{d,i}} &= 2 r_{d,i} V_{x_d,i}, \\ \frac{\partial E_i}{\partial r_{2,i-1}} &= 2 r_{2,i-1} V_{x_2,i}, \\ \frac{\partial E_i}{\partial r_{2,i}} &= -2 r_{2,i} V_{x_2,i}, \\ \frac{\partial E_i}{\partial w_i} &= \left(r_{d,i}^2 - r_{d,i-1}^2\right) \frac{\partial V_{x_d,i}}{\partial w_i} - \left(r_{2,i}^2 - r_{2,i-1}^2\right) \frac{\partial V_{x_2,i}}{\partial w_i}, \\ \frac{\partial E_i}{\partial w_0} &= -\left(r_{2,i}^2 - r_{2,i-1}^2\right) \frac{\partial V_{x_d,i}}{\partial w_0}. \end{aligned} \tag{A.36}$$

Similarly as for the inlet-rotor disc continuity, a special equation is introduced for $i = N$.

Axial relation (F_i):

$$\begin{aligned} F_i \equiv & \frac{1}{2}\left(p_{2,i} + p_{2,i-1} - p_{1,i} - p_{1,i-1}\right) + p_0 \\ & + \frac{1}{2}\rho\left[V_{x_2,i}^2 - V_{x_1,i}^2\right] \\ & + \frac{1}{2}\rho\left[V_{\theta_{d2},i}^2\left(\left(\frac{r_{d,i} + r_{d,i-1}}{r_{2,i} + r_{2,i-1}}\right)^2 - 1\right)\right] \\ & + \frac{1}{2}\rho\left[V_{\theta_1,i}^2\left(\left(\frac{r_{1,i} + r_{1,i-1}}{r_{d,i} + r_{d,i-1}}\right)^2 - 1\right)\right] - f_x = 0, \end{aligned} \tag{1.21}$$

which rewrites and differentiates to

$$
\begin{aligned}
F_i \equiv {} & \frac{1}{2}\left(p_{2,i} - p_{2,i-1}\right) + p_0 - \frac{1}{2}\left(p_{1,i} - p_{1,i-1}\right) \\
& + \frac{1}{2}\rho\left(V_{x2,i}^2 - V_{x1,i}^2\right) \\
& + \frac{1}{2}\rho\left(V_{\theta_2,i}^2 - V_{\theta_{d2},i}^2\right) \\
& + \frac{1}{2}\rho\left(V_{\theta_{d1},i}^2 - V_{\theta_1,i}^2\right) - f_{x,i}, \\
\frac{\partial F_i}{\partial r_{d,i-1}} &= \rho V_{\theta_2,i}\frac{\partial V_{\theta_2,i}}{\partial r_{d,i-1}} + \rho V_{\theta_{d1},i}\frac{\partial V_{\theta_{d1},i}}{\partial r_{d,i-1}} - \frac{\partial f_{x,i}}{\partial r_{d,i-1}}, \\
\frac{\partial F_i}{\partial r_{d,i}} &= \rho V_{\theta_2,i}\frac{\partial V_{\theta_2,i}}{\partial r_{d,i}} + \rho V_{\theta_{d1},i}\frac{\partial V_{\theta_{d1},i}}{\partial r_{d,i}} - \frac{\partial f_{x,i}}{\partial r_{d,i}}, \\
\frac{\partial F_i}{\partial r_{2,i-1}} &= \rho V_{\theta_2,i}\frac{\partial V_{\theta_2,i}}{\partial r_{2,i-1}}, \\
\frac{\partial F_i}{\partial r_{2,i}} &= \rho V_{\theta_2,i}\frac{\partial V_{\theta_2,i}}{\partial r_{2,i}}, \\
\frac{\partial F_i}{\partial w_i} &= \rho V_{x2,i}\frac{\partial V_{x2,i}}{\partial w_i} - \frac{\partial f_{x,i}}{\partial w_i}, \\
\frac{\partial F_i}{\partial p_{2,i-1}} &= \frac{1}{2}, \\
\frac{\partial F_i}{\partial p_{2,i}} &= \frac{1}{2}, \\
\frac{\partial F_i}{\partial V_{\theta_{d2},i}} &= \frac{1}{2}\rho\left(2V_{\theta_2,i}\frac{\partial V_{\theta_2,i}}{\partial V_{\theta_{d2},i}} - 2V_{\theta_{d2},i}\right) - \frac{\partial f_{x,i}}{\partial V_{\theta_{d2},i}}, \\
\frac{\partial F_i}{\partial p_0} &= 1, \\
\frac{\partial F_i}{\partial w_0} &= \rho V_{x2,i}\frac{\partial V_{x2,i}}{\partial w_0}, \\
\frac{\partial F_i}{\partial \bar{C}_L} &= -\frac{\partial f_{x,i}}{\partial \bar{C}_L}.
\end{aligned}
\tag{A.37}
$$

Pressure equilibrium (G_i):

$$
\begin{aligned}
G_i \equiv {} & \frac{1}{2}\left(r_{2,i} + r_{2,i-1}\right)^3\left(p_{2,i} - p_{2,i-1}\right) \\
& - \rho V_{\theta_{d2},i}^2\left(r_{d,i} + r_{d,i-1}\right)^2\left(r_{2,i} - r_{2,i-1}\right) = 0.
\end{aligned}
\tag{1.22}
$$

Rewritten and differentiated yields

$$\begin{aligned}
G_i &\equiv \frac{1}{2}\left(r_{2,i}+r_{2,i-1}\right)\left(p_{2,i}-p_{2,i-1}\right)-\rho V_{\theta_2,i}^2\left(r_{2,i}-r_{2,i-1}\right),\\
\frac{\partial G_i}{\partial r_{d,i-1}} &= -2\rho\left(r_{2,i}-r_{2,i-1}\right)V_{\theta_2,i}\frac{\partial V_{\theta_2,i}}{\partial r_{d,i-1}},\\
\frac{\partial G_i}{\partial r_{d,i}} &= -2\rho\left(r_{2,i}-r_{2,i-1}\right)V_{\theta_2,i}\frac{\partial V_{\theta_2,i}}{\partial r_{d,i}},\\
\frac{\partial G_i}{\partial r_{2,i-1}} &= \frac{1}{2}\left(p_{2,i}-p_{2,i-1}\right)+\rho V_{\theta_2,i}^2-2\rho\left(r_{2,i}-r_{2,i-1}\right)V_{\theta_2,i}\frac{\partial V_{\theta_2,i}}{\partial r_{2,i-1}},\\
\frac{\partial G_i}{\partial r_{2,i}} &= \frac{1}{2}\left(p_{2,i}-p_{2,i-1}\right)-\rho V_{\theta_2,i}^2-2\rho\left(r_{2,i}-r_{2,i-1}\right)V_{\theta_2,i}\frac{\partial V_{\theta_2,i}}{\partial r_{2,i}},\\
\frac{\partial G_i}{\partial p_{2,i-1}} &= -\frac{1}{2}\left(r_{2,i}+r_{2,i-1}\right),\\
\frac{\partial G_i}{\partial p_{2,i}} &= \frac{1}{2}\left(r_{2,i}+r_{2,i-1}\right),\\
\frac{\partial G_i}{\partial V_{\theta_{d2},i}} &= -2\rho\left(r_{2,i}-r_{2,i-1}\right)V_{\theta_2,i}\frac{\partial V_{\theta_2,i}}{\partial V_{\theta_{d2},i}}.
\end{aligned} \tag{A.38}$$

Tangential momentum equation (H_i):

$$H_i \equiv \rho\left(V_{x_1,i}+w_i\right)\left(V_{\theta_{d2},i}-V_{\theta_1,i}\frac{r_{1,i}+r_{1,i-1}}{r_{d,i}+r_{d,i-1}}\right)-f_{\theta,i}=0. \tag{1.23}$$

Rewrites and differentiates to

$$\begin{aligned}
H_i &\equiv \rho V_{x_d,i}\left(V_{\theta_{d2},i}-V_{\theta_{d1},i}\right)-f_{\theta,i}=0,\\
\frac{\partial H_i}{\partial r_{d,i-1}} &= -\rho V_{x_d,i}\frac{\partial V_{\theta_{d1},i}}{\partial r_{d,i-1}}-\frac{\partial f_{\theta,i}}{\partial r_{d,i-1}},\\
\frac{\partial H_i}{\partial r_{d,i}} &= -\rho V_{x_d,i}\frac{\partial V_{\theta_{d1},i}}{\partial r_{d,i}}-\frac{\partial f_{\theta,i}}{\partial r_{d,i}},\\
\frac{\partial H_i}{\partial w_i} &= \rho\left(V_{\theta_{d2},i}-V_{\theta_{d1},i}\right)-\frac{\partial f_{\theta,i}}{\partial w_i},\\
\frac{\partial H_i}{\partial V_{\theta_{d2},i}} &= \rho V_{x_d,i}-\frac{\partial f_{\theta,i}}{\partial V_{\theta_{d2},i}}.
\end{aligned} \tag{A.39}$$

Global continuity at the rotor disc (I_1).

$$I_1 \equiv \pi\sum_{i=1,N}\left(r_{d,i}^2-r_{d,i-1}^2\right)\left(V_{x_1,i}+w_i\right)-Q=0. \tag{1.24}$$

Rewritten and differentiated:

$$\begin{aligned}
I_1 &\equiv \pi\sum_{i=1,N}\left(r_{d,i}^2-r_{d,i-1}^2\right)V_{x_d,i}-Q=0,\\
\frac{\partial I_1}{\partial r_{d,i}} &= 2\pi r_{d,i}\left(V_{x_d,i}-V_{x_d,i+1}\big|_{i\neq N}\right),\\
\frac{\partial I_1}{\partial w_i} &= \pi\left(r_{d,i}^2-r_{d,i-1}^2\right)\frac{\partial V_{x_d,i}}{\partial w_i}.
\end{aligned} \tag{A.40}$$

Global continuity far downstream (I_2).

$$I_2 \equiv \pi \sum_{i=1,N} \left(r_{2,i}^2 - r_{2,i-1}^2\right) \left(V_{x_1,i} + 2w_i + w_0\right) - Q = 0. \tag{1.25}$$

Rewritten and differentiation yields

$$\begin{aligned}
I_2 &\equiv \pi \sum_{i=1,N} \left(r_{2,i}^2 - r_{2,i-1}^2\right) V_{x_2,i} - Q = 0, \\
\frac{\partial I_2}{\partial r_{2,i}} &= 2\pi r_{2,i} \left(V_{x_2,i} - V_{x_2,i+1}\,|_{i \neq N}\right), \\
\frac{\partial I_2}{\partial w_i} &= \pi \left(r_{2,i}^2 - r_{2,i-1}^2\right) \frac{\partial V_{x_2,i}}{\partial w_i}, \\
\frac{\partial I_2}{\partial w_0} &= \pi \left(r_N^2 - r_0^2\right).
\end{aligned} \tag{A.41}$$

Equation for $\bar{C}_L$ (I_3).

$$I_3 \equiv \pi \sum_{i=1,N} \left(r_{d,i}^2 - r_{d,i-1}^2\right) C_{L,i} - \pi \left(r_N^2 - r_0^2\right) \bar{C}_L = 0, \tag{1.26}$$

$$\begin{aligned}
\frac{\partial I_3}{\partial r_{d,i}} &= 2\pi r_{d,i} \left(C_{L,i} - C_{L,i+1}\right) + \pi \left(r_{d,i}^2 - r_{d,i-1}^2\right) \frac{\partial C_{L,i}}{\partial r_{d,i}} \\
&\quad - \pi \left(r_{d+1,i}^2 - r_{d,i}^2\right) \frac{\partial C_{L,i+1}}{\partial r_{d,i}}\,|_{i \neq N}, \\
\frac{\partial I_3}{\partial w_i} &= \pi \left(r_{d,i}^2 - r_{d,i-1}^2\right) \frac{\partial C_{L,i}}{\partial w_i}, \\
\frac{\partial I_3}{\partial V_{\theta_{d2},i}} &= \pi \left(r_{d,i}^2 - r_{d,i-1}^2\right) \frac{\partial C_{L,i}}{\partial V_{\theta_{d2},i}}, \\
\frac{\partial I_3}{\partial \bar{C}_L} &= -\pi \left(r_N^2 - r_0^2\right).
\end{aligned} \tag{A.42}$$

APPENDIX B

Fan-Geometries used for the Validations

This appendix contains a full description of the fan geometries used in the validations from chapter 2. Furthermore, rotor angular velocities and densities are listed, enabling calculations of the various fans used in this study.

Work by Downie *et al.* (1993)

For the comparisons of section 2.3.1, the rotor setup from Downie *et al.* has hub and tip radii of 0.116 m and 0.305 m, respectively. The angular velocity of the rotor is 1000 RPM and the dimensionless parameters from Downie *et al.* has been transformed with a density of $\rho = 1.21 kg/m^3$.

Case 1 rotor, denoted *Mark 3* in Downie *et al.* (1993) is designed using 6 blades comprising F-series airfoils with 2.5% nose-droop. The geometry at eight spanwise stations, provided by Thompson (1996), is given in Table B.1.

Table B.1: Spanwise geometry of the Case 1 rotor, investigated in section 2.3.1.

Radial position (m)	*Pitch* (degrees)	*Chord* (m)	*Camber* (%)	*Thickness* (% chord)
0.1220	31.1	0.125	7.25	10.0
0.1525	27.9	0.125	6.23	10.0
0.1830	25.0	0.125	4.86	10.0
0.2100	22.7	0.125	4.66	10.0
0.2135	22.5	0.125	4.64	10.0
0.2440	19.9	0.125	4.51	10.0
0.2745	17.8	0.125	4.37	10.0
0.2989	16.5	0.125	4.20	10.0

Case 2 rotor, denoted *Mark 1* in Downie *et al.* (1993) is designed using 8 blades constructed with cambered flat plate airfoils. Table B.2 provides geometries for the eight spanwise stations (Thompson 1996).

Work by Kahane (1948)

For the comparisons of section 2.3.2, the rotor has 24 blades, of the NACA 65-(12)10 airfoil. Hub and tip radii are 0.1840 m and 0.2667 m, respectively. The blades are constructed with a constant pitch angle of 41.8°. The chord is 0.05893 m, constant along the blade. The angular velocity of the rotor is 3000 RPM and the transformations of the dimensionless parameters were performed by a density of $\rho = 1.21 kg/m^3$.

Table B.2: Spanwise geometry of the Case 2 rotor, investigated in section 2.3.1.

Radial position (m)	*Pitch* (degrees)	*Chord* (m)	*Camber* (%)	*Thickness* (mm)
0.1220	32.3	0.128	6.25	2.0
0.1525	28.2	0.120	5.63	2.0
0.1830	25.2	0.112	5.15	2.0
0.2100	23.3	0.106	4.86	2.0
0.2135	23.0	0.106	4.77	2.0
0.2440	21.3	0.098	4.48	2.0
0.2745	20.0	0.090	4.20	2.0
0.2989	19.3	0.084	4.07	2.0

Work by Bell and DeKoster (1942)

For the investigations of the counter-rotating rotors (section 2.4), these comprise 12 or 24 blades of the 12 % thick RAF 6E airfoil. Hub and tip radii are 0.1840 m and 0.2667 m, respectively. The blades are constructed with a 6.5^o linear pitch from hub to tip and the chord is constant at 0.0508 m. The rotors are run at angular velocities between 3000 RPM and 3600 RPM. For the transformations of the dimensionless parameters, a rotor angular velocity of 3600 RPM and a density of $\rho = 1.21 kg/m^3$ are chosen.

The first of the rotors investigated in section 2.4 comprise 24 blades in both the front and the rear rotor. The hub pitch angle is 50.5^o for the front rotor and 30.5^o for the rear rotor. The second rotor has 24 blades in the front rotor and 12 blades in the rear rotor. Both at a hub pitch angle of 30.5^o.

Work by Mathews *et al.* (1967)

For the stator-rotor-stator investigations (section 2.5), geometries are provided in Wallis (1967). The hub and tip radii are 1.524 m and 3.048 m, respectively. During measurements, different values of the density appear. These are listed in the figures of section 2.5. The angular velocity of the rotor is 295 RPM.

The front stator (prerotator) comprises 9 blades of the 12 % thick C4 airfoil. Table B.3 provides a spanwise geometrical description at six stations along the blades. Here, the pitch angle is measured from the axial direction.

The rotor is constructed using 14 blades of the 10 % thick Clark Y airfoil. In Table B.4, a detailed geometrical description at seven spanwise stations is provided. The pitch-angles in the table corresponds to a blade setting angle of 0^o.

The rear stator comprises 11 blades of the 12 % thick C4 airfoil. Table B.5 provides a spanwise geometrical description at six stations along the blades.

Table B.3: Spanwise geometry of the front stator in the stator-rotor-stator configuration, investigated in section 2.5.

Radial position (m)	*Pitch* (degrees)	*Chord* (m)	*Camber* (%)	*Thickness* (% chord)
1.524	14.5	1.219	6.36	12.0
1.829	13.0	1.219	5.70	12.0
2.134	12.0	1.219	5.26	12.0
2.438	11.2	1.219	4.90	12.0
2.743	10.6	1.219	4.64	12.0
3.048	10.3	1.219	4.51	12.0

Table B.4: Spanwise geometry of the rotor in the stator-rotor-stator configuration, investigated in section 2.5.

Radial position (m)	*Pitch* (degrees)	*Chord* (m)	*Camber* (%)	*Thickness* (% chord)
1.524	30.4	0.848	-	10.0
1.829	27.5	0.620	-	10.0
2.134	25.3	0.506	-	10.0
2.286	24.0	0.471	-	10.0
2.438	22.9	0.437	-	10.0
2.743	21.3	0.399	-	10.0
3.048	19.4	0.368	-	10.0

Table B.5: Spanwise geometry of the rear stator in the stator-rotor-stator configuration, investigated in section 2.5.

Radial position (m)	*Pitch* (degrees)	*Chord* (m)	*Camber* (%)	*Thickness* (% chord)
1.524	76.5	1.308	10.35	12.0
1.829	78.8	1.308	9.18	12.0
2.134	80.6	1.308	8.28	12.0
2.438	82.0	1.308	7.52	12.0
2.743	83.2	1.308	6.94	12.0
3.048	84.0	1.308	6.47	12.0

APPENDIX C

Vortex Shedding Noise Model

This appendix presents the noise prediction model by Fukano *et al.* (1977a) used for prediction of the vortex shedding noise from the fan rotor.

The sound pressure level is determined using an empirical method by Fukano *et al.* (1977a), treating the broad band noise generated by the trailing edge vortex shedding. Essentially, the noise is generated due to fluctuations in the pressure around the blade which, in turn, can be attributed to the lift coefficient. Below, a summary of the analysis and assumptions from Fukano *et al.* (1977a) is presented.

When the approaching velocity is low compared to the velocity of sound, the sound power, e, due to lift fluctuations, may be estimated by the following equation:

$$e = \frac{\rho}{48\pi a_0^3}\int_{SPAN} cV_{rel}^4 S_c \langle \overline{\left[\frac{\partial C_L}{\partial t}\right]^2} \rangle dr, \qquad \text{(C.1)}$$

where a_0 is the velocity of sound. Furthermore, c is the length of the chord, V_{rel} the fluid velocity relative to the blade, S_c the correlation area of the pressure fluctuations and C_L the lift coefficient. All of which are functions of the radial coordinate, r.

Introducing proper scaling factors, the circulation, γ_0, from a fully developed vortex behind a 2-dimensional airfoil may be described by $\gamma_0 = V_{rel}D_w/2$, where D_w is a characteristic length, taken to be the width of the wake. Furthermore, knowing that the vortex shedding is periodic, the instantaneous lift force per unit blade length, F_L, induced by the circulation, can be described by

$$F_L(t) = \rho V_{rel}\gamma_0, sin\,(2\pi f t)\,, \qquad \text{(C.2)}$$

where f is the vortex shedding frequency.

Dividing the above by $1/2\rho c V_{rel}^2$, the lift coefficient is obtained. Introducing the expression for γ_0 yields

$$C_L(t) = D_w/c \cdot sin\,(2\pi f t) \qquad \text{(C.3)}$$

and the time averaged value of the square of $\partial C_L/\partial t$ becomes

$$\overline{\left[\frac{\partial C_L}{\partial t}\right]^2} = D_w^2\,(2\pi f)^2\,/(2c^2). \qquad \text{(C.4)}$$

Assuming the Strouhal number of the vortex shedding to be 0.2 yields $f = 0.2V_{rel}/D_w$ which can be inserted in eq. (C.4). The correlation area, S_c in eq. (C.1) is approximated by $S_c = cD_w/2$.

Dividing the fan blade into a number of blade elements, the sound power generated by a fan blade can be found as a numerical integration of eq. (C.1). Furthermore, assuming that the total sound power level from the rotor is the sum of the contributions from each blade, yields an equation for the total sound power level from the rotor,

$$E = \frac{B\pi\rho}{1200a_0^3} \sum_{i=1}^{N} D_{w,i} V_{rel,i}^6 \Delta r_i. \tag{C.5}$$

Finally, D_w is approximated as the sum of the trailing edge width of the airfoil ($D_{T,i}$) and the boundary layer thickness on each side of the airfoil. Assuming that the boundary layer can be approximated with a turbulent, zero pressure gradient boundary layer yields

$$D_{w,i} = D_{T,i} + 2(0.37/8 \cdot c_i) Re_i^{-0.2}, \tag{C.6}$$

where Re_i is the Reynolds number based on c_i and $V_{rel,i}$.

The sound pressure, $\sqrt{\overline{p^2}}$, can be calculated from the sound power by

$$E/2 = \left(\frac{4\pi}{3}\right)\left(\frac{d^2}{\rho a_0}\right)\overline{p^2} \tag{C.7}$$

where d is the distance from the rotor to the measuring probe. Finally, the sound pressure level (SPL) is defined as

$$SPL = 10 log_{10}\left(\frac{\overline{p^2}}{p_*^2}\right), \tag{C.8}$$

where p_* equals $2 \cdot 10^{-5} N/m^2$. In the calculations of the sound pressure level in chapter 5, an arbitrary value of $d = 1.5m$ is chosen and the trailing edge width is taken to be constant, $D_T = 1mm$.

Bibliography

Arora, J. S. (1989). *Introduction to optimum design.* McGraw-Hill.

Bell, E. B. (1942). Test of a single-stage axial-flow fan. Report 729, NACA, Langley Memorial Aeronautical Laboratory, Langley Field, Va.

Bell, E. B. and L. J. DeKoster (1942). Test of a dual-rotation axial-flow fan. Wartime Report L-303, NACA, Langley Memorial Aeronautical Laboratory, Langley Field, Va.

Bolton, A. N. (1990). Installation effects in fan systems. *Proceedings of the Institution of Mechanical Engineers, Part A 204*, 201–215.

BSI (1980). Fans for general purposes, part 1: Methods of testing fan performance. Standard BS 848 : Part 1, British Standards Institution.

Cudina, M. (1992). Noise generated by a vane-axial fan with inlet guide vanes. *Noise Control Engineering Journal 39*(1), 21–30.

Doak, P. E. and P. G. Vaidya (1969). A note on the relative importance of discrete frequency and broad-band noise generating mechanisms in axial fans. *Journal of Sound and Vibration 9*(2), 192–196.

Downie, R. J., M. C. Thompson and R. A. Wallis (1993). An engineering approach to blade designs for low to medium pressure rise rotor-only axial fans. *Experimental Thermal and Fluid Science 6*, 376–401.

Dugao, Z., Z. Jiang and J. Song (1996). Optimization design of an axial flow-fan used for mining local-ventilation. *Computers and Industrial Engineering 31*(3), 691–696.

Filleul, N. L. S. (1966). An investigation of axial flow fan noise. *Journal of Sound and Vibration 3*(2), 147–165.

Fletcher, R. (1971). A general quadratic programming algorithm. *Institute of Mathematics and its Applications, IMA. Journal 7*, 76–91.

Fukano, T., Y. Kodama and Y. Senoo (1977a). Noise generated by low pressure axial flow fans, I: Modeling of the turbulent noise. *Journal of Sound and Vibration 50*(1), 63–74.

Fukano, T., Y. Kodama and Y. Takamatsu (1977b). Noise generated by low pressure axial flow fans, II: Effects of number of blades, chord length and camber of blade. *Journal of Sound and Vibration 50*(1), 75–88.

Fukano, T., Y. Kodama and Y. Takamatsu (1978). Noise generated by low pressure axial flow fans, III: Effects of rotational frequency, blade thickness and outer blade profile. *Journal of Sound and Vibration 56*(2), 261–277.

Fukano, T., Y. Kodama and Y. Takamatsu (1980). Discrete frequency noise due to irregularity in blade row of axial fan rotor. *Bulletin of the JSME 23*(182), 1335–1343.

Fukano, T., Y. Takamatsu and Y. Kodama (1986). The effects of tip clearance on the noise of low pressure axial and mixed flow fans. *Journal of Sound and Vibration 105*(2), 291–308.

Gill, P. E., W. Murray and M. H. Wright (1981). *Practical Optimization.* Academic Press.

Glauert, H. (1935). Airplane propellers. In W. F. Durand (Ed.), *Aerodynamic Theory,* Volume 4, pp. 169–360. Berlin: Julius Springer.

Han, S. P. (1976). Superlinearly convergent variable metric algorithms for general nonlinear programming problems. *Mathematical Programming 11*, 263–282.

Herrig, L. J., J. C. Emery and J. R. Erwin (1951). Systematic two-dimensional cascade tests of NACA 65-series compressor blades at low speeds. Report RM L51G31, NACA, Langley Aeronautical Laboratory, Langley Field, Va.

Horlock, J. H. (1978). *Actuator Disk Theory. Discontinuities in Thermo-Fluid Dynamics.* McGraw-Hill Inc.

International Standard ISO 5801 (1997). Industrial fans - performance testing using standardized airways. Technical Report ISO 5801:1997 (E), The International Organization for Standardization.

Kahane, A. (1948). Investigation of axial-flow fan and compressor rotors designed for three-dimensional flow. Report Tech. Note 1652, NACA, Langley Memorial Aeronautical Laboratory, Langley Field, Va.

Lee, C., M. K. Chung and Y.-H. Kim (1993). A prediction model for the vortex shedding noise from the wake of an airfoil or axial flow fan blades. *Journal of Sound and Vibration 164*(2), 327–336.

Longhouse, R. E. (1976). Noise mechanism separation and design considerations for low tip-speed, axial-flow fans. *Journal of Sound and Vibration 48*(4), 461–474.

Longhouse, R. E. (1977). Vortex shedding noise of low tip speed, axial flow fans. *Journal of Sound and Vibration 53*(1), 25–46.

Madsen, K. (1991). Constrained optimization (in danish : Optimering under bibetingelser). Report 40, Numerical Institute, Technical University of Denmark.

Mathews, K. E. and P. G. North (1967). Development of the primary ventilation system at Mount Isa: I: Mining considerations. In *Proceedings / Australasian Institute of Mining and Metallurgy.*, Volume 222, pp. 1–19.

Mathews, K. E., P. G. North, R. A. Wallis, R. B. Menzies, R. H. Challen and N. Ruglen (1967). Development of the primary ventilation system at Mount Isa: I-IV. In *Proceedings / Australasian Institute of Mining and Metallurgy.*, Volume 222, pp. 1–61.

Menzies, R. B. and R. H. Challen (1967). Development of the primary ventilation system at Mount Isa: III: Engineering design and erection. In *Proceedings / Australasian Institute of Mining and Metallurgy.*, Volume 222, pp. 35–52.

Michelsen, J. A. (1992). Basis3D - a platform for development of multiblock PDE solvers. Technical note AFM92-05, Department of Fluid Mechanics, DTU, Denmark.

Mikkelsen, R. (1997). Private communication. Calculated airfoil data in cascade configurations.

Powell, M. J. D. (1978a). Algorithms for nonlinear constraints that use Lagrangian functions. *Mathematical Programming 14*, 224–248.

Powell, M. J. D. (1978b). A fast algorithm for nonlinearly constrained optimization calculations. In G. A. Watson (Ed.), *Lecture Notes in Mathematics*, Volume 630, pp. 144–157.

Press, W. H., S. A. Teukolsky, W. T. Vetterling and B. P. Flannery (1992). *Numerical recipes in FORTRAN: the art of scientific computing. page 128* (2 ed.). Cambridge University Press.

Randall, J. M., D. Berckmans and R. P. White (1996). A methodology to compare the performance of low pressure fan test rigs using non-dimensional fan characteristics. *Journal of Agricultural Engineering Research 65*, 235–246.

Roberts, W. B. (1975). The experimental cascade performance of NACA compressor profiles at low Reynolds number. *Journal of Engineering for Power, Transactions of the ASME 97*, 454–459.

Sharland, I. J. (1964). Sources of noise in axial flow fans. *Journal of Sound and Vibration 1*(3), 302–322.

Sørensen, D. N. and J. N. Sørensen (1996). Numerical optimization of a pitch controlled wind turbine. In A. Zervos, H. Ehmann and P. Helm (Eds.), *1996 European Union Wind Energy Conference. Proceedings of an International Conference held at Göteborg, Sweden, 20-24 May 1996*, pp. 863–866. H. S. Stephens & Associates.

Sørensen, D. N. and J. N. Sørensen (1997). Towards improved rotor-only axial fans. part I: A numerically efficient aerodynamic model for arbitrary vortex flow. *Submitted to the Journal of Fluids Engineering (1997)*, .

Sørensen, D. N., M. C. Thompson and J. N. Sørensen (1997). Towards improved rotor-only axial fans. part II: Design optimization for maximum efficiency. *Submitted to the Journal of Fluids Engineering (1997)*, .

Sørensen, N. N. (1995). General purpose flow solver applied to flow over hills. Ph.D. dissertation Risø-R-827(EN), Risø National Laboratory, Denmark.

Squire, H. B. (1960). Analysis of the vortex breakdown phenomenon. Part I. Report 102, Imperial College of Science and Technology, Aeronautics Department.

Thompson, M. C. (1996). Private communication. Blade geometries for Mark1 and Mark3 rotors.

Turner, R. C. (1966). Notes on ducted fan design. Current Papers C.P. 895, Ministry of Aviation, Aeronautical Research Council.

Venter, S. J. and D. G. Kröger (1992). The effect of tip clearance on the performance of an axial flow fan. *Energy Conversion and Management 33*(2), 89–97.

Von Backström, T. W., J. D. Buys and W. H. Stinnes (1996). Minimization of the exit loss of a rotor-only axial fan. *Engineering Optimization 26*, 25–33.

Wallis, R. A. (1961). *Axial Flow Fans. Design and Practice.* London: George Newnes Limited.

Wallis, R. A. (1967). Development of the primary ventilation system at Mount Isa: II: Aerodynamic design of new fans. In *Proceedings / Australasian Institute of Mining and Metallurgy.*, Volume 222, pp. 21–34.

Wallis, R. A. (1968). Optimisation of axial flow fan design. *Mechanical and Chemical Engineering Transactions. The Institution of Engineers, Australia. MC4*(1), 31–37.

Wallis, R. A. (1977). The F-series aerofoils for fan blade sections. *Mechanical Engineering Transactions. The Institution of Engineers, Australia. ME2*, 12–20.

Wallis, R. A. (1993). *Axial Flow Fans and Ducts.* Malabar, Florida: Krieger Publishing Company.

Wallis, R. A. and N. Ruglen (1967). Development of the primary ventilation system at Mount Isa: IV: Aerodynamic performance trials. In *Proceedings / Australasian Institute of Mining and Metallurgy.*, Volume 222, pp. 53–61.

Wright, T. (1984). Axial fan performance with blade-base clearance. *Journal of Engineering for Gas Turbines and Power, Transactions of the ASME 106*, 901–905.

Wright, T. (1996). Low pressure axial fans. In J. A. Schetz and A. E. Fuhs (Eds.), *Handbook of Fluid Dynamics and Fluid Machinery. - 3: Applications of Fluid Dynamics*, pp. 2340–2356. Chichester : Wiley.

Yang, X. and N. Nie (1986). The optimum low noise flow-type of low pressure axial flow fans. In R. Lotz (Ed.), *1986 International Conference on Noise Control Engineering. Inter-noise 86*, pp. 175–180. Noise Control Foundation.

Author Index

Index